Nonlinear dynamics of spatio-temporally driven lattices

Dissertation

zur Erlangung des Doktorgrades

des Fachbereichs Physik

der Universität Hamburg

vorgelegt von

Christoph Petri

aus Mannheim

Hamburg

2012

Gutachter der Dissertation:	Prof. Dr. Peter Schmelcher Prof. Dr. Fotis Diakonos
Gutachter der Disputation:	Prof. Dr. Peter Schmelcher Prof. Dr. Henning Moritz
Datum der Disputation:	04.05.2012
Vorsitzender des Prüfungsausschusses:	Prof. Dr. Günter Huber
Vorsitzender des Promotionsausschusses:	Prof. Dr. Peter Hauschildt
Leiterin des Fachbereichs Physik:	Prof. Dr. Daniela Pfannkuche
Dekan der MIN-Fakultät:	Prof. Dr. Heinrich Graener

Zusammenfassung

Im Rahmen dieser Arbeit wird die klassische und die Quantendynamik von Teilchen in raumzeitlich getriebenen Gittern untersucht. Im klassischen Regime zeigen wir, dass ein räumlich unterschiedliches zeitabhängiges Treiben neue Phänomene hervorruft und im Vergleich zu uniform getriebenen Gittern zu einer erhöhten Kontrolle über die Nichtgleichgewichtsdynamik der Teilchen führt. Durch geeingete Wahl der lokalen zeitabhängingen Treibgesetze können bestimmte Teile des klassischen Phasenraums auf eine kontrollierte Art und Weise manipuliert werden, während gleichzeitig der restliche Teil des Phasenraums davon im Wesentlichen unbeeinflusst bleibt. Mit Hilfe einer räumlich variierenden Phaseverschiebung des lokalen Treibens ist es möglich einen gerichteten Transport beziehungsweise lokalisierte chaotische Dynamik hervorzurufen, das heißt Teilchen können an eine bestimmte Position im Gitter transporiert und danach dort gefangen werden. Des Weiteren wird die Teilchendynamik in Gittern studiert, welche aus Blöcken mit unterschiedlichen zeitabhängige Treibgesetzen zusammengesetzt sind. Im Rahmen dieser Untersuchung finden wird, dass die Teilchen Übergänge in ihrem dynamischen Zustand zwischen chaotischer und regulärer Bewegung erfahren können, wenn sie sich von einem Block in einen anderen bewegen. Für ein Ensemble führen diese Übergangsprozesse zu lang anhaltenden, transienten periodischen Oszillationen der Teilchendichte. Indem man zeitabhänging die lokalen Treibgesetze verändert, können diese Modulationen in eine sich bewegende Dichtewelle von Teilchen umgewandelt werden. Im quantenmechanischen Regime wird die Schrödingergleichung des getriebenen Gitter mit Hilfe von Floquet- und Blochtheorie gelöst. Es wird gezeigt, dass ein monochromatisches Treiben mit räumlich variierender Phasenverschiebung ausreichend ist, um Quantentransport hervorzurufen.

Abstract

In this thesis we study the classical and the quantum dynamics of particles in spatiotemporally driven lattices. In the classical regime we find that a locally varying time-dependent driving leads to novel phenomena yielding an increased control over the non-equilibrium dynamics of the propagating particles compared to the case of a uniformly driven lattice. By means of an appropriate tuning of the local time-dependent forces certain parts of the classical phase space can be manipulated in a controllable manner whereas the remaining portion is mainly unaffected. By imposing a spatially varying phase shift to the driving we can evoke a directed current and create localized chaotic dynamics, i.e. particles can be transported to a certain position in the lattice and subsequently get trapped there. Moreover, we study lattices consisting of domains with different time-dependent forces. We find that particles can experience conversions in their dynamical state from chaotic to regular motion and vice versa when crossing from one domain to another. For an ensemble these conversion processes lead to long-time transient periodic oscillations of the particle density. By manipulating temporally the local driving forces these modulations can be rendered into a propagating density wave of particles. In the quantum regime the time-dependent Schrödinger-equation of the driven lattice is solved by means of Floquet- and Bloch theory. It is shown that a monochromatic driving combined with a spatially modulated phase shift is sufficient to evoke quantum transport.

Contents

Chapter 1

Introduction

Time-dependent forces are often the origin for the appearance of complex phenomena in physical systems. For instance, the quantum tunneling of a particle in a spatially symmetric double-well potential can be either enhanced drastically or almost completely suppressed by applying a time-periodic force [1–3]. In classical physics an interesting effect which can be evoked by a time-dependent driving, is "Fermi acceleration", i.e. the unbounded gain of kinetic energy of particles [4–6]. In fact, due to their rich phenomenology time-driven systems represent a major focus in several versatile research fields, such as the physics of atoms, molecules or mesoscopic systems [7–9].

Among the most prominent mesoscopic setups are the driven lattices, i.e. particles in a one-dimensional static potential are acted upon additionally by external time-dependent forces of zero mean. A spectacular phenomenon appearing in these systems is the so called "ratchet effect" or "directed transport", that is under certain circumstances one can observe a current of particles, although there exists no net force. During the last decades the question concerning the prerequisites for the ratchet effect to occur has been unraveled step-by-step. Since the second law of thermodynamics forbids the extraction of a net motion from equilibrium fluctuations, the system has to be constantly driven out of thermal equilibrium [10]. Due to the fact that ratchet effect is supposed to be the working principle of molecular motors [11–13] much effort has been made in the early 90's to understand how it can be generated by employing external noise [14–18]. For this class of systems the term "Brownian ratchet" or "Brownian motor" has been established and it has been shown that the outcome of such a ratchet can be a current of particles against a dc-bias [19–22]. An example showing this phenomenon is the flashing ratchet where an asymmetric sawtooth potential is periodically turned on and off. Its operational principle is schematically depicted in Fig. 1.1. In the beginning, when the potential is turned on, the Brownian particles are confined to a minimum of the sawtooth. Once the potential is turned off, the particles are accelerated in the direction of the bias and at the same time diffusion sets in which leads to a uniform spreading. When the potential is turned on again the asymmetry of the sawtooth causes more particles to be trapped in the right well than in the left well. Consequently, the particles will be transported against the dc-bias, if the switching of the potential is repeated periodically. It is important to note that this flashing ratchet works only in the presence of friction because the energy the particles gain when the potential is turned on has to be damped out so that the gathering of the particles in the minima of the sawtooth is possible. A very interesting connection of the just described Brownian ratchets can be drawn to game theory. Parrondo et al. showed that two losing gambling games can be combined to a winning one when the player switches "periodically" between the games. Mathematically, this is equivalent to a Brownian ratchet with discrete time [23, 24]. Experimentally, the ratchet effect has been observed in a variety of systems such as semiconductor heterostructures [25–27], Josephson junction array [28–30],

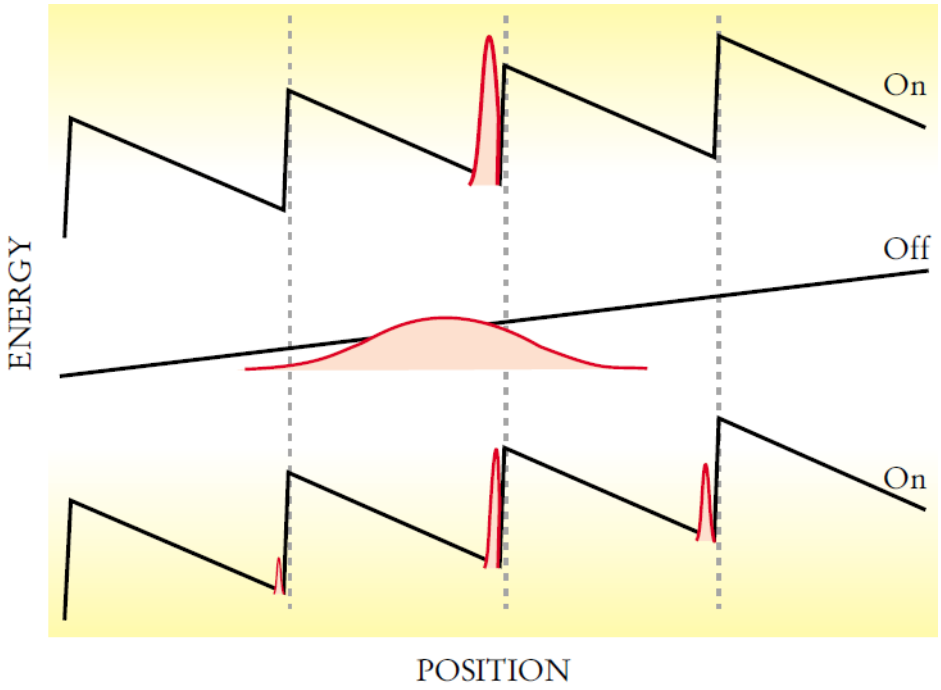

Figure 1.1: Operational principle of a flashing ratchet with dc-bias. Figure taken from [20]

spin transport [31] and for atoms loaded into optical lattices in one dimension [32–39] and in 2D [40].

In the absence of noise one speaks of "deterministic ratchets" and the conditions under which a directed transport of particles is possible depend on whether there is friction in the system or not. In the dissipative regime the underlying mechanism responsible for the existence of directed currents and the reversal of the transport has been identified in Refs. [41–43]. Due to dissipation transporting attractors in phase space emerge and by choosing the initial conditions appropriately it is possible to populate them selectively. If no friction is present, the systems are called "Hamiltonian ratchets". In this case a directed transport of particles can occur only if certain spatiotemporal symmetries of the driven potential are broken which have been identified in Ref. [44]. Accordingly, if the potential is invariant under a generalized parity- and time-reversal transformation, no ratchet effect will occur because it is then possible to construct for every trajectory a mirror-image with the opposite sign of the velocity such that an average over a representative set of particles yields zero transport. Yet, breaking both symmetries does not evoke coercively the ratchet effect because it is not a sufficient criterion for the existence of transport. Subsequently, the transport properties of Hamiltonian systems [45–53] have been studied thoroughly. It has been shown that a necessary condition for the occurrence of directed transport in the classical regime is the existence of a mixed phase space with chaotic and regular regions [46]. The authors derived in [45,46,51] sum formula which predicts the transport velocity of a classical ensemble of particles. Moreover, in Ref. [54] the influence of an additional dc bias on the directed transport of a Hamiltonian ratchet has been studied. The authors have found the persistence of transporting invariant sub-manifolds like regular islands. In their vicinity trajectories can

get sticky, such that they perform ballistic-like motion. Remaining chaotic trajectories are accelerated by the bias field getting separated very fast from the ballistic type dynamics.

In the quantum regime both dissipative [55–57] and Hamiltonian ratchets [45,46,51,58–62] have attracted a lot of attention during the last decade whereas the Hamiltonian case is of special interest due to several reasons. Contrary to the classical case a quantum transport is possible for Hamiltonian systems with fully chaotic dynamics which has been shown in [63–65]. Moreover, the underlying mechanism of a Hamiltonian quantum ratchet has been exploited for a very recent theoretical proposal of a "quantum motor" [66]. In general, the control over transport properties on the nanoscale is accompanied by the growing importance of quantum effects. At the same time one typically wants to reduce dissipation as much as possible since it induces heating, i.e. the quantum ratchet should operate in the Hamiltonian regime. As previously mentioned, the archetypical ratchets which are for instance experimentally realized in [37] consist of a one-dimensional lattice perturbed by a periodic time-dependent driving. Due the temporal periodicity of the Hamiltonian the time-dependent Schrödinger equation can solved by means of Floquet theory [67–69] and the quantum current depends on the properties of the so-called Floquet modes and the quasi-energy spectrum [46, 51, 60]. It is observed that by breaking the fundamental spatiotemporal symmetries of the potential, derived in [44], the Floquet modes and the quasi-energy spectrum are desymmetrized which leads to the occurrence of directed transport [46, 51, 60]. In Ref. [60] the impact of avoided crossings between different transporting Floquet states has been considered. Tuning the control parameters of the system leads to an enhancement or suppression of the current flow. Yet, all previously discussed Hamiltonian ratchets (classical and quantum) have in common that the driving is globally, i.e. the force which acts on the particles can be written as a sum or a product of two functions depending only on the spatial coordinate and the time, i.e. $F(x,t) \propto f(x) + g(t)$ or $F(x,t) \propto f(x) \cdot g(t)$. Consequently, it is an intriguing perspective to consider the consequences of a breaking of the generalized parity and time-reversal symmetry established in [44] inhomogeneously by applying a spatially varying driving force.

Objective of this work

In this thesis we study the non-equilibrium dynamics of spatiotemporally driven lattices consisting of laterally oscillating potential barriers whereas we focus on the impact of local driving forces on the classical and the quantum dynamics. In the classical regime we consider the question how the phase space of the system gets manipulated by a local driving. On the one hand we find that by equipping the harmonic driving laws of the barriers with spatially varying phase shifts a directed current of particle can be evoked although there is no net force and each barrier is non-transporting itself. On the other hand, one can get localized chaotic dynamics between neighboring barriers, i.e. particles in these localized chaotic seas are trapped on specific positions in the lattice which can be controlled by choosing appropriate local drivings. Moreover, we study so-called "block-structured lattice" which are composed of domains with different driving laws, transport properties and local phase spaces. At the interfaces between the domains we find that classical trajectories can experience crossovers from diffusive to ballistic motion and vice versa. These dynamical conversion processes induce long-time transient oscillations of the particle density which can be converted into a propagating density wave by tuning the driving forces. In the quantum regime we have

implemented a numerical scheme based on Floquet and Bloch theory in order to obtain the time-evolution operator. We have studied the quantum transport properties and observed that a harmonic driving for each barrier together with local phase shift is sufficient to evoke a nonzero current.

In detail, the thesis is structured as follows:

- In the **second chapter** we introduce the Hamiltonian of a spatiotemporally driven lattice and show how the phase space flow can be described by an implicit mapping. We discuss briefly the dynamics of the precursor of the driven lattice which is a single laterally oscillating potential barrier. Finally, the symmetry properties of the driven lattice are addressed and we study how the spatiotemporally symmetries [44] which forbid transport in the classical regime can be broken by modulating spatially the time-dependent driving force.
- The **third chapter** is devoted to the phase space analysis. In this part we study how the local driving leaves its hallmarks in the appearance of the classical phase space of the system. We show that by appropriately choosing the driving laws of the potential barrier one can "engineer" the phase space in a controllable manner, i.e. we can manipulate certain parts of the space wheres the remaining portion remains mainly unaffected. By means of a kinematic consideration concerning the scattering dynamics of a single potential barrier we derive a formula predicting the position of the tori delimiting the main chaotic phase space component and compare the formula's prediction to the position of the tori in the Poincaré surfaces of section. In the end we discuss briefly why chaotic trajectories in the driven lattice obey typically intermittent dynamics, i.e. the diffusive dynamics is interrupted by episodes of long ballistic motion.
- We discuss in the **fourth chapter** the transport and the localization properties of particles in the locally driven lattice. We find that a harmonic driving law applied to the potential barriers together with local phase shifts is sufficient to create a directed current of particles although each single barrier is non-transporting. The magnitude and the direction of the current can be controlled by the parameters of the driving or of the static lattice. Several mechanisms for transient localization of particles in different wells of the driven unit cell are presented and we outline how it can be converted into permanent trapping of particle at certain positions of the lattice.
- In the **fifth chapter** we discuss the classical dynamics of block-structured driven lattices which consist of domains equipped with different driving force and thus possessing other transport properties. We find that at the interfaces between the domains particles can experience a change in their dynamical character (diffusive / ballistic). For the non-equilibrium dynamics of an ensemble these conversion processes cause a transient periodic modulations of the particle density possessing local minima and maxima in a domain. By an appropriate tuning of the driving forces these density modulations can be rendered into a time-propagating wave of particles .
- The **sixth chapter** is devoted to the quantum dynamics of spatiotemporally driven lattices. We implement a numerical scheme for solving the time-dependent Schrödinger equation based on Floquet and Bloch theory. Afterwards, we analyze the quasi energy spectrum and discuss the properties of the quantum transport for different setups. For lattices where the spatiotemporally symmetries of the potential are broken by the driving we find that the asymptotic average current acquires a nonzero value. The

direction and the magnitude of this transport can be tuned by varying the frequency of the driving.

Finally, we conclude and give a brief outlook.

Chapter 2

Lattice of laterally oscillating barriers

In this chapter we introduce the physical system which we investigate. Firstly, the Hamiltonian of the setup is defined and the numerical scheme for propagating the equations of motion is explained. Secondly, we summarize the dynamical properties of the single driven barrier and discuss the symmetries of the lattice.

2.1 General definitions and Hamiltonian

The classical dynamics of an ensemble of identical, non-interacting particles in a one-dimensional, infinitely extended lattice of laterally oscillating square potential barriers of equal height V_0 and width l is described by the Hamiltonian

$$H(x,p,t) = \frac{p^2}{2m} + V(x,t), \tag{2.1}$$

where m is the mass of the particles and

$$V(x,t) = \sum_{i=-\infty}^{\infty} V_0 \Theta\left(\frac{l}{2} - |x - x_{0,i} - f_i(t)|\right) \tag{2.2}$$

is the potential. $x_{0,i}$ is the equilibrium position and $f_i(t)$ is the so-called driving law of the i-th barrier. Accordingly, $f_i(t)$ is a periodic function which is explicitly allowed to depend on the site index i and thus each barrier can be in general driven in a different way. For the equilibrium position of the potentials we choose

$$x_{0,i} = i\,D \quad \text{with} \;\; D > 0, \tag{2.3}$$

such that the static counterpart of Hamiltonian (2.1) is an equally spaced lattice of identical barriers, i.e. in their equilibrium position the barriers are centered around $\{0, \pm D, \pm 2D, \ldots\}$. Fig. 2.1 shows an illustrative sketch of the system including the relevant parameters. For the driving law $f_i(t)$ we choose one of the harmonic functions

$$f_i(t) = C\cos(\omega t + \varphi_i), \tag{2.4}$$

$$f_i(t) = C\left\{\cos(\omega t + \varphi_i) + \sin(2(\omega t + \varphi_i))\right\}, \tag{2.5}$$

where $\varphi_i \in [0, 2\pi]$ is a local phase shift that depends on the lattice site index of the i-th barrier. In the following the amplitude C and the frequency ω are always equal for all sites i and we change the lattice by choosing different phase shifts $\{\varphi_i\}$. If the barriers have the same initial phase shift, e.g. $\varphi_i = \varphi_0$ for all site indices i, the lattice will be equidistant at

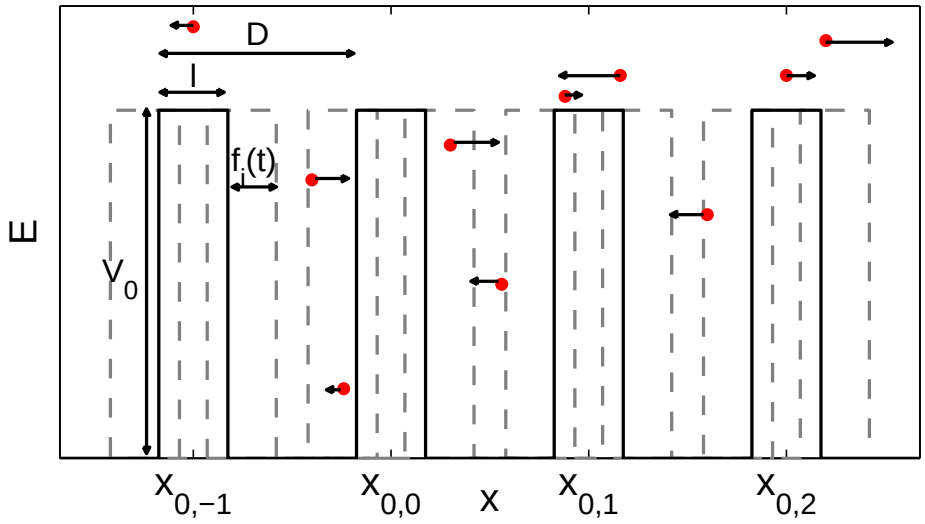

Figure 2.1: Schematic illustration of the lattice of laterally oscillating barriers.

all times. We will refer to this special case as "uniformly oscillating lattice". To ensure that neighboring potentials do not touch or overlap for arbitrary phase shifts $\{\varphi_i\}$, the amplitude of oscillation must not be too large, i.e. $\max|f_i(t)| \leq \frac{D-l}{2}$.

2.2 Mapping of the phase space flow

In order to study the dynamics of an ensemble of particles in the lattice described by the Hamiltonian (2.1), we have to solve the equations of motion

$$\dot{x} = \frac{\partial H}{\partial p} \tag{2.6}$$

$$\dot{p} = -\frac{\partial H}{\partial x}, \tag{2.7}$$

which for smooth potentials are usually integrated by a Runge-Kutta-method. However, in our case these "numerical standard-techniques" cannot be applied straightforwardly since $V(x,t)$ is discontinuous and thus the force $F(x,t) = -\partial V(x,t)/\partial x$ is delta-shaped [70], i.e.

$$V(x,t) \propto \Theta(x,t) \Rightarrow F(x,t) \propto \delta(x,t). \tag{2.8}$$

Instead, we exploit the fact that the particles move ballistically between consecutive collisions with the barriers' edges. Therefore, the Hamiltonian flow in the three-dimensional phase space can be described by an implicit mapping $\mathcal{M}$ from one barrier-particle interaction to the next one [70, 71], i.e.

$$\begin{pmatrix} x_{n+1} \\ p_{n+1} \\ t_{n+1} \end{pmatrix} = \mathcal{M} \begin{pmatrix} x_n \\ p_n \\ t_n \end{pmatrix}, \tag{2.9}$$

where x_n is the particle's position, p_n its momentum and t_n the time straight after the n-th collision. In the following we describe briefly how the mapping $\mathcal{M}$ is iterated:

t_{n+1} is derived from the condition that the position

$$x_p(t_{n+1}) = x_n + v_n(t_{n+1} - t_n) \tag{2.10}$$

of a particle travelling with velocity $v_n = \frac{p_n}{m}$ equals at this point in time to the position of an edge of the i-th barrier in whose scattering region the particle is at time t_n (see Fig. 2.1), i.e.

$$x_{b,i}(t_{n+1}) = x_{0,i} \pm \frac{l}{2} + f_i(t_{n+1}). \tag{2.11}$$

The $+/-$ sign has to be chosen for the right/left edge of the i-th barrier, respectively. Accordingly, t_{n+1} is the solution of the following equation

$$x_{0,i} \pm \frac{l}{2} + f_i(t_{n+1}) = x_n + v_n(t_{n+1} - t_n), \tag{2.12}$$

where we have to take the smallest $t_{n+1} > t_n$ since this corresponds to the physical reasonable collision. For the chosen harmonic driving laws (2.4) and (2.5) Eq. (2.12) is not analytically solvable and therefore numerical methods must be applied to find t_{n+1}. To this end Eq. (2.12) is rewritten as the root-finding problem $g(t_{n+1}) = 0$ with

$$g(t_{n+1}) = x_{0,i} \pm \frac{l}{2} + f_i(t_{n+1}) - x_n - v_n(t_{n+1} - t_n). \tag{2.13}$$

If no solution $t_{n+1} > t_n$ exists, the particle will leave the scattering region of the i-th barrier and we have to calculate the collision time t_{n+1} with a neighboring potential. Depending on the parameters v_n, x_n etc. Eq. (2.13) can have many solutions. In order to ensure that we find the smallest solution $t_{n+1} > t_n$, it is mandatory to provide a so-called "bracketing" for this sought after root, i.e. by exploiting the properties of the function $g(t_{n+1})$ we have to determine a unique interval $[t_1, t_2]$ which contains only the first solution of Eq. (2.13). Although at first glance this seems to be a straightforward task for a one-dimensional root-finding problem, it is nevertheless non-trivial, because it is possible that some of the solutions of Eq. (2.13) lie very close together. If a bracketing is on hand, the root can be traced by means of several algorithms. We have chosen the "Van Wijngaarden-Dekker-Brent method" which is described in Ref. [72]. The details of the bracketing scheme can be found in [71].

Once we have found the collision time t_{n+1} the next position of the particle x_{n+1} is calculated simply by inserting t_{n+1} in Eq. (2.11), i.e.

$$x_{n+1} = x_{0,i} \pm \frac{l}{2} + f_i(t_{n+1}). \tag{2.14}$$

To derive the momentum after the next collision p_{n+1} we must distinguish two different cases [70]. Let us assume that the particle is outside of the barrier before the collision occurs. If its relative kinetic energy at t_{n+1} is smaller than the potential height, that is

$$E_{kin,rel} = \frac{m}{2}\left(v_n - v_{b,i}(t_{n+1})\right)^2 < V_0 \tag{2.15}$$

with $v_{b,i}(t_{n+1}) = \dot{x}_{b,i}(t_{n+1})$ being the barrier's velocity, an elastic reflection will occur. In this case the new velocity v_{n+1} becomes

$$v_{n+1} = 2v_{b,i}(t_{n+1}) - v_n. \tag{2.16}$$

If $E_{kin,rel}$ exceeds V_0, the particle will enter the potential and lose kinetic energy. Simple algebra yields the following equation for the new velocity

$$v_{n+1} = v_{b,i}(t_{n+1}) + \mathrm{sign}(v_n - v_{b,i}(t_{n+1}))\sqrt{(v_n - v_{b,i}(t_{n+1}))^2 - \frac{2V_0}{m}} \tag{2.17}$$

Conversely, if the particle is inside of the potential before the collision occurs, it will leave the barrier and v_{n+1} is then given by

$$v_{n+1} = v_{b,i}(t_{n+1}) + \mathrm{sign}(v_n - v_{b,i}(t_{n+1}))\sqrt{(v_n - v_{b,i}(t_{n+1}))^2 + \frac{2V_0}{m}} \tag{2.18}$$

In both cases the new momentum is simply calculated by $p_{n+1} = mv_{n+1}$. Hence, an orbit in phase space is given by an infinite sequence of points

$$\mathcal{O} = \{(x_0, p_0, t_0)^t, \ldots, (x_n, p_n, t_n)^t, \ldots\}. \tag{2.19}$$

Before we proceed with the infinite lattice it is helpful to summarize briefly the properties of the single driven barrier.

2.3 Single driven barrier

Omitting the sum in Eq. (2.1) and choosing $x_0 = 0$ yields obviously the Hamiltonian of a single barrier which laterally oscillates around the origin. The dynamics of the particles in this system is described as well by the previously introduced mapping $\mathcal{M}$. We only have to bear in mind that the particles can leave the scattering region of the barrier and thus the sequence representing an orbit in phase space $\mathcal{O}$ is in general finite. In Ref. [70] the authors have shown that the laterally oscillating barrier with pure cosine driving $f(t) = \cos(t)$ possesses in certain regions of the parameter space a regular island in phase space associated with trapped dynamics in its scattering region. It is important to remark that the elliptic island appears only for curved driving laws, i.e. for a sawtooth-like oscillation where the potential moves with constant velocity between its turning points this elliptic islands is not present in phase space [70]. In Fig. 2.2(a) such an elliptic island for a purely harmonic driving $f(t) = \cos(t)$ is shown. In its center a periodic orbit resides. Furthermore, we observe an eye-catching embedded chain of five sub-island. For an initial condition chosen in one of the five islands the typical dynamics of the trajectory in real space is shown in Fig. 2.2(b). As we see, the particle moves synchronously with the oscillation of the potential and is trapped forever. Outside of the elliptic island the phase space is chaotic, i.e. these scattering particles leave the region covered by the barrier oscillation typically after a few collisions. Still, there are also exceptions, i.e. particles which remain for a very long time in the scattering region and this effect is discussed in the following. In Ref. [70] it has been shown that the laterally driven barrier is a chaotic scatterer which yields singularities of the dwell time, i.e. the time that the

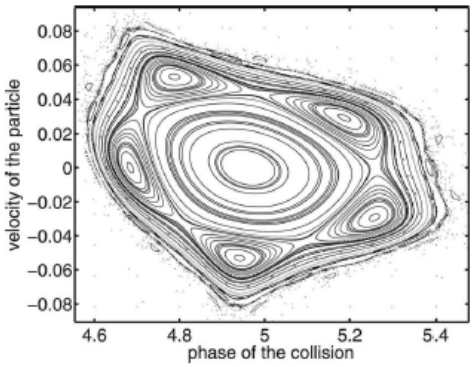

(a) Regular island in the phase space of the single oscillating barrier for $l = 0.4$, $V_0 = 0.32$ and a pure cosine driving $f(t) = \cos(t)$.

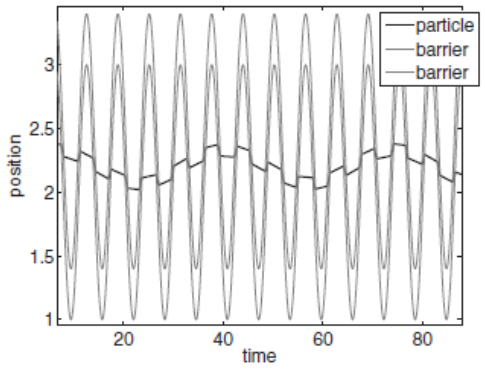

(b) Typical trajectory in real space for an orbit in the island shown in figure 2.2(a)

Figure 2.2: Figures taken from Ref. [70]

particles spend in the interaction region. The authors explain this behavior by the existence of the elliptic island. Accordingly, scattering particles whose initial conditions overlap with the stable manifold of unstable periodic orbits in phase space surrounding the elliptic island are guided on the manifold towards the islands. Once in its vicinity they trace the outermost torus for a very long time which is called "stickiness" [73, 74]. Finally, the particles leave the interaction region again on the unstable manifold which yields in conclusion a strong delay between the entering and the exiting of the scattering region. In the discussion of the diffusion of the lattice we will see that these scattering properties leave there their hallmark. As a matter of course all the aforementioned points are still true when the barrier oscillates biharmonically according to $f(t) = C\{\cos(\omega t) + \sin(2(\omega t))\}$ because this driving law is also curved and similarly permits the existence of an elliptic island in phase space. Let us now return to the discussion of the dynamics of particles in the infinite lattice.

2.4 General symmetries of the lattice

One aspect of this thesis are the transport properties of the driven lattice described by the Hamiltonian (2.1). Let us therefore discuss under which conditions directed transport can occur. In Ref. [44], the authors have proven that the directed current will vanish, if the equations of motion are invariant under certain transformations, i.e. if certain symmetries hold. These transformations change the sign of the velocity and as a result it is possible to construct for every trajectory a mirror image with the opposite sign for the velocity. In this case, averaging over a representative set of trajectories yields zero mean velocity, that is a vanishing directed transport. Such transformations reverse either time or spatial coordinates together with a constant shift. Thus they take on the appearance

$$T_a : x \to -x + c_x, \;\; t \to t + c_t, \tag{2.20}$$

$$T_b : x \to x + c_x, \;\; t \to -t + c_t. \tag{2.21}$$

The equations of motion (2.6)-(2.7) derived for the Hamiltonian (2.1) can be simply rewritten as

$$m\ddot{x} = -\frac{\partial V(x,t)}{\partial x}. \tag{2.22}$$

For the absence of directed transport due to symmetry reasons it is therefore necessary that the potential $V(x,t)$ is invariant under one of the transformations (2.4)-(2.21). We remark that a vanishing current can also occur if the above symmetries do not hold, which is however a non-generic case and is encountered only for specifically chosen parameter values. In the case of the uniformly oscillating lattice, i.e. $\varphi_i = \varphi_0$ for all lattice sites i, the potential reads

$$V(x,t) = \sum_{i=-\infty}^{\infty} V_0 \Theta\left(\frac{l}{2} - |x - iD - f_i(t)|\right) \tag{2.23}$$

For the monochromatic harmonic driving law (2.4) (i.e. $f_i(t) = C\cos(\omega t + \varphi_0)$) we see immediately that $V(x,t)$ possesses the generalized time-reversal symmetry, that is

$$\begin{aligned} V(x, -t - \frac{2\varphi_0}{\omega}) &= \sum_{i=-\infty}^{\infty} V_0 \Theta\left(\frac{l}{2} - |x - iD - C\cos(-(\omega t + \varphi_0))|\right) && (2.24)\\ &= \sum_{i=-\infty}^{\infty} V_0 \Theta\left(\frac{l}{2} - |x - iD - C\cos(\omega t + \varphi_0)|\right) && (2.25)\\ &= V(x,t). && (2.26) \end{aligned}$$

According to Eqs. (2.4) and (2.21) the presence of this symmetry is already sufficient to rule out directed transport. Yet, for the sake of completeness we remark that the potential is also invariant under the generalized parity transformation, i.e.

$$\begin{aligned} V(-x, t + \frac{\pi}{\omega}) &= \sum_{i=-\infty}^{\infty} V_0 \Theta\left(\frac{l}{2} - |-x - iD + C\cos(\omega t + \varphi_0)|\right) && (2.27)\\ &= \sum_{j=-\infty}^{\infty} V_0 \Theta\left(\frac{l}{2} - |x - jD - C\cos(\omega t + \varphi_0)|\right) && (2.28)\\ &= V(x,t), && (2.29) \end{aligned}$$

where we have redefined $j = -i$ in the second step. Summing up, two transformations under which the potential is invariant can be identified

$$\begin{aligned} T &: x \to -x, \;\; t \to t + \frac{\pi}{\omega},\\ T' &: x \to x, \;\; t \to -t - \frac{2\varphi_0}{\omega}. \end{aligned} \tag{2.30}$$

Consequently, for the monochromatically, uniformly oscillating lattice no directed transport occurs. The same will be true, if the local phase shifts of the barriers alternate, i.e.

$$\varphi_i = \begin{cases} \varphi_1 & \text{if } i \text{ is even} \\ \varphi_2 & \text{else.} \end{cases} \tag{2.31}$$

with $\varphi_1 \neq \varphi_2$. In this case the transformation is given by

$$T : x \to x + D, \;\; t \to -t - \frac{\varphi_1 + \varphi_2}{\omega}. \tag{2.32}$$

To verify this claim we write the potential as

$$\begin{aligned} V(x,t) = &\sum_{\text{even}} V_0 \Theta \left(\frac{l}{2} - |x - iD - C\cos(\omega t + \varphi_1)| \right) \\ &+ \sum_{\text{odd}} V_0 \Theta \left(\frac{l}{2} - |x - iD - C\cos(\omega t + \varphi_2)| \right) \end{aligned} \tag{2.33}$$

and apply the transformation given by Eq. (2.32) which yields

$$\begin{aligned} V(x + D, -t - \tfrac{\varphi_1 + \varphi_2}{\omega}) = &\sum_{\text{even}} V_0 \Theta \left(\frac{l}{2} - |x - (i-1)D - C\cos(\omega t + \varphi_2)| \right) \\ &+ \sum_{\text{odd}} V_0 \Theta \left(\frac{l}{2} - |x - (i-1)D - C\cos(\omega t + \varphi_1)| \right). \end{aligned} \tag{2.34}$$

To see the equivalence of Eq. (2.33) and (2.34) we point out that for the sum over the even numbers in (2.34) the barrier indices are $i - 1$ which is odd. For the other case, i.e. the sum over the odd numbers, $i - 1$ is even. Hence, both equations are equivalent and the potential is thus invariant under transformation (2.32). Consequently, the monochromatically driven lattice with alternating phase shifts shows no directed transport, too.

For more complicated phase shifts like sequences with higher periods n, that is $\varphi_{i+n} = \varphi_i$ and $\varphi_i \neq \varphi_j$ for $i, j = 1, 2, \ldots, n$ it is generally impossible to find transformations of type (2.4) and (2.21) under which the potential is invariant. Therefore, a directed transport is possible to be evoked in such setups. Still, we emphasize again that breaking the symmetries (2.4) and (2.21) is only a necessary but not a sufficient criterion for the occurrence of a particle current.

When the lattice is driven according to the biharmonic law (2.5), it is impossible to define proper c_t and c_x such that the potential $V(x,t)$ is invariant under one of the transformations and (2.21) even if we choose constant phase shifts, i.e. $\varphi_i = \varphi_0$ for all i. Therefore, we expect that the bichromatically, uniformly oscillating lattice shows a particle current. Let us now proceed to the discussion of the phase space of Hamiltonian 2.1.

Chapter 3

Phase space analysis

In this chapter we present an analysis of the phase space of the Hamiltonian (2.1) for setups which are introduced in the following section. General characteristics of the Poincaré surfaces of section (PSS), like the appearance of regular islands and the chaotic sea, are discussed. Especially, main emphasis is placed on the comparison of the phase space properties of the setups which possess one of the symmetries (2.4)-(2.21) and those who do not. Furthermore, the stability of the phase space structures against perturbation of the phase pattern is studied.

3.1 Setup

In Sec. 2.1 we introduced the two driving laws which are investigated in the following, i.e. a pure cosine and a biharmonic driving (see Eqs. (2.4) and (2.5)). In order to reduce the number of varying parameters, we set the frequency of the driving to $\omega = 1$. Additionally, C is chosen such that the amplitude of the driving is one, i.e. $\max|f_i(t)| = 1$. For the monochromatic law (2.4) this implies $C = 1$ and $C \approx 0.57$ in the case of the biharmonic driving (2.5). Moreover, the barriers' width and the equilibrium distance are fixed to $l = 0.4$ and $D = 4.4$, respectively. Finally, without loss of generality the mass of the particles is chosen $m = 1$. We are therefore left with two parameters: the barrier height V_0 and the local phase shifts $\{\varphi_i\}$. Since one of our interests are the lattice's transport properties, we choose setups for which the symmetries (2.4)-(2.21) are broken, because this is necessary to obtain directed currents. If the barriers are driven according to the monochromatic law (2.4), this symmetry breaking is implemented by spatially modulating the phase shifts $\{\varphi_i\}$. For the biharmonic driving (2.5) a constant phase, i.e. $\varphi_i = \varphi_0$, is sufficient to break both symmetries (2.4)-(2.21). In the following, four different setups are studied in detail:

(a) *constant phase gradient*: The potential height is fixed to $V_0 = 0.16$ and the barriers are equipped with a linearly increasing phase,

$$f_i(t) = \cos\left(t + \frac{i}{n}2\pi\right), \tag{3.1}$$

where the periods of the site-dependent phases (which we call "phase periods" for reasons of brevity) are $n = 1, 3, 6, 10$. For $n = 3$, the sequence of phase shifts $\{\varphi_i\}$ is $\{\ldots, 0, \frac{2\pi}{3}, \frac{4\pi}{3}, 0, \frac{2\pi}{3}, \ldots\}$, whereas for $n = 1$ a lattice of uniformly oscillating barriers is recovered. One can verify straightforwardly that the potential is not invariant under one of the transformations (2.4)-(2.21) for phase periods greater than or equal to three. Hence, a nonzero mean velocity can be expected for $n = 3, 6, 10$.

(b) *perturbed phase gradient*: For the second class of setups we keep $V_0 = 0.16$ and the above phase gradient with period three setup is perturbed, i.e. the sequence of phase shifts

becomes $\{\ldots, 0, \frac{2\pi}{3} \pm \alpha, \frac{4\pi}{3}, 0, \frac{2\pi}{3} \pm \alpha, \ldots\}$ such that for $\alpha = 0$ the equidistant phase gradient is recovered.

(c) *broken phase gradient*: A specific phase shift sequence of period three $\{\ldots, 0, \frac{\pi}{10}, \frac{3\pi}{10}, 0, \frac{\pi}{10}, \frac{3\pi}{10}, \ldots\}$ is chosen and the global potential height V_0 is varied.

(d) *Biharmonic driving*: We choose $V_0 = 0.16$ for all barriers, take a constant phase shift $\varphi_i = 0$ for all barriers i and apply the biharmonic driving (2.5), i.e.

$$f_i(t) = 0.57\,\{\cos(t) + \sin(2t)\} \tag{3.2}$$

3.2 Phase space topology

In this section the phase space topology is analyzed. Firstly, the method, how the Poincaré surfaces of section (PSS) for the above defined setups are obtained, is described briefly. Afterwards, we discuss the structure of the PSSs and address the question how breaking the symmetries (2.4)-(2.21) leaves its hallmarks.

3.2.1 Poincaré surfaces of section

In Sec. 2.2 we have seen that the orbit in phase space of an arbitrary trajectory is given by the infinite sequence of points

$$\mathcal{O} = \{(x_0, p_0, t_0)^t, \ldots, (x_n, p_n, t_n)^t, \ldots\}. \tag{3.3}$$

It is obviously impossible to plot $\mathcal{O}$ on a two-dimensional sheet. Thus, in order to visualize the dynamics we make so-called Poincaré surface of sections (PSS) of the phase space [5]. Due to the time-periodicity of the Hamiltonian $H(x, p, t + T) = H(x, p, t)$, $(T = 2\pi)$, an area-preserving surface of section is obtained by taking stroboscopic "snapshots" of the (x, p)-plane at times $t = n\,T$ with $n \in \mathbb{N}$. Additionally, the Hamiltonian possesses the translation invariance $H(x+L, p, t) = H(x, p, t)$, where L is the length of the system's unit cell. Generally, L is not the distance between the barriers at their equilibrium positions, but for our chosen setups L is a multiple of D, $L = n \cdot D$, where n is the phase period. Thereby, the space coordinate can be restricted to the length L of the Hamiltonian's unit cell. The desired Poincaré surface of section is then provided by the set of points:

$$\mathcal{M} = \{(x(t + kT) \bmod L, p(t + kT)) | k \in \mathbb{N}\}. \tag{3.4}$$

By means of the sequence of phase space points $\mathcal{O}$ the momentum and the position of a particle at any time can be derived straightforwardly. $p(t + kT)$ is obviously given by $(x_i, p_i, t_i)^t \in \mathcal{O}$ with $t_i \leq t + kT$, i.e. $p(t + kT) = p_i$. Furthermore, the particle's position at time $t + kT$ is calculated straightforwardly via

$$x(t + kT) = x_i + \frac{p_i}{m}(t + kT - t_i). \tag{3.5}$$

Since the time between successive "snapshots" of the (x, p)-plane is equal, the PSS is done for a specific phase of the driving. It is therefore not surprising that the appearance of the surface of section is not universal but depends on exactly this phase. An example of how this manifests itself in the PSS is given in the next section.

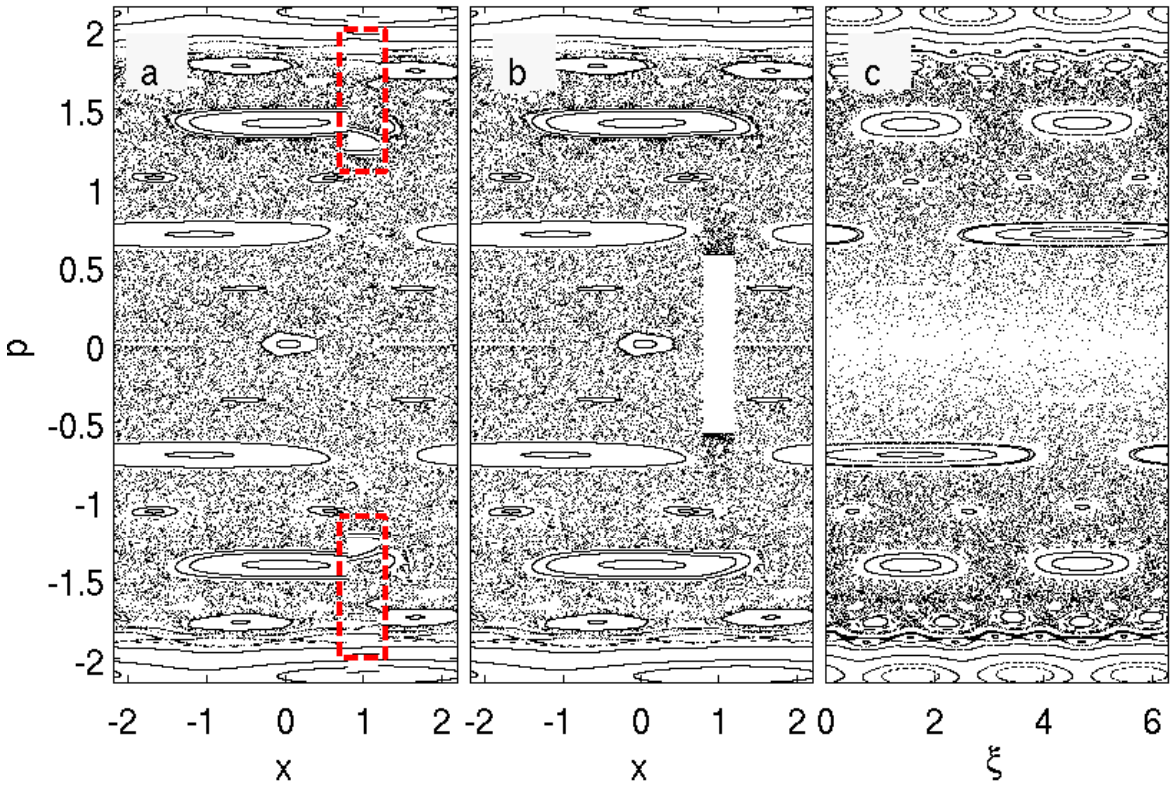

Figure 3.1: (a) Stroboscopic PSS of the lattice of uniformly oscillating square potentials. For a better illustration we have added in (b) the potential energy to the kinetic energy of the particles, in order to avoid the discontinuities in the "regular" PSS. Figure (c) shows the PSS where we record time and momentum of particle once they cross equidistant positions in real space (see Sec. 3.2.1).

For later purposes it is moreover convenient to introduce a further scheme to perform Poincaré surface of sections of the phase space. For a uniform driving without a phase gradient the lattice possesses the translation invariance with the equilibrium distance of two adjacent barriers, i.e. $L = D$. In this case another PSS can be done by recording the time and the velocity of a particle every time it crosses equidistantly spaced positions in real space. Since the Hamiltonian has the property $H(x, p, t + T) = H(x, p, t)$ we can additionally map the recorded time to the period of the driving T, i.e. we can just as well record the phase of the driving when a trajectory crosses certain positions $\xi(x+kL)$. Accordingly, this procedure yields that the PSS is given by the following set of points:

$$\mathcal{M} = \{(\xi(x + kL), p(x + kL))|k \in \mathbb{N}\}. \tag{3.6}$$

Along the lines of the PSS presented before we exploit the mapping of the dynamics (see Eq. (2.9)) in order to determine the time and the momentum of a particle once it crosses one of the positions $x+kL$ which make up the PSS. Let us assume that in the course of the dynamics two consecutive phase space points $(x_i, p_i, t_i)^t, (x_{i+1}, p_{i+1}, t_{i+1})^t \in \mathcal{O}$ have the property that $x_i < x + kL < x_{i+1}$. The momentum of the particle in the PSS is then $p(x + kL) = p_i$ and

the time is given by

$$t(x + kL) = t_i + \frac{x + kL - x_i}{p_i/m}, \tag{3.7}$$

which is converted to the phase of the driving via $\xi(x + kL) = \omega t(x + kL) \bmod 2\pi$. Similarly to the stroboscopic PSS the appearance of the "momentum versus phase" PSS depends on the position in real space where we record t and p of the trajectories. We will use the term "Poincaré surface of section" (PSS) without additional definite specification because it is always clear from the context which one is meant.

3.2.2 Monochromatically, uniformly driven lattice

In Fig. 3.1 (a) the stroboscopic PSS of the monochromatically driven lattice with a phase period one, i.e. a lattice of uniformly oscillating barriers ($n = 1$, $L = D$, $f_i(t) = \cos(t)$) is shown. The Poincaré surface of section possesses discontinuities (dashed box in Fig. 3.1 (a)), which are due to the fact that the particles are either inside or outside the barrier when the snapshot of the (x, p)-plane is taken. The particles have $E_{pot} = 0$ outside and $E_{pot} = V_0$ inside. Since the potential is not smooth, this provides discontinuities in the PSS. For illustrative reasons it is therefore useful to add the potential energy $E_{pot} = V_0$ to the kinetic energy for those particles, which are inside the barrier at the moment of the snapshot. This has been done in Fig. 3.1 (b). The invariant curves are then continuous, yet the barrier can be seen as a blank squared region in the PSS. To avoid the discontinuities all the subsequent stroboscopic PSS are presented in this way.

Another eye-catching feature of the PSS is the reflection symmetry with respect to $p = 0$. However, this is not universally valid, but occurs only for specific phases of the snapshot of the (x, p)-plane. As Fig. 3.1 (b) shows, the PSS is done at the moment the barrier arrives at one of its turning points, i.e. the i-th barrier is centered around $x_{0,i} = iD + C$ at this point in time. For the first unit cell $i = 0$, this yields $x_{0,0} = 1$ (blank squared region in Fig. 3.1 (b)). If the PSS is made, for instance, when the barrier has its maximum velocity, then this symmetry is absent. Yet, the dynamics of the lattice of uniformly oscillating barriers can be completely classified by means of the stroboscopic Poincaré surface of section [5].

For large momenta $|p| \gg 1$ the potential is negligible due to its finite height. In this limit, the integrable dynamics of a free particle is recovered and the phase space is foliated by invariant curves, which are topologically equivalent to a torus [75]. In the PSS these curves appear as straight lines, which stretch out over the whole unit cell. This simple part of the PSS is not displayed in Fig. 3.1 (b) and occurs for $|p| \geq 3$. With decreasing momentum, the integrability is lost, but large regular domains remain. Many orbits still lie on deformed tori, which occur as curved lines in the PSS ($|p| \approx 2$ in Fig. 3.1 (b)). Particles on these invariant curves travel through the lattice in the direction of their initial momentum. Indeed the KAM theorem, which predicts the persistence of quasi-periodic motion in Hamiltonian dynamical systems under a small perturbation, states that tori with sufficiently irrational winding number survive under a small perturbation [75]. The winding number is defined as the limit

$$w = \lim_{t\to\infty} \frac{x(t) - x(0)}{t}, \tag{3.8}$$

if it exists [76]. x and t are measured in multiples of the spatial period of the unit cell and time period, respectively. Thus w is proportional to the average velocity of the particle in the

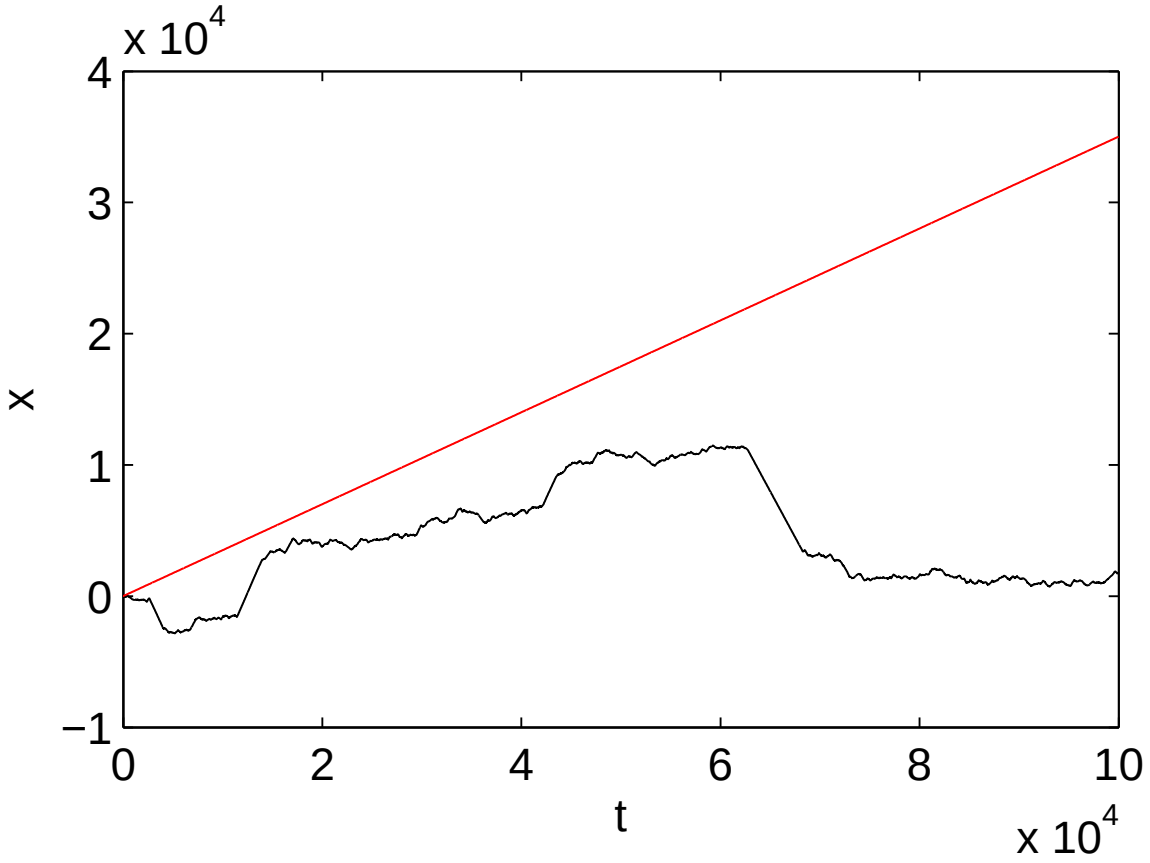

Figure 3.2: Two trajectories in the monochromatically driven lattice for $V_0 = 0.16$, $l = 0.4$ and $L = 4.4$. The black curve corresponds to a particle which has initially been started in the chaotic sea, i.e. $x(0) = -2.2$, $p(0) = 0.3$. The red curve corresponds to a ballistic trajectory placed initially in one of the two elliptic islands belonging to winding number $w = \frac{1}{2}$, that is $x(0) = -0.54$, $p(0) = 0.35$.

lattice, $w \sim \overline{v}$ [51]. Tori with rational winding numbers $w = r/s$ are excluded in the KAM theorem. According to the Poincaré-Birkhoff theorem they dissolve into an even number of alternately elliptic and hyperbolic fixed points of period s. The trajectories in the extended system, which correspond to these periodic orbits in the PSS, travel r spatial unit cells in s time periods in the direction of their initial velocity. Hence in the PSS they occur as s distinct points. Around each elliptic periodic orbit there is again a set of invariant curves, which can be seen in our PSS as elliptic islands. Completely analogous to the trajectory belonging to the periodic orbit in the center of this structure, the motion of particles, which are inside these islands proceeds through the lattice only in one direction. Accordingly, the trajectories intersect the PSS sequentially at different islands of the corresponding chain of islands. For example in Fig. 3.2 the red curve is the trajectory in real space corresponding to the central period two orbit in the $w = \frac{1}{2}$ elliptic islands at $p = 0.35$, $x = -0.54$ and $x = 1.54$ respectively. The particle traverses the lattice in positive direction and the orbit in the PSS jumps back and forth between the two islands. In the vicinity of the hyperbolic fixed points there is an infinite number of homo- and heteroclinic intersections of the stable and unstable manifolds, which yields horseshoe type dynamics and hence the presence of chaos [5]. For

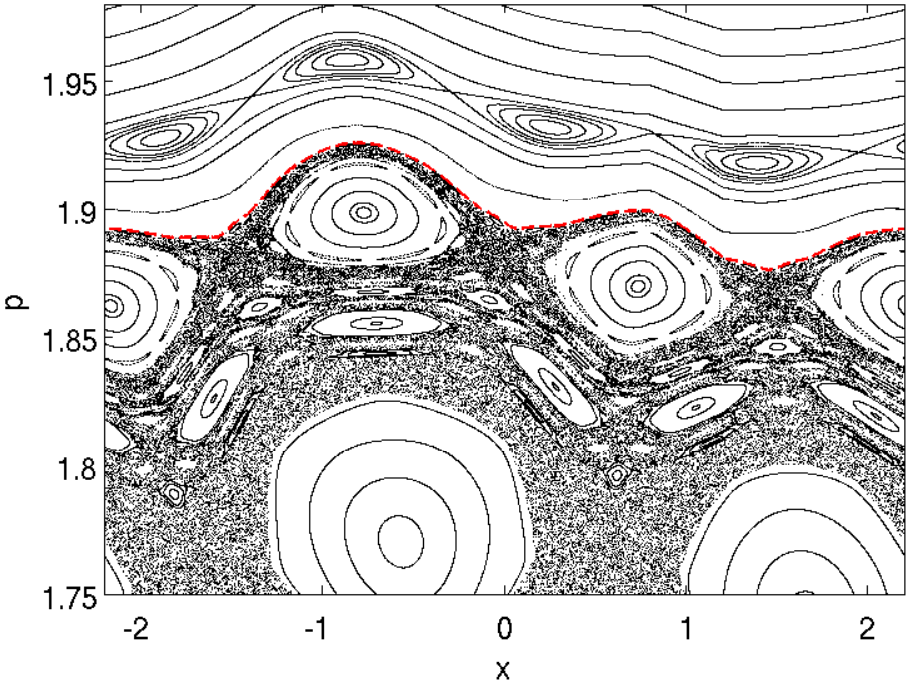

Figure 3.3: Magnification of the Poincaré surface of section shown in Fig. 3.1(b) in the region of the upper boundary of the chaotic sea with the FISC highlighted a red dashed line.

large kinetic energies these chaotic layers are too small to be visible in the PSS shown in Fig. 3.1 (b). The magnification of the PSS (see Fig. 3.3) for $1.75 < p < 1.95$ shows such a separatrix region around $p \approx 1.93$. However, with decreasing momentum the strength of the perturbation and thereby the size of these layers increases until finally a large chaotic sea in the PSS for small momenta develops. Trajectories belonging to orbits in this chaotic sea of the PSS wander diffusively through the lattice. The typical dynamics such a particle obeys in real space is shown in Fig. 3.2 (black line). The trajectory exhibits intermittent dynamics, i.e. we observe alternately phases during which the particle crosses the lattice only in one direction with constant velocity and phases of chaotic motion where the sign of the velocity is constantly reversed. The question of the origin of this intermittency is addressed at a later point. We will see that the phases during which the particles move with constant velocity leave an important hallmark in the diffusion properties of the system. At $x \approx 0.05$, $p = 0$ we see in Fig. 3.1 (b) the regular island embedded in the chaotic sea corresponding to trapped motion in the scattering region of a single barrier whose properties have been summarized in Sec. 2.3 (see also Ref. [70]). Other dominant elliptic islands in the PSS are the ones with winding number $w = r$, where the central periodic orbits are trajectories which travel r lattice sites during one oscillation period of the lattice, e.g. the $w = 1$ island at $x \approx -1.1$, $p \approx 0.7$ or $w = 2$ at $x \approx -0.1$, $p \approx 1.4$. In Appendix A a method is presented with which we can determine the position of these elliptic islands in the Poincaré surface of section.

Let us now return to the border regions of the PSS ($1.75 < p < 2.0$ in Fig. 3.1 (b)), where the large chaotic sea is bounded by tori, which have not been destroyed by the driving. In this regime of intermediate kinetic energy the PSS possesses a very rich structure with a hierarchy

of elliptic islands surrounded by smaller islands. For even larger momenta the chaotic sea is bounded by an invariant curve, which is called the "first invariant spanning curve" (FISC). Fig. 3.3 shows a magnification of this region of the PSS for positive momenta with the FISC highlighted as a red dashed line. For negative momenta there exists of course a FISC, too (Fig. 3.1 (b)). Independent of the phase of the driving when the PSS is done the FISC in the positive and negative momentum regime is found at $|p| \approx 1.9$. Although the position of the FISC in the PSS is very hard to determine analytically, it is possible to derive at least a lower bound to its position in velocity space, as will be shown in Sec. 3.3.

Finally, we want to discuss the PSS for the harmonically, uniformly driven lattice which is obtained by recording the time and the momentum of particles at equidistantly spaced positions in real space (see Sec. 3.2.1). In Fig. 3.1 (c) we show the corresponding PSS which is taken at the centers between the equilibrium positions of adjacent barriers. Consequently, every time a trajectory crosses the positions $x = \left(i + \frac{1}{2}\right) L$ the time t (phase of the driving law) and the momentum p is recorded. Evidently, the PSS is not mirror symmetric with respect to $p = 0$ but possesses a point symmetry to $\xi = \pi$, $p = 0$. The appearance of the PSS, e.g. the location of the elliptic islands in the PSS, depends on the position x where the PSS is taken. Qualitatively, the PSSs shown in Figs. 3.1(b) and (c) possess the same structure. We see a large chaotic sea with embedded elliptic islands and for larger momenta the phase space structure becomes more and more regular. Furthermore, the FISCs bounding the chaotic sea are in the same momentum regime both in Fig. 3.1 (b) and (c), too.

However, there are some clear differences. The island at $p = 0$ corresponding to trapped dynamics is not visible in Fig. 3.1 (c), because we perform the PSS outside the scattering region of the barriers. Still, this is not a drawback because we will use the "momentum versus phase" PSS afterwards only for setups where this island is absent. Generally, the number of islands embedded in the chaotic sea does not agree in Fig. 3.1 (b) and (c). For example there is a single island in Fig. 3.1(b) at $x \approx -0.1$, $p \approx 1.4$ which corresponds to two islands in Fig. 3.1(c) at $\xi \approx 1.6$, $p \approx 1.4$ and $\xi \approx 4.7$, $p \approx 1.4$ which is due to the different schemes used for performing the two PSSs. Using this special island as an example, we can understand intuitively the reason for the inequality of the number of islands. Its associated central periodic orbit belongs to a trajectory in real space which travels in one period of the driving two times the equilibrium distance of adjacent barriers, i.e. $x(t + T) = x(t) + 2L$ and $t(x + 2L) = t(x) + T$. Due to Eq. (3.4) this corresponds to a period one orbit in the stroboscopic PSS (Fig. 3.1 (b)). At the same time it is obvious that $t(x + L) \neq t(x + 2L)$ such that, according to Eq. (3.6), this trajectory yields a period two orbit in Fig. 3.1(c). For the other lattices we discuss exclusively the stroboscopic PSS because this is sufficient to demonstrate the impact of breaking the symmetries (2.4) and (2.21) of the Hamiltonian. The concept of "momentum versus phase" PSS, introduced here, will prove useful at a later point.

3.2.3 Constant phase gradient

In Fig. 3.4 (a)-(c) the PSS of the monochromatically driven lattice with a linear, equidistant phase gradient of period 3, 6 and 10 is shown. Clearly, the length of PSS increases with the phase period n because the length of the Hamiltonian's unit cell depends linearly on n (see Sec. 3.2.1). Contrary to the case $n = 1$, the PSS is obviously not symmetric with respect to $p = 0$ and moreover there is no alternative phase of a chosen PSS for which this symmetry

is restored. As a result not only the PSS but the complete phase space of these phase periods is asymmetric with respect to $p = 0$. Later we will see that this desymmetrization is actually the origin of the occurrence of directed currents in the system. Nevertheless, the PSS shows in general the same structure, which we have already discussed for the lattice of monochromatically, uniformly oscillating barriers. For small momenta there is a large chaotic sea with embedded elliptic islands. Since the potential height V_0 and the potential width l are equal for all phase periods, each barrier possesses analogous to $n = 1$ at $p = 0$ a small island of bounded motion in its scattering region [70] (e.g. $x_1 \approx 0.05$, $x_2 \approx 4.35$, $x_3 \approx 8.75$ for $n = 3$ in Fig. 3.4 (a)). With increasing kinetic energy more chains of elliptic islands appear until the chaotic sea is bounded by the FISCs. Although the form of the FISC depends on the phase at which the PSS is taken, Fig. 3.4 shows that for all periods of the gradient it is located at approximately in the same momentum range $|p| \approx 1.9$ similar to the case of the uniformly oscillating lattice (see Fig. 3.3 (b)). However, a significant symmetry the phase space possesses for $n = 1$ has disappeared, namely the areas of the elliptic islands in the PSS with winding numbers $w = r/s$ and $w = -r/s$ are in general not equal anymore. For example, in the case $n = 3$ the two dominant elliptic islands for positive momenta in the PSS belong to the periodic orbit with winding number $w = 1/2$ ($p \approx 1$, $x_1 \approx -1.65$, $x_2 \approx 4.95$ in Fig. 3.4 (a)). On the contrary, there are three periodic orbits with $w = -1/2$. Correspondingly, we find six small elliptic islands in the PSS for negative momenta ($p \approx -1$, $x_1 \approx -1.65$, $x_2 \approx 0.6$, $x_3 \approx 2.8$, $x_4 \approx 4.9$, $x_5 \approx 7.1$, $x_6 \approx 9.35$ in Fig. 3.4 (a)). Their total area in the PSS is less than the area of the two elliptic islands with $w = \frac{1}{2}$. Since these areas are preserved under the Hamiltonian flow, this is universally valid for all phases of the PSS.

3.2.4 Perturbed phase gradient

As the next step, the equidistance of the phase gradient with period 3 is broken up by imposing an additional phase shift α to the "middle" barrier. For a relatively large range of α one observes that the PSS remains on a coarse scale unaffected by this perturbation in the sense that the position and the size of the significant elliptic islands stays approximately the same. However, close to the FISC important changes occur. To see this, the upper part of the chaotic sea is magnified in Fig. 3.5 for $\alpha = 0$ (a) and $\alpha = -\frac{0.03\pi}{3}$ (b). We observe that the former stable FISC in the lattice with the equidistant gradient dissolves when decreasing α from 0 to $-0.03\pi/3$. Thereby, the proportion of the chaotic layer is increased considerably. However, at the position where the FISC is for $\alpha = 0$ in Fig. 3.5 (a) a cantorus remains in the PSS for $\alpha = -0.03\pi/3$. A cantorus is a remnant of a destroyed KAM-torus [5]. Depending on the irrationality of the winding number belonging to the dissolved torus, the cantorus can represent a strong barrier, such that the Hamiltonian flow passes through it very slowly. As a consequence it takes long until a trajectory, which has been started with small momentum in the chaotic sea, samples the accessible region of phase space above the cantorus. Consequently, for a finite time this cantorus acts in a similar way like the FISC, i.e. as if it would be an impenetrable torus. Yet, in the limit of long simulation time the Hamiltonian flow is able to pass through. Therefore these cantori are usually called "partial barriers" and possess a major impact on the transient dynamics and the long-term transport. Thus, corresponding care must be taken when estimating the transport velocity by simulating an ensemble of particles with small initial momenta in the chaotic sea.

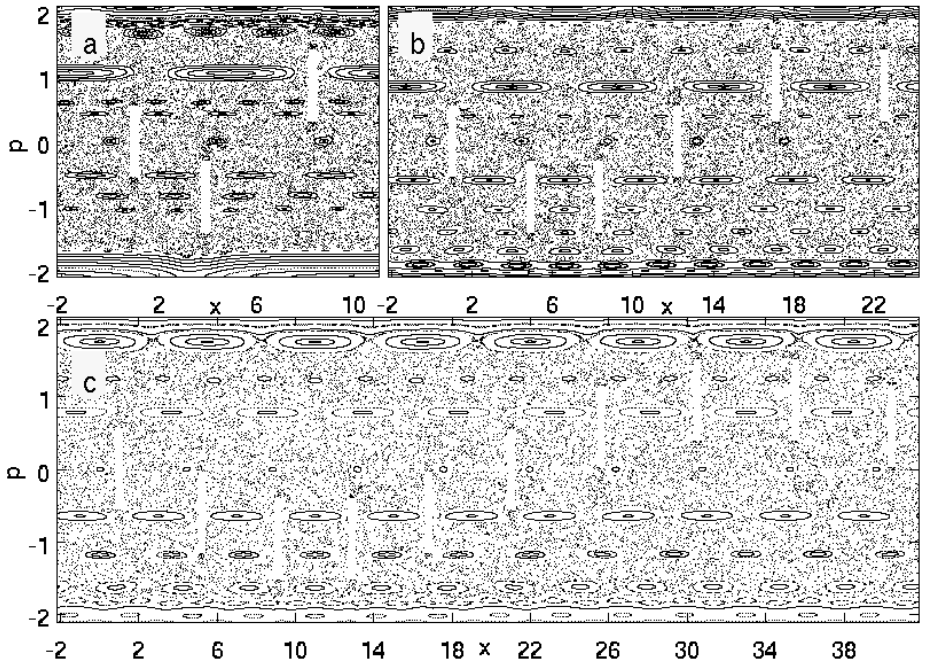

Figure 3.4: Stroboscopic PSS of the monochromatically driven lattice with a linear phase gradient of period $n = 3$ (a), 6 (b) and 10 (c). The length of the unit cell increases with the period of the gradient.

3.2.5 Broken phase gradient

Let us now consider the impact of a variation of the global potential height V_0 on the phase space properties for a lattice with a specific sequence of phase shifts having the period three $\{\ldots, 0, \frac{\pi}{10}, \frac{3\pi}{10}, 0, \frac{\pi}{10}, \ldots\}$. In Fig. 3.6 the PSS for four different values of V_0 is shown. The island at $p = 0$, which is a property of scattering from a single barrier and corresponds to a localized dynamics, has disappeared, because the parameters (V_0, l) are chosen such that its central periodic orbit has ceased to exist [70]. Still, for not too high values of the potential height $V_0 \leq 13.0$ the chaotic sea corresponding to diffusive dynamics in real space is connected (see Fig. 3.6 (a)). With increasing V_0 another class of localized dynamics arises in the system. As Fig. 3.6 (b) shows, a separated chaotic sea between the first and the second barrier appears. This part of phase space is confined by impenetrable tori, i.e. the particles starting in this sea cannot escape from it and are thus trapped between the barriers. In Fig. 3.7 (a) a trajectory in real space of such a trapped orbit in the PSS obeying chaotic dynamics is shown. Note that the "empty barrier" region in the PSS is not a confinement criterion like the invariant tori. As the potential height is increased further localized chaotic trajectories appear between the other barriers, too. Embedded in these chaotic seas are elliptic islands belonging to regular, trapped dynamics of particles between two adjacent barriers, e.g. at $x = 6.9$, $p = 3.2$ in Fig. 3.6 (c) with a corresponding trajectory in real space shown in Fig. 3.7 (b). Intuitively, the occurrence of these localized chaotic seas is surprising, because one might expect that with increasing potential height the particles just have to acquire more collisions until they are finally fast enough to surpass V_0. Even more astonishing is the fact that these regions in phase space do not appear simultaneously between all barriers but successively

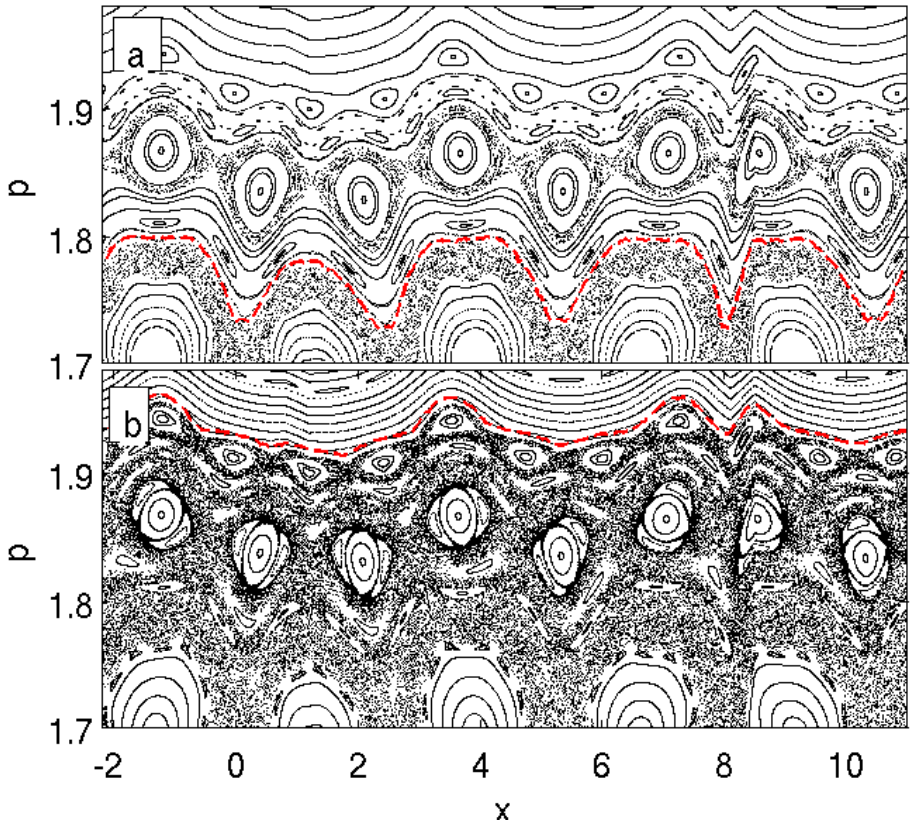

Figure 3.5: Magnification of the Poincaré surface of section in the upper region of the FISC for two different phase gradients. (a) is the equidistant gradient of period 3 and in (b) the phase of the "middle" barrier has been shifted by $\alpha = -0.03\pi/3$. The red dashed curves are the FISCs.

with increasing V_0.

This behavior can be resolved straightforwardly. For small momenta $p^2/2 \ll V_0$ the particles exhibit exclusively reflective collisions, i.e. they cannot penetrate into the barriers. In this regime the dynamics of the Hamiltonian (2.1) is equivalent to a variant of the well-known Fermi-Ulam-Model (FUM) [5] with two oscillating walls. The original FUM describes the dynamics of a particle bouncing between two infinitely heavy walls where one wall is static and the other oscillates. In the case of smooth driving laws the phase space of the FUM is not globally stochastic, but possesses a FISC at momentum p_b, which prevents particles from gaining arbitrarily high momenta [5]. In our case both walls oscillate which only matters in that the momentum p_b of the FISC gets shifted compared to the original FUM. Consequently, localized chaos in the driven lattice will occur if the potential height is larger than the kinetic energy associated with this momentum, $V_0 \geq p_b^2/2$.

For momenta less than a certain value p_s the phase space of the FUM is indeed completely chaotic. In the case of the previous setups (Figs. 3.1 and 3.4 with $V_0 = 0.16$) the potential height V_0 has been chosen smaller than the corresponding kinetic energy $V_0 \leq p_s^2/2$. Consequently, all orbits of the large chaotic sea move diffusively through the lattice in these cases. For intermediate momenta $|p_s| < |p_r| < |p_b|$ the phase space of the FUM possesses a well known resonance structure [5], whose central periodic orbits correspond to periodic

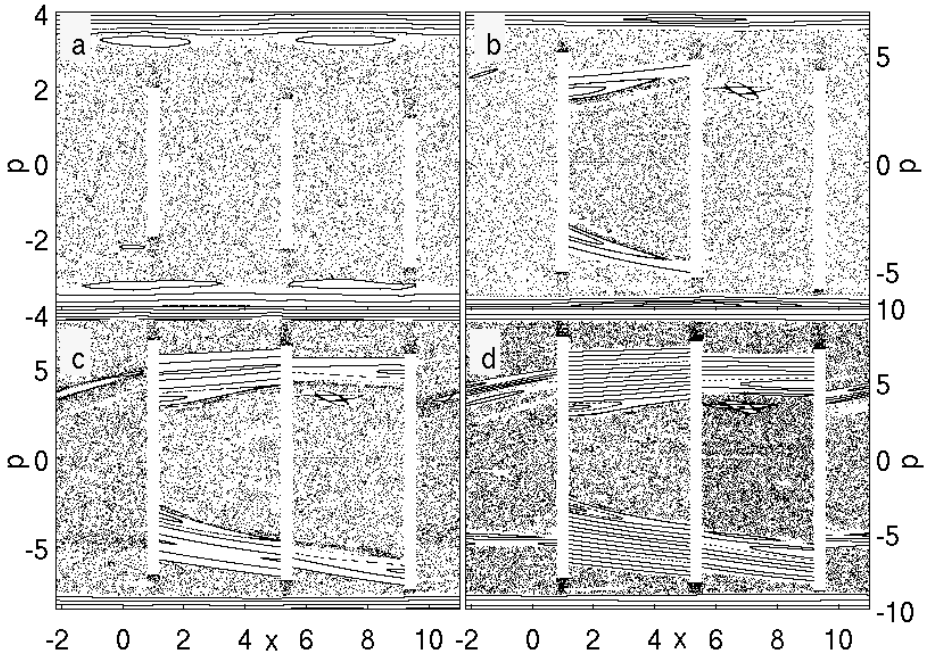

Figure 3.6: PSS for a lattice with a specific phase gradient of period three $\{\ldots, 0, \frac{\pi}{10}, \frac{3\pi}{10}, 0, \frac{\pi}{10}, \frac{3\pi}{10}, \ldots\}$ and four different global potential heights. The values are $V_0 = 2.0$ (a), $V_0 = 13.0$ (b), $V_0 = 22.0$ (c) and $V_0 = 32.0$ (d).

trajectories bouncing between the adjacent barriers and colliding with them only at certain phases (see Fig. 3.7 (b)). When the global potential height is increased, these orbits and their surrounding elliptic islands appear in the PSS between two barriers prior to the blocking tori, since $|p_r| < |p_b|$. Due to the fact that the equations of motion are invariant under a constant shift in time, the phase space of the variant of FUM with two oscillating walls depends only on the relative phase between the walls but not on an absolute phase shift. Naturally, the same holds for the momentum p_b of the FISC, which limits the kinetic energy growth of chaotic particles. Due to the different phase relations $\Delta\varphi = \varphi_{i+1} - \varphi_i$ two adjacent barriers have with respect to each other, these confined chaotic seas do not occur simultaneously between different pairs of barriers but one after another with increasing potential height (see Fig. 3.5 (b)-(d)). For the previous discussed lattices with constant phase gradients of periods $n = 1$, 3, 6, 10 neighboring barriers have the same relative phase $\Delta\varphi = 0, \frac{2\pi}{3}, \frac{2\pi}{6}, \frac{2\pi}{10}$. Consequently, in these setups the confined chaotic seas will occur simultaneously between all barriers, if the potential height V_0 is increased. Performing Poincaré surfaces of section for different V_0 with phase period $n = 1, 3$ etc. reveals that this is indeed true. Finally, we remark that even for large potential heights $V_0 = 32$ the lattice with broken phase gradient possesses a chaotic sea corresponding to diffusive dynamics of particles. In the PSS (Fig. 3.6 (d)) the chaotic layers above and below the blocking tori leading to trapped particles between neighboring barriers ($5 \leq |p| \leq 10$ in Fig. 3.6 (d)) belong to one chaotic sea. Consequently, an orbit launched in the upper or in the lower layer jumps up and down in PSS and the trajectory in real space moves diffusively.

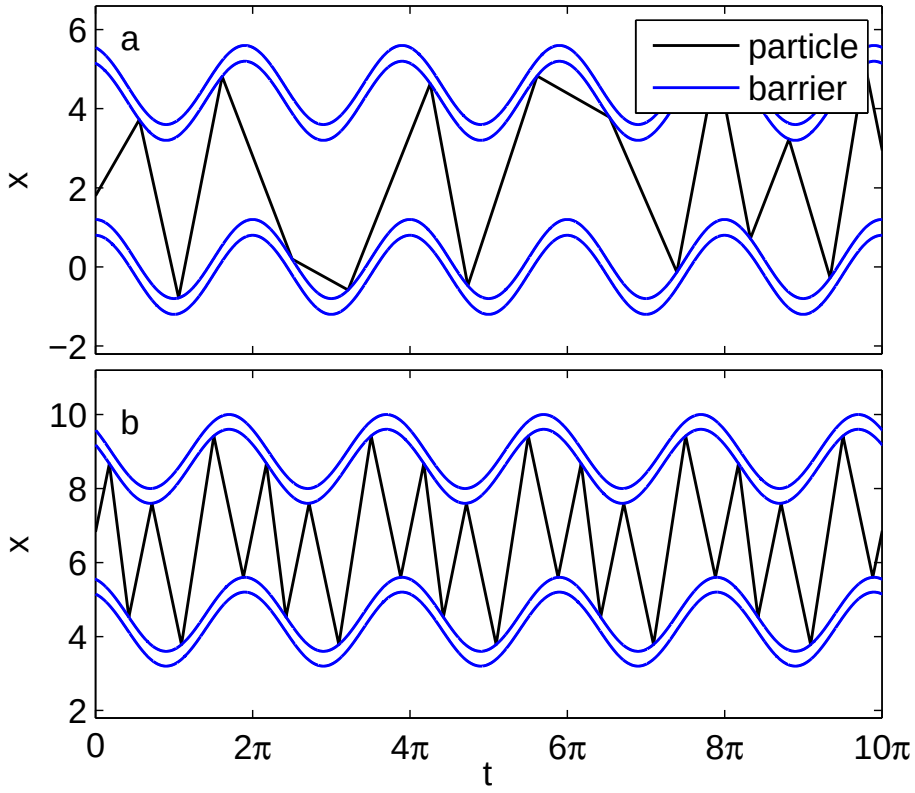

Figure 3.7: (a) Trajectory started in the localized chaotic sea between the first and the second potential barrier for the lattice with a specific phase gradient of period three $\{\ldots, 0, \frac{\pi}{10}, \frac{3\pi}{10}, 0, \frac{\pi}{10}, \frac{3\pi}{10}, \ldots\}$ and potential height $V_0 = 13.0$ (Fig. 3.6 (b)). (b) Periodic orbit bouncing between the second and the third barrier in the unit cell. The corresponding initial condition belongs to the elliptic island embedded in the chaotic sea at $x \approx 6.8$, $p \approx 3.3$ (Fig. 3.6 (b)).

3.2.6 Biharmonically, uniformly driven lattice

In this section the phase space of the biharmonically, uniformly driven lattice is discussed. In Fig. 3.8 we show the associated Poincaré surface of section for $V_0 = 0.16$ and $l = 0.4$. It possesses a similar topology like the PSSs belonging to the previous setups, i.e. we can identify the typical various components. For large momenta the PSS is foliated by deformed invariant curves of the unperturbed system. With decreasing momentum the structure becomes richer until we reach the large chaotic sea corresponding to diffusive dynamics of trajectories in real space with embedded ballistic, elliptic islands. As we see, there is no regular structure belonging to trapped particles in the scattering region of a single barrier, although for the present choice of the potential height and the barrier length such an elliptic island exists for the purely cosine oscillation. In the case of the biharmonic driving law this island arises for shallower potential heights and its volume in phase space is smaller.

Still, we observe also major differences to the previous setups. Evidently, the desymmetrization of the PSS and thus of the complete phase space is stronger than before. Firstly, we see that there is for example at $x \approx -1.1$, $p \approx 0.7$ an elliptic islands in the PSS (see Fig. 3.8) to which no analogue island for negative momenta is visible. Furthermore, a closer look at

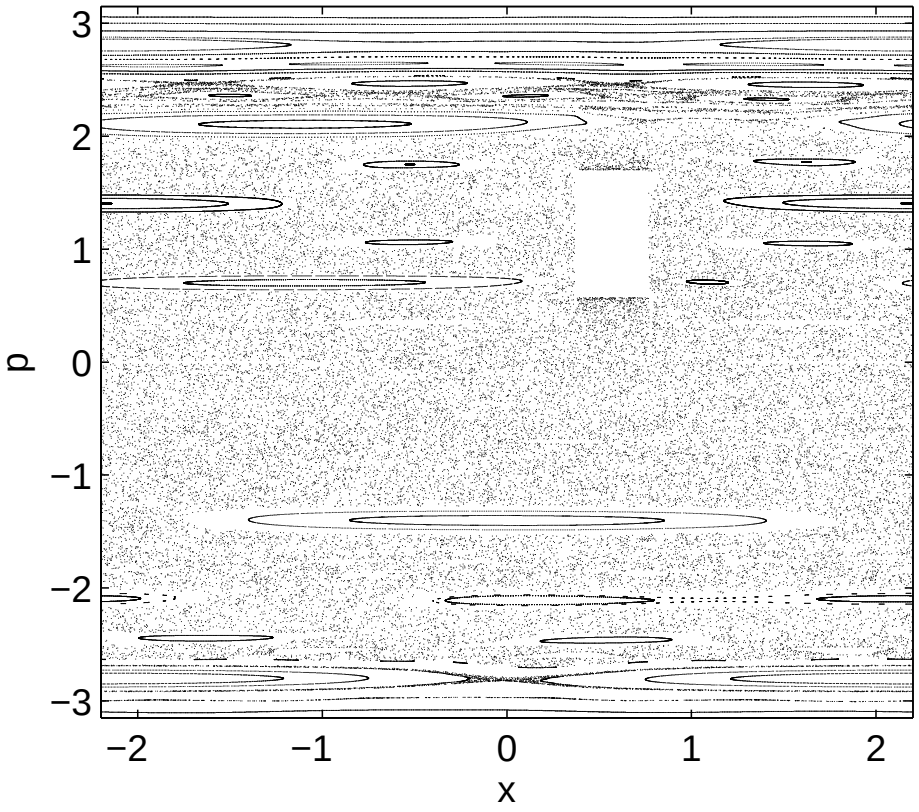

Figure 3.8: Stroboscopic PSS of the biharmonically, uniformly driven lattice for $V_0 = 0.16$, $l = 0.4$ and $L = 4.4$.

the PSS reveals that the large chaotic sea belonging to diffusive dynamics of trajectories is bounded asymmetrically, that is the average momentum of the FISC for $p < 0$ is larger than for $p > 0$. Accordingly, we expect for the biharmonic driving law a larger directed current of particles. In the following section we show how this can be traced back to the different maximal velocities of the barrier in positive and negative direction, respectively.

3.3 First invariant spanning curve

In this section we show how an approximation for the position of the FISC in velocity space can be derived from simple kinematic considerations. In Fig. 3.9 (a) we show the collision points for a particle started on the outermost torus of the $w = 1$ island. The collisions occur for certain phases when the barrier moves in the opposite direction such that the relative kinetic energy is high enough to surpass the potential height. On the contrary, particles on the FISC are fast enough to be transmitted, even if a collision takes place when the barrier moves with its extremal velocity u_{ex} in the same direction (see Fig. 3.9 (b)), i.e. the minimal relative kinetic energy must exceed the potential height. Thus we get

$$\frac{m\,(v - u_{ex})^2}{2} \geq V_0, \tag{3.9}$$

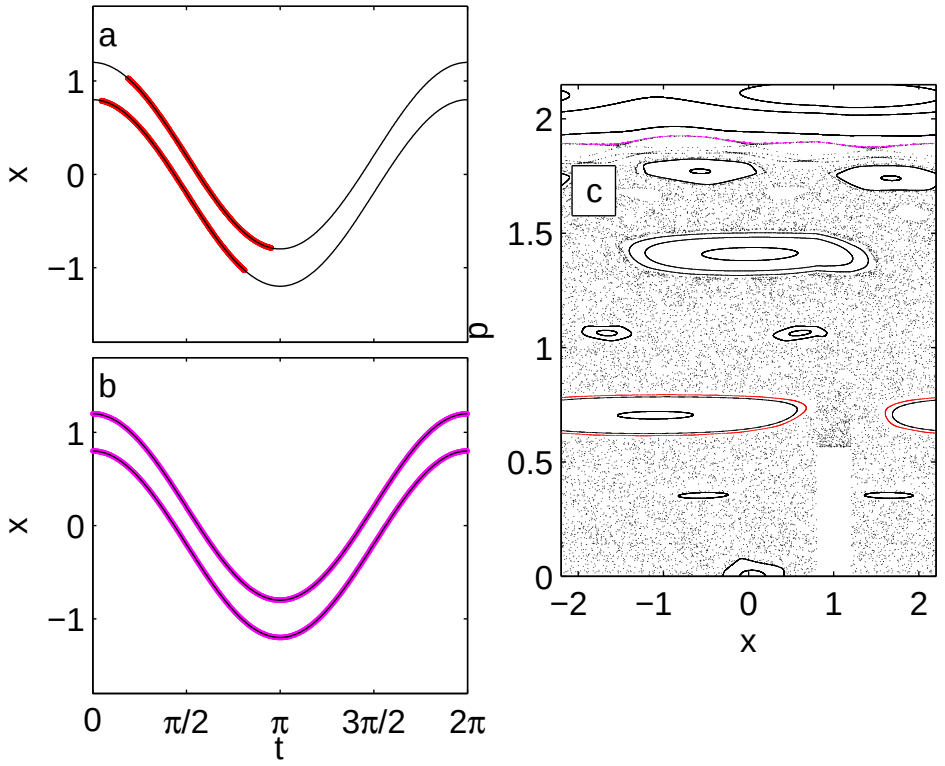

Figure 3.9: (a) Movement of the barrier during one phase of oscillation together with all collision points (red part) of a particle started on the outermost torus of the elliptic island belonging to the winding number $w = 1$ (see Fig. (c)). (b) depicts the same information as in Fig. (a) but for a particle started on the FISC (see Fig. (c)). (c) shows an extract of the PSS corresponding to the uniformly driven lattice together with the orbits whose collision points with the barriers are plotted in (a), (b).

where v is the velocity of the particle. In case of a harmonic driving law, the extremal velocities of the barrier are given by $u_{ex} = \pm\omega C$. Plugging u_{ex} in Eq. (3.9) yields an approximation to the velocity regime where the FISC is located in the PSS. Depending on the sign of v we find

$$v_{\pm} = \pm\omega C \pm \sqrt{\frac{2}{m}V_0}, \tag{3.10}$$

where the index $\pm$ denotes the position of the FISC in the PSS for positive and negative velocities, respectively. In case of the harmonic driving law we have $|v_+| = |v_-|$ independent of the phase period. For $m = 1$, $\omega = 1$, $C = 1$ and $V_0 = 0.16$, we find from Eq. (3.9) $|v_{\pm}| \approx 1.57$. Fig. 3.1 (b) shows that the FISC of the uniformly oscillating lattice is located indeed at $|p| \approx 1.9 > m|v_{\pm}|$. The significant discrepancy (around 15 %) is due to the fact that the approximation accounts only for a simple kinematic consideration of the dynamics between the particle and a single barrier, neglecting all the dynamical processes happening in the extended system. Yet, with decreasing barrier width l the agreement becomes better and in the limit $l \to 0$ the position of the FISC in velocity space predicted by formula (3.9) is exact.

We can understand this behavior straightforwardly. For a particle with initial velocity v

which is transmitted through the barrier after two collisions (one with the left and one with the right barrier's edge) the change of velocity is given by

$$\Delta v = v_b(\xi_2) + \sqrt{\left(v_b(\xi_1) - v_b(\xi_2) + \sqrt{(v - v_b(\xi_1)^2 - \frac{2V_0}{m}}\right)^2 + \frac{2V_0}{m}} - v, \tag{3.11}$$

where ξ_1 and ξ_2 are the phases of the collisions. For $l \to 0$ we have obviously $v_b(\xi_1) = v_b(\xi_2)$ and thus $\Delta v = 0$. Accordingly, a particle which is faster than the maximal barrier velocity is never decelerated independent of the collision phase and continues to traverse the lattice in one direction. However, with increasing potential width l a particle can be decelerated after it has been transmitted because the barrier velocity at the first and the second collision are not equal anymore, i.e. $v_b(\xi_1) \neq v_b(\xi_2)$, and thus $\Delta v \neq 0$ in general. Consequently, it can happen that after the transmission of a particle with initial velocity $|v| > |v_\pm|$ through a barrier it is too slow to surpass the next one, e.g. if this collision occurs again at a phase when the relative kinetic energy is minimal. Therefore, a finite barrier width l yields a correction, i.e. a particle on the FISC must be faster because Eq. (3.9) underestimates its velocity. In fact, we have observed for all driving laws and phase periods that the chaotic sea in the PSS grows in the momentum-dimension with increasing l because the FISC gets shifted to higher velocities. Unfortunately, this correction is hard to quantify. Nevertheless, this naive approach provides some insights, as we shall argue briefly in the following.

For driving laws with more than one frequency the extremal velocity u_{ex} of the barrier depends on its sign. For example, in the case of the biharmonic driving law $f(t) = C(\cos(\omega t) + \sin(2\omega t))$ we find $u_{ex,+} \approx 2.06\omega C$ and $u_{ex,-} = -3\omega C$, respectively. In this case Eq. (3.9) yields $v_+ = 2.06\omega C + \sqrt{2V_0/m}$ and $v_- = -3\omega C - \sqrt{2V_0/m}$. Consequently, we expect that the FISC for positive momenta is located closer to $p = 0$ than for negative momenta independent of the phase of the PSS. Indeed, the PSS of the biharmonically, uniformly oscillating lattice shown in Fig. 3.8 reveals such a behavior. In fact, due to this strong asymmetry of the FISC we observe immediately that the area of the chaotic sea with $p < 0$ is larger than the area with $p > 0$ for all phases of the PSS. For the setups with monochromatic driving and a phase gradient it is not so simple to decide whether the chaotic sea possesses a positive, negative or no asymmetry only by looking at the PSS. Instead, in these cases we have to evaluate the areas explicitly.

3.4 Intermittency

In this section we return to the problem posed in Sec. 3.2.2 concerning the origin of the intermittent behavior of particles launched in the chaotic sea of the PSS, i.e. diffusive phases interrupted by ballistic flights. Fig. 3.10 (a) shows a trajectory obeying such characteristic dynamics in the monochromatically, uniformly oscillating lattice. As we see, the particle moves diffusively through the system. Yet, for some time intervals it traverses many barriers only in one direction as if it would be in a ballistic island or in a region of the PSS above the FISC, i.e. a phase spanning torus. A magnification of the trajectory shown in Fig. 3.10(a) reveals that the intermittent behavior of the dynamics continues on smaller scales, too.

In order to throw light on the origin of this behavior we show in Fig. 3.10 (b) the complete PSS of the monochromatically, uniformly oscillating lattice together with the surfaces of

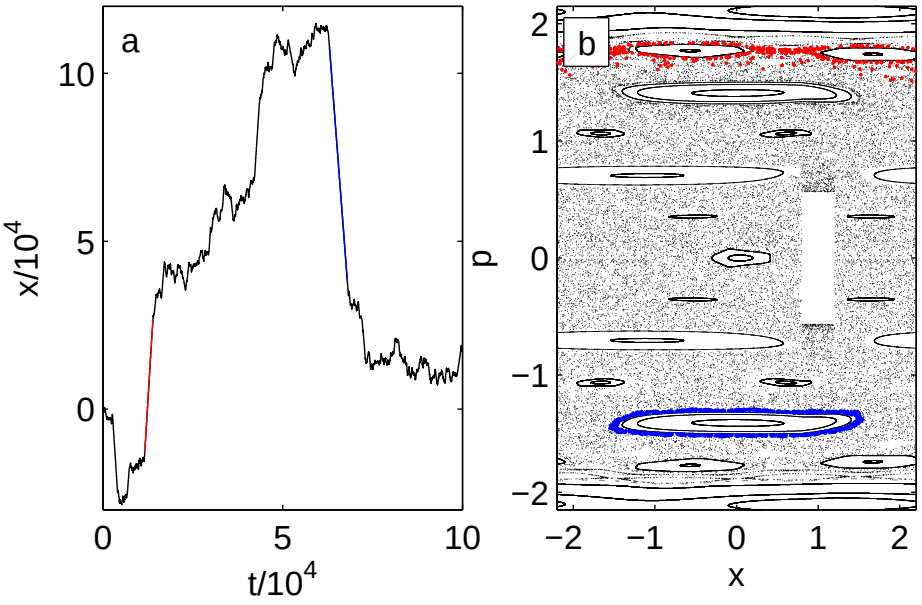

Figure 3.10: (a) Trajectory obeying chaotic dynamics (initial condition $x(0) = -2.2$, $p(0) = 0.3$) in the lattice of uniformly oscillating barriers $V_0 = 0.16$, $l = 0.4$. (b) Red and blue points in the stroboscopic PSS are the phases of the orbit corresponding to the trajectory shown in (a) during which it performs the ballistic flight in positive and negative direction, respectively.

section during which the particle performs a long flight in positive and negative direction (red and blue points in Fig. 3.10(b) respectively). In case of the long flight in negative direction $6.3 \cdot 10^4 \leq t \leq 6.8 \cdot 10^4$ the orbit in the PSS traces the outermost torus of the elliptic island with winding number $w = -2$ (blue points in Fig. 3.10 (b)). For the long flight in positive direction, i.e. $1.16 \cdot 10^4 \leq t \leq 1.39 \cdot 10^4$, the orbit is confined in the PSS to the region of the chaotic sea close to the FISC (red points in Fig. 3.10 (b)). In the literature the effect of chaotic trajectories coming arbitrary close to an invariant structure in phase space and remaining in its vicinity for a certain time is known as "stickiness" [73, 74]. It is a phenomenon which typically occurs in Hamiltonian systems with mixed phase space. Stickiness leads to sporadic episodes of almost regular dynamics which leaves its hallmark in e.g. the decay of correlations [73, 74] or the recurrence time [77]. In our lattice the chaotic orbits in the PSS which become sticky to elliptic islands lead to ballistic flights with different velocity depending on the winding number. Furthermore, stickiness can yield phases of motion during which the particles remain in the scattering region of one barrier. The latter occurs when an orbit gets sticky to the island at $p = 0$ corresponding to trapped dynamics in the scattering region of a single barrier (see Sec. 2.3).

Another origin of ballistic flights in the lattice are the so-called "cantori" in phase space, which are remnants of dissolved tori with irrational winding number. One can think cantori as tori with gaps through which the Hamiltonian flow and thus chaotic trajectories can leak. Depending on the number-theoretic properties of the winding number of the dissolved torus the flux across a cantorus can become arbitrarily small. Due to their property of forming a strong resistance to the Hamiltonian flow, cantori are sometimes also called "partial barriers" in the literature. A chaotic orbit which is confined by a partial barrier to a sub-domain

of the complete PSS with non-zero average momentum yields also a ballistic flight of the trajectory in real space. In Appendix B we give an example of such a trajectory and show for the monochromatically, uniformly driven lattice how the flux across a cantorus can be determined numerically. In the next chapter we will see that these ballistic flights have a major impact on the diffusion properties of the lattice.

Chapter 4

Transport and localization of particles

In this chapter the transport and the localization of particles in a laterally oscillating lattice is studied. As we have seen in Sec. 2.4 the directed transport can be ruled out by means of symmetry considerations for the case of monochromatic and uniform driving, i.e. when all barriers oscillate harmonically without phase gradient. Yet, whether in the other setups a current of particles is observed cannot be judged prior to a more detailed analysis, because breaking the symmetries (Ref. [44]) is a necessary but not a sufficient condition for the occurrence of directed transport. In the course of this study the velocity of the directed current as a function of the phase gradient of the barriers and the diffusion properties in the lattices are discussed, too.

4.1 Transport and diffusion in phase-modulated lattices

In this section we discuss the transport and the diffusion properties for the setups defined in Sec. 3.1.

4.1.1 Transport properties for constant phase gradients

Let us start with the transport properties of the lattice with a constant phase gradient $\varphi_i = \frac{i}{n}2\pi$ with $n = 1, 3, 6, 10$. In order to decide whether directed transport occurs or not we study the evolution in time of the mean position $\langle x(t)\rangle$. Therein $\langle\cdots\rangle$ denotes the average of an ensemble of particles whose initial conditions are always chosen such that the particles start with small, symmetrically distributed momenta in the chaotic sea of the PSS close to the origin of the lattice, i.e. in the beginning the ensemble average of the velocity is zero. In this way we avoid that some particles are initialized already in relevant elliptic islands belonging to ballistic flights or to trapped dynamics. In Fig. 4.1 (a) the absolute value of the mean position $|\langle x(t)\rangle|$ as a function of time is shown for phase periods $n = 1, 3, 6, 10$. For $n = 1$ (lattice of monochromatically, uniformly oscillating barriers) the plot reveals that no directed transport occurs, as we have expected because in this case the relevant symmetries are not broken (see Sec. 2.4). The ensemble average of the position fluctuates only around $\langle x\rangle = 0$. In order to make this visible the data-points with $\langle x(t)\rangle < 0$ ($\langle x(t)\rangle > 0$) for $n = 1$ have been plotted with asterisks (diamonds). A similar behavior is observed for $\langle v(t)\rangle$ (Fig. 4.1 (b)). For $n = 1$ the mean velocity changes its sign several times correlated with the corresponding behavior of $\langle x(t)\rangle$. On the contrary, for other phase periods ($n = 3, 6, 10$) we clearly observe directed transport. After an initial transient $t \approx 10^3 - 10^4$, which corresponds to the time needed for the spreading of the initial ensemble over the whole chaotic sea in phase space, the mean position grows according to $\langle x(t)\rangle = v_{\mathrm{mean}}t$, where v_{mean} is referred to as the *transport velocity* of the system. An asymptotic linear fit to the curves $\langle x(t)\rangle$ yields

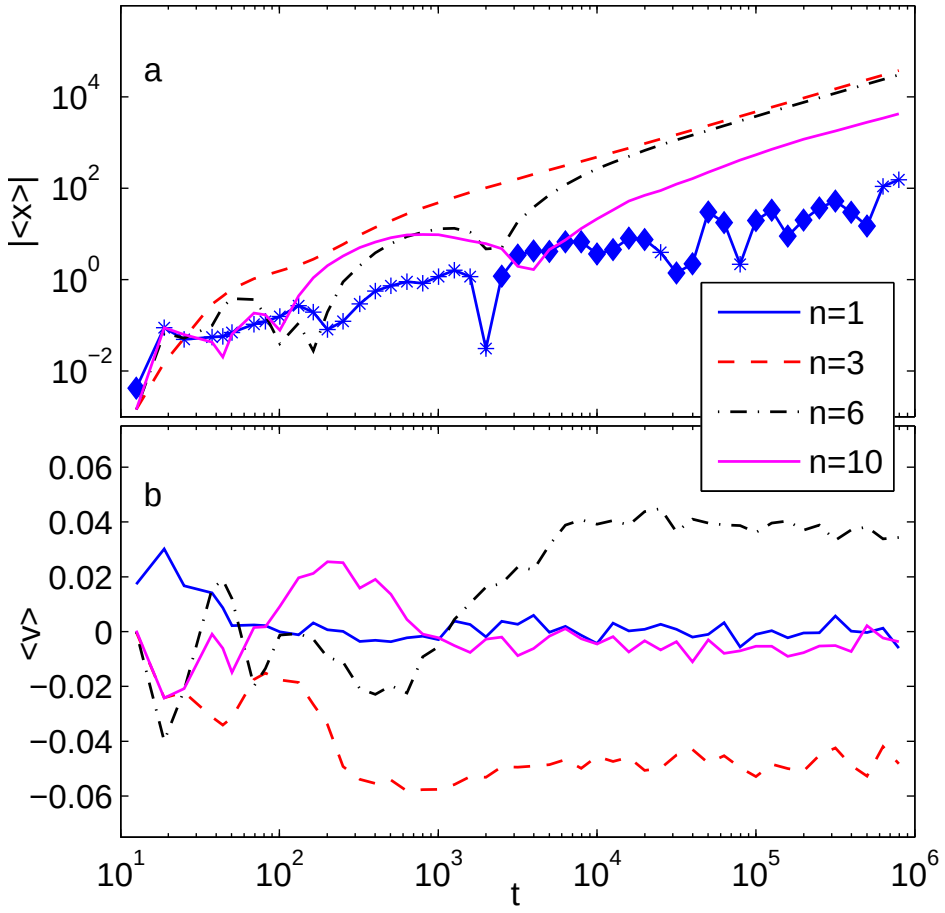

Figure 4.1: (a) Absolute value of the mean position averaged over an ensemble of 10^5 particles, which has been started with small momentum $p \leq 0.1$ in the chaotic sea as a function of time for various phase periods n. For $n = 1$ (blue line) the datapoints with $\langle x(t) \rangle < 0$ / $\langle x(t) \rangle > 0$ are additionally plotted as asterisks / diamonds. (b) The corresponding evolution of the mean velocity as a function of time.

phase period n	1	3	6	10
v_{mean}	0	-0.0476	0.0384	-0.0055
$v_{\mathcal{CS}}$	0	-0.0456	0.0372	0.0201

Table 4.1: Transport velocities for the different phase periods obtained by performing asymptotically a linear fit to the evolution of the ensemble average of the position $\langle x(t)\rangle = v_{\text{mean}} \cdot t$ (first row) and by averaging over the chaotic sea of phase space according to Eqs. (4.1) and (4.2)(second row).

the mean transport velocities presented in the first row of Table 4.1. For $n = 3$ and $n = 6$ the values for v_{mean} in Table 4.1 are consistent with the behavior of the ensemble average of the velocity $\langle v(t)\rangle$ for large times (Fig. 4.1 (b)). After the initial transient, $\langle v(t)\rangle$ never changes sign again and fluctuates around v_{mean}. Whether this is also true in the case of the phase period $n = 10$ cannot be judged ultimately, since the fluctuations of $\langle v(t)\rangle$ are of the same order of magnitude as v_{mean}. Nevertheless, Fig. 4.1 (a) reveals that after the transient $t \approx 10^4$ the ensemble average of the position grows linearly with time.

To get an intuition about the scales of the transport let us consider the following instructive example. In the case of phase period $n = 3$ we find that the ensemble average of the particle position $\langle x(t)\rangle$ equals after 10000 periods of the driving -680 times the equilibrium distance between two adjacent barriers, so the transport is rather small. For visualization we plot in Fig. 4.2 (a) the absolute value of $\langle x(t)\rangle$ together with the variance $\sigma_x(t) = \sqrt{\langle x(t)^2\rangle - \langle x(t)\rangle^2}$ and show in Figs. 4.2 (b)-(d) several snapshots of the probability density function $\rho(x)$ of the particles' position in real space. In the beginning, i.e. $t \leq 10^4$, we observe primarily a broadening of $\rho(x)$ (see Fig. 4.2 (b) and (c)) since in this regime the dynamics is dominated by the diffusion. The transport is visible only by a slight negative shift of the maximum of $\rho(x)$ (see Fig. 4.2 (c)). Subsequently, the directed transport gains importance compared to the diffusion and at $t \approx 10^6$ the curves $|\langle x(t)\rangle|$ and $\sigma_x(t)$ intersect. Indeed, we observe that the corresponding probability distribution $\rho(x)$ (Fig. 4.2 (d)) shows beside a permanent broadening also a clear drift of $\rho(x)$ in the negative direction. For even larger times $t = 10^8$ the average position exceeds the variance (see Fig. 4.2 (a)). Accordingly, the width of the associated probability distribution $\rho(x)$ (Fig. 4.2(e)) is much smaller than the position of its maximum. In order to optimize the transport one has thus to tune the parameters of the lattice (like the potential height V_0) such that the crossing of $\langle x(t)\rangle$ and $\sigma_x(t)$ occurs as soon as possible. In this way one would create a most effective ratchet. However, such a study is beyond the scope of this thesis.

Let us now discuss the question of the origin for the appearance of directed transport. Due to the choice of the initial conditions, the ensemble is localized in the chaotic sea between the FISCs for every point in time. Thus, the convergence of the ensemble average of the velocity $\langle v(t)\rangle$ to a non-zero value can be explained by means of an asymmetry of the chaotic sea with respect to $p = 0$, if it is assumed additionally that the dynamics is ergodic with a uniform invariant density [51]. Again, it is important to emphasize that this desymmetrization has to occur in phase space and not only for a certain PSS, which depends on the phase of driving at the moment of the snapshot. For a Hamiltonian system with mixed phase space the proof that the dynamics is ergodic in the chaotic subsets is still an open problem [78] and has been achieved only for very special systems [79]. Nevertheless, if we assume ergodicity of the dynamics in the chaotic sea, then the phase space average of the velocity $v_{\mathcal{CS}}$ over the chaotic

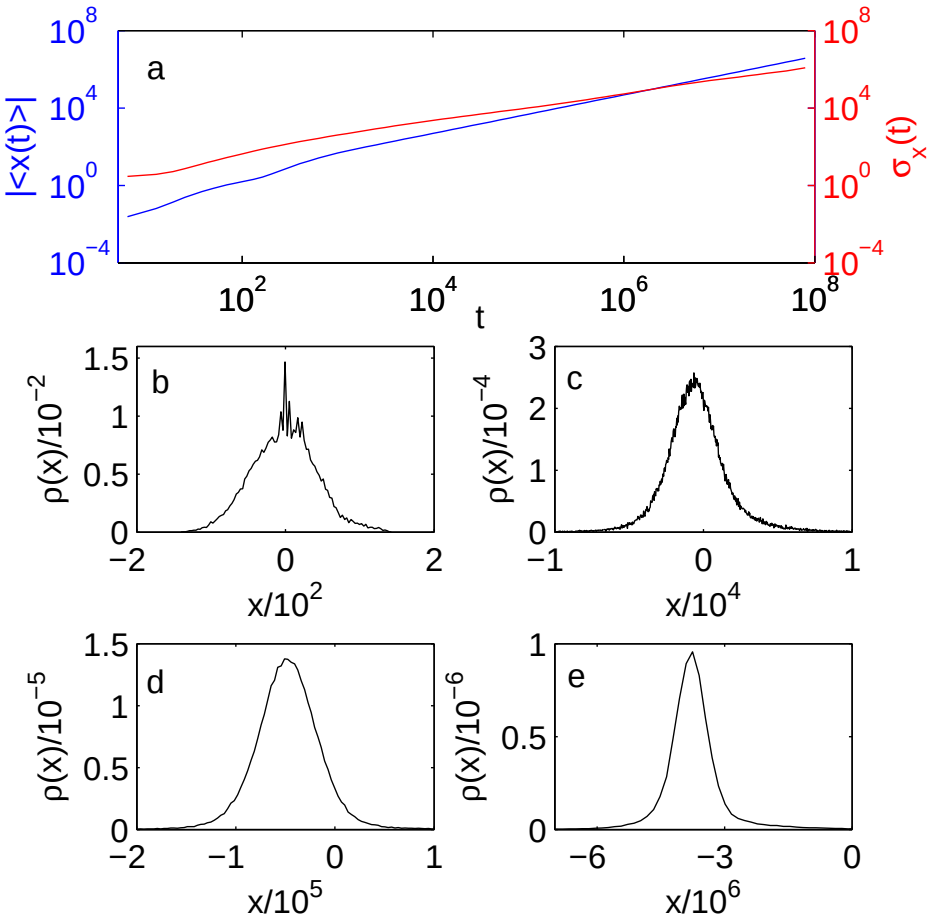

Figure 4.2: (a) Absolute value of the average particle position (blue curve) together with the variance (red curve) for an ensemble of 10^5 particles in the monochromatically driven lattice with phase period $n = 3$. Below, a sequence of the particle distribution in real space $\rho(x,t)$ is depicted for (b) $t = 10^2$, (c) $t = 10^4$, (d) $t = 10^6$ and (e) $t = 10^8$.

sea should coincide with v_{mean}. $v_{\mathcal{CS}}$ can be calculated by

$$v_{\mathcal{CS}} = \frac{1}{\Omega_{\mathcal{CS}}} \int\limits_{\mathcal{CS}} \frac{p}{m}\, dx\, dp\, dt, \tag{4.1}$$

where $\Omega_{\mathcal{CS}}$ is the phase space volume of the chaotic sea. Due to the time and the spatial-periodicity of the Hamiltonian $H(x, p, t+T) = H(x+L, p, t) = H(x, p, t)$, it is sufficient to perform the integration only over one period of the driving and along one unit cell. If we change in Eq. (4.1) from time t to the phase of the oscillation $\xi = \omega t \bmod 2\pi$, the volume $\Omega_{\mathcal{CS}}$ can be written as $\Omega_{\mathcal{CS}} = 2\pi \cdot A_{\mathcal{CS}}$ with $A_{\mathcal{CS}}$ being the area of the chaotic sea in the PSS. Performing the integration over x and p in Eq. (4.1) yields hence the mean velocity of the chaotic sea in the PSS for a fixed phase ξ which is determined by dividing the PSS into small rectangles and averaging over the cells that get visited by a single long ($t_{\text{final}} \geq 10^9$) chaotic trajectory. This procedure yields a function $v_{\mathcal{PSS}}(\xi)$ whose convergence is checked by enlarging the grid of the PSS. Finally, the mean velocity of the chaotic sea of the complete phase space is obtained by averaging over the phases of the PSS, i.e.

$$v_{\mathcal{CS}} = \frac{1}{2\pi} \int\limits_{0}^{2\pi} v_{\mathcal{PSS}}(\xi) d\xi. \tag{4.2}$$

Of course the present scheme for calculating $v_{\mathcal{CS}}$ is equivalent to the procedure presented in [46, 51]. We remark, that for our system it turns out to be more efficient to evaluate numerically the integrals (4.1), (4.2) according to the just introduced steps than applying the sum formula of [51], where all the winding numbers and areas of the significant elliptic resonances in the PSS have to be determined. For a toy-model with only one elliptic island which is used in [51] the sum formula needs of course few time and effort. However, for a more realistic Hamiltonian system with a mixed phase space like the present driven lattice where we have a hierarchy of islands surrounded by sub-islands calculating all the winding-numbers and areas is tedious and thus not feasible anymore. Furthermore, even for very long simulation times ($t \geq 10^9$) a "drift" of a chaotic trajectory beyond an intact KAM-torus by accumulating numerical errors has never been observed in our system.

In Fig. 4.3 we show for two phase periods the average velocity of the chaotic in the PSS $v_{\mathcal{PSS}}(\xi)$ as a function of the phase ξ when the surface of section is taken. Apparently, for $n = 1$ (see Fig. 4.3(a)) the function $v_{\mathcal{PSS}}(\xi)$ is zero at $\xi = 0, \pi, 2\pi$ when the PSS possesses mirror-symmetry with respect to $p = 0$. Furthermore, Fig. 4.3 (a) reveals the point-symmetry of the function $v_{\mathcal{PSS}}(\xi)$ to $\xi = \pi$ for $n = 1$, i.e. $v_{\mathcal{PSS}}(\pi+\xi) = -v_{\mathcal{PSS}}(\pi-\xi)$ so that averaging over one complete phase gives $v_{\mathcal{CS}} = 0$. Contrary, for $n = 3$ the average velocity in the PSS $v_{\mathcal{PSS}}(\xi)$ fluctuates around a negative value, i.e. in this case formula (4.2) yields $v_{\mathcal{CS}} < 0$. For the other phase periods ($n = 6$ and $n = 10$) the function $v_{\mathcal{PSS}}(\xi)$ shows a behavior similar to the case $n = 3$, i.e. fluctuation around a non-zero value so that Eq. (4.2) gives $v_{\mathcal{CS}} \neq 0$ for $n = 6$ and $n = 10$, too. In the second row of Table 4.1 the corresponding results for $v_{\mathcal{CS}}$ are summarized for the various phase periods. In the case of $n = 3$ and $n = 6$ the velocities obtained by performing asymptotically a linear fit to the mean position and averaging over the chaotic sea coincide very well. However, for $n = 10$ Eq. (4.1) predicts that the transport should be actually in the opposite direction than it is observed by simulating an ensemble of

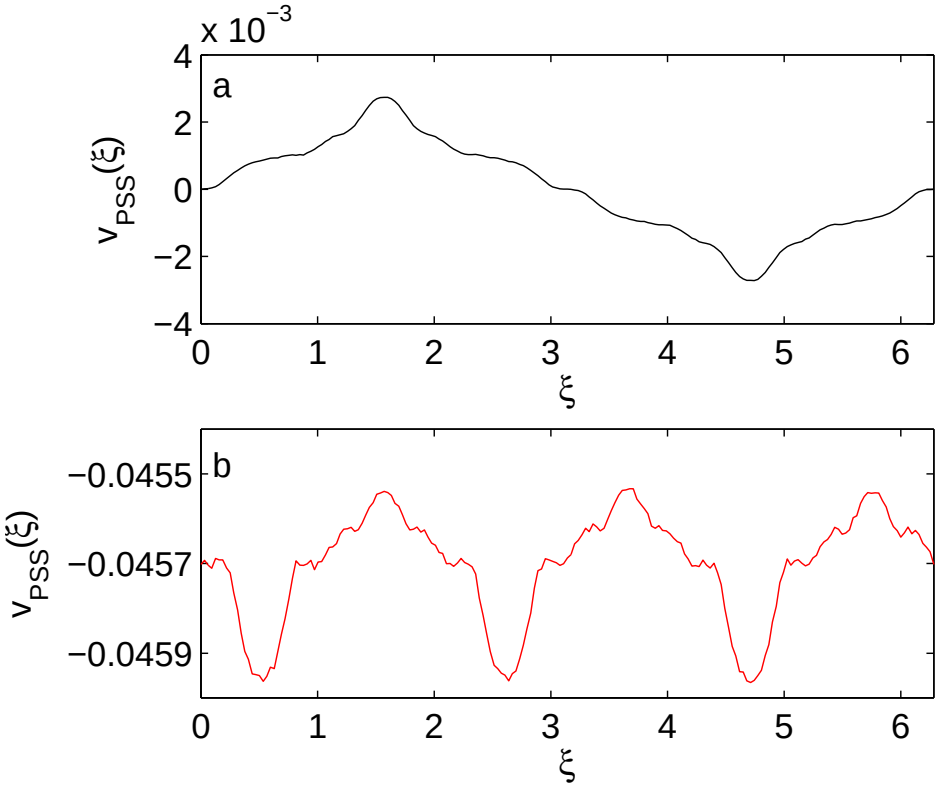

Figure 4.3: The average velocity of the chaotic sea in the PSS $v_{PSS}(\xi)$ as a function of the phase ξ of the driving, when the snapshot of the x/p-plane is done for the phase period (a) $n = 1$ and (b) $n = 3$.

particles. This contradiction can be resolved straightforwardly. According to our discussion of the PSS there are cantori in the chaotic parts of phase space. Depending on the system's parameters like phase period or potential height, the flux across them can become arbitrarily small and therefore these cantori restrict trajectories to certain subparts of phase space even for long simulation times but not asymptotically. In Sec. 3.4 their impact on the appearance of ballistic flights has been discussed. Yet, as we have indicated already in the discussion of the setup with the perturbed phase period three, there is of course the opposite effect, too. For trajectories starting with small momenta like our initial ensembles, the cantori prevent the particles even for long times from sampling the (transporting) phase space beyond the cantori. Indeed the surfaces of section of phase period $n = 10$ for $t < 10^6$ show that the region of the chaotic sea especially close to the FISC for positive momenta has not been visited by a single trajectory. Since this part of phase space corresponds to a positively valued drift, a transient transport in the opposite direction occurs in our case. In order to verify this explanation, a smaller initial ensemble has been simulated for a longer simulation time. For this simulation a zero crossing of $\langle x(t) \rangle$ is observed at $t_{\mathrm{cr}} \approx 1.3 \cdot 10^7$. After the zero crossing the mean position $\langle x(t) \rangle$ grows in the positive x-direction, which is predicted by Eq. (4.2). Moreover, for $t > t_{\mathrm{cr}}$ the region in the PSS close to the FISC for positive momenta gets sequentially visited by trajectories.

According to the above, the origin for the occurrence of directed transport is simply the

desymmetrization of the chaotic sea with respect to $p = 0$, i.e. for the phase periods larger than three the phase space volume of the chaotic sea with $p > 0$ and accordingly $p < 0$ are not equal anymore. An important manifestation of this asymmetry in the monochromatically driven lattices with phase periods is that the areas of elliptic islands with $w = r/s$ and $w = -r/s$ are different in the PSS. Usually, this phase space asymmetry is achieved by applying a biharmonic driving law to the static system [33, 37, 44, 47, 48, 51], such that the potential $V(x, t)$ of the Hamiltonian breaks both symmetries derived in [44]. However, from the discussion of the FISC in Sec. 3.3 we know that a kinematic approach to the single barrier dynamics explains already the asymmetry of the chaotic sea of the phase space with respect to $p = 0$, because the FISC, depending on the direction of the propagation, is located in different ranges of the velocity. Physically, this corresponds to an inequality of the maximal barrier velocity in positive and negative direction, which is absent for the harmonic driving law. Consequently, for the lattice with phase-modulated harmonically driven barriers this simple consideration, independently of the phase period, is not enough to explain the asymmetry.

4.1.2 Diffusion properties for constant phase gradients

In this section the diffusion properties of the driven lattice are discussed. To this end we calculate the variance $\sigma_x(t)$ for different phase periods n. Fig. 4.4 shows the evolution of $\sigma_x(t)$ in a double-logarithmic plot for $n = 1, 3, 6, 10$. The variance follows obviously a power-law, i.e. $\sigma_x(t) \propto t^\gamma$ with similar exponents γ. Performing an asymptotic linear fit to the curves yields that $0.65 \leq \gamma \leq 0.75$ for all n, i.e. the system shows universally super-diffusion in configuration space. Let us now discuss the origin of this behavior. In Sec. 2.3 it has been shown that every barrier possesses an elliptic island at $p = 0$ for $V_0 = 0.16$ and $l = 0.4$. Accordingly, the particles in the chaotic sea, which move diffusively through the lattice, can become sticky to this structure. Therefore they can remain in the scattering region of one barrier for many periods of the driving. On the contrary, the particles can perform ballistic flights. These events originate either from phases of motion during which the particles are confined by partial barriers to regions of phase space with non-zero average velocity or they are the result of stickiness to elliptic islands corresponding to periodic orbits, which travel through the lattice in the direction of their initial momentum (Sec. 3.4). Usually, strong partial barriers are close to the FISCs, where transporting islands are found, too. Consequently, both effects reinforce each other in this part of phase space, i.e. trajectories which are confined by a partial barrier and get additionally sticky to elliptic islands contribute to the longest ballistic flights in the system. These trajectories can be detected numerically very easily. We look simply for time intervals with a minimum length, where the sign of the velocity does not change upon interaction between the particle and the barriers, i.e. we search for ballistic flights. The corresponding probability distribution of the lengths of ballistic flights obeys a power law $p(t) \sim t^{-\nu}$, e.g. Fig. 4.5 (a) shows $p(t)$ for the case $n = 1$. The tail of the distribution is obviously very noisy which yields severe difficulties in extracting the exponent of the power-law. Therefore, in order to reduce statistical noise [80], we do not fit directly to $p(t)$, but calculate first the cumulative probability distribution function $P(t)$, which is defined by

$$P(t) = \int_t^\infty p(t')\, dt'. \tag{4.3}$$

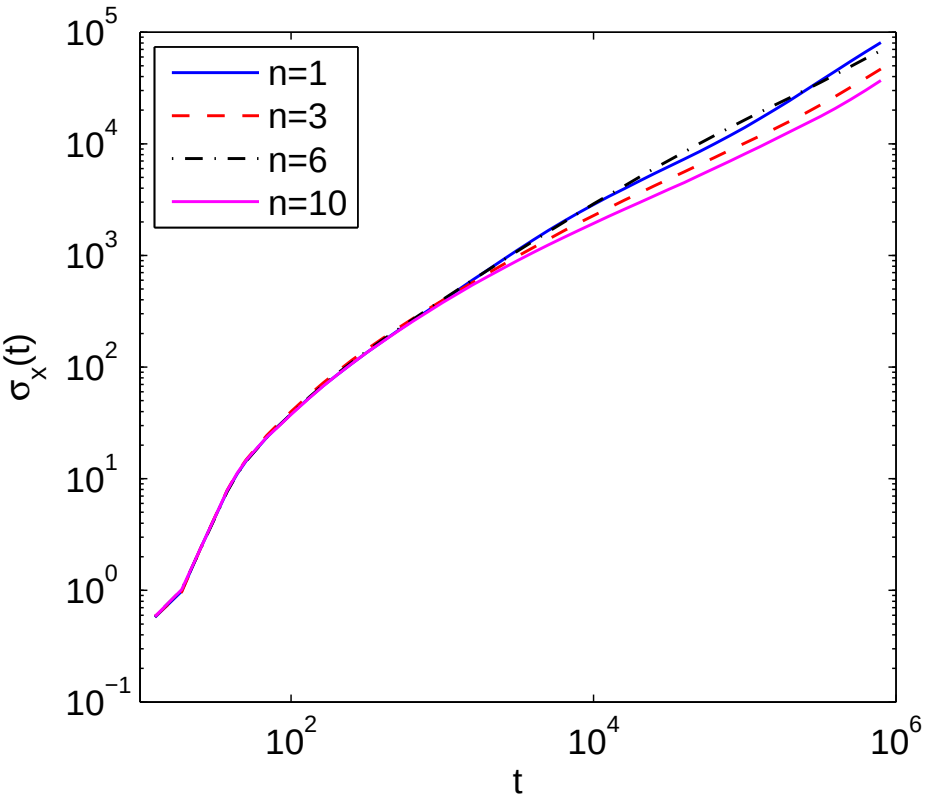

Figure 4.4: Double-logarithmic plot showing the evolution of the variance $\sigma_x(t)$ for an ensemble of particles initialized in the chaotic sea of phase space for the phase periods $n = 1, 3, 6, 10$. Performing an asymptotic linear fit yields $0.65 \leq \gamma \leq 0.75$ for all n.

Fig. 4.5 (b) shows $P(t)$ in a double-logarithmic plot for the various phase periods. Clearly, there is a power-law behavior of $P(t) \sim t^{-\mu}$ over several decades. The exponent can be estimated by a linear asymptotic least-square fit, which gives $1.41 \leq \mu \leq 1.65$ for all phase periods n. Due to Eq. (4.3) the probability distribution $p(t)$ follows thus a power law with the exponent $\nu = \mu + 1$, i.e. $2.41 \leq \nu \leq 2.65$. From continuous-time-random-walk (CTRW) theory [47,48,81] it is known that such an interplay between ballistic flights and waiting times yields anomalous diffusion in configuration space. Furthermore, CTRW theory predicts that between the exponents γ and μ the relation $2\gamma = 3 - \mu$ [82,83] holds. For our numerical data we have $0.65 \leq \gamma \leq 0.75$ and $1.41 \leq \mu \leq 1.65$. Therefore, this condition is quite well fulfilled.

In the previous chapter we have seen that the phase space is mixed for all considered setups and parameter regimes. In fact, this is the typical KAM-scenario in periodically driven Hamiltonian systems [5]. Particularly, we have always, embedded in the chaotic sea, ballistic islands associated to trajectories which traverse the lattice only in one direction. In Sec. 3.4 we have seen that stickiness to these regular structures is the most important origin of the ballistic flights interrupting constantly the diffusive dynamics of the particles. According to the discussion in the previous paragraph this effect leads to super-diffusion in coordinate space or in other words to a "faster broadening" of the spatial particle distribution. Consequently, we observe super-diffusion for all other setups as well, that is the variance $\sigma_x(t)$

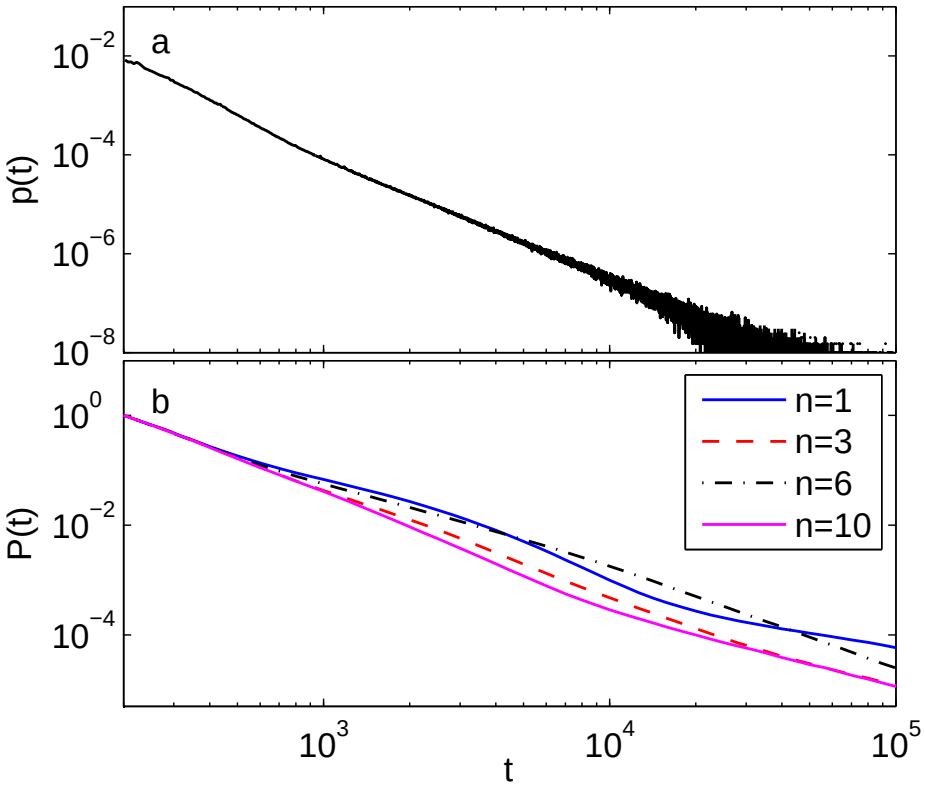

Figure 4.5: (a) The probability distribution for the lengths of ballistic flights in a uniformly driven lattice. i.e. $n = 1$. (b) The cumulative distribution function $P(t)$ for the different phase periods n is depicted where fitting a power-law yields for the exponent $1.41 \leq \mu \leq 1.65$.

follows asymptotically a power-law with an exponent $0.5 < \gamma < 1$.

4.1.3 Transport properties for the perturbed / broken phase gradient / biharmonic driving

Now we turn to the discussion of the transport properties of the lattice, where the equidistant phase gradient with period three is perturbed, i.e. each barrier is driven harmonically and equipped with a local phase shift according to the period three sequence $\{\cdot, 0, \frac{2\pi}{3}+\alpha, \frac{4\pi}{3}, \cdots\}$. Fig. 4.6 shows the transport velocity of the system as a function of the phase shift α of the "middle" barrier. For these setups and all the upcoming ones the transport velocity has been calculated exclusively by evaluating numerically Eq. (4.2) according to the procedure presented in Sec. 4.1.1, because this is much more efficient in terms of computational time than simulating the long term dynamics of a whole ensemble. The star in Fig. 4.6 marks the setup with $\alpha = -\frac{0.03\pi}{3}$ for which we obtain the PSS shown in Fig. 3.5 (b). Using this example one can again demonstrate very vivid the impact of the tuning of the asymmetric phase space on the direction of the transport. The PSS of the setup with equidistant phase period three, i.e. $\alpha = 0$, shown in Fig. 3.5 (a) corresponds to the system with transport velocity $v_{\mathcal{CS}}(\alpha = 0) = -0.0456$. By perturbing this equidistance of the gradient the formerly stable FISC dissolves and thus parts of the phase space volume with larger positive momenta

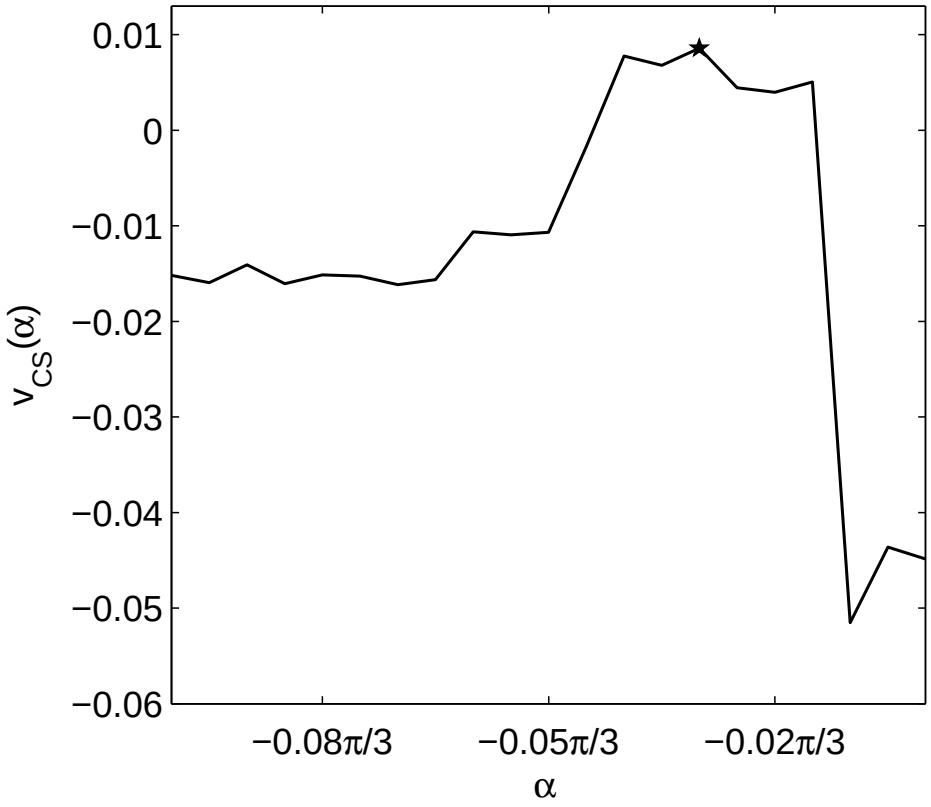

Figure 4.6: Transport velocity v_{mean}, as a function of the phase shift $\alpha = -\frac{0.1\pi}{3} \ldots 0$ of the "middle" barrier. With a star we have marked the setup, which we have chosen in Sec. 3.2.4 to produce the PSS shown in Fig. 3.5 (b).

become accessible to chaotic trajectories. At the same time, the remaining phase space, in particular the part with $p < 0$, remains basically unaffected, i.e. overall the phase space volume of the chaotic sea with $p > 0$ increases significantly. Therefore, the phase space average of the velocity over the chaotic sea in Eq. (4.1) and thus the direction of the transport changes its sign. For some values of α the directed transport vanishes, i.e. $v_{\mathcal{CS}}(\alpha) = 0$. Yet, this does not imply that a symmetry of type (2.4) or (2.21) is present. In fact both symmetries are broken. Nevertheless, the phase space volumes with $p > 0$ and $p < 0$ of the chaotic sea are accidentally equal for some values of α.

Let us now consider the transport properties of the setup with variable potential height and fixed phase gradient of period three $\{\ldots, 0, \frac{\pi}{10}, \frac{3\pi}{10}, 0, \frac{\pi}{10}, \frac{3\pi}{10}, \ldots\}$. As before the transport velocity is determined by evaluating Eq. (4.1) for the different global potential heights. Since with increasing potential height trapping between adjacent barriers occurs, it is important to choose the initial conditions carefully such that the particles are not launched in the "wrong" part of the PSS. Otherwise the result for $v_{\mathcal{CS}}$ would be completely falsified by those trajectories. In Table 4.2 the transport velocities for the broken phase gradient and different global potential heights is shown. Similarly to the previous setup, the directed transport can be tuned by varying a parameter, which is now the potential height.

In the following we discuss briefly the transport properties of the uniformly, biharmonically

V_0	2	13	22	32
$v_{\mathcal{CS}}$	0.0221	0.0404	0.0088	0.1201

Table 4.2: Transport velocities for different global potential heights V_0 and broken phase gradient obtained by averaging over the chaotic sea of the phase space.

driven lattice. For $V_0 = 0.16$ we obtain $v_{\mathcal{CS}} = -0.251$ by evaluating Eq. (4.1). The finding of a negative transport velocity $v_{\mathcal{CS}}$ approves quantitatively the discussion of the corresponding PSS in Sec. 3.2.6. There it has been elucidated that the PSS of the uniformly, biharmonically driven lattice is asymmetric with respect to $p = 0$. Specifically, the area of the chaotic sea with $p < 0$ is larger than the area with $p > 0$ independent of the phase of the PSS. Consequently, the volume of the chaotic sea in the complete phase space possesses as well a negative weight, i.e. according to Eq. (4.1) a transport in negative direction can be expected. We have explained the asymmetry of the PSS by the different velocity regimes of the FISCs which delimit the chaotic sea at positive and negative momentum. By means of a simple kinematic consideration this finding has been traced back to the maximal barrier velocity in positive v_+ and negative direction v_- respectively. For the biharmonic driving law we have found $|v_-| > |v_+|$ and thus a negative asymmetry of the chaotic sea in phase space. Roughly speaking, we can thus say that the transport points into the direction of the larger barrier velocity. For the biharmonic driving law v_+ and v_- can be tuned by e.g. introducing a phase shift, i.e.

$$f(t) = \cos(\omega t) + \sin(2(\omega t + \varphi)) \tag{4.4}$$

Varying φ changes v_+ and v_- and it is indeed observed that the transport direction shows to a good approximation the previously described behavior, i.e. positive transport for $|v_+| > |v_-|$ and vice versa [84].

4.1.4 Comparison of harmonic and biharmonic driving

In this section we compare qualitatively our results on directed transport for the cases of biharmonic and harmonic driving. An eye-catching feature of the biharmonic driving is that it leads to a transport velocity which is, compared to the setup with harmonic driving and constant phase gradient, approximately six to twelve times larger although the barrier parameters, i.e. potential height V_0, potential width l etc, are equal. Consequently, the biharmonic driving law must lead to a more pronounced phase space asymmetry with respect to $p = 0$. In the following we summarize the reasons for this behavior that we have found in the previous sections. In the discussion of the PSS (see Sec. 3.2.1) we have seen that breaking the time-reversal and parity symmetries of the Hamiltonian (Eq. (2.4) and (2.21)) by means of a harmonic driving with local phase shifts manifests in phase space in such a way that the elliptic islands with winding number $w = r/s$ and $w = -r/s$ do not have the same area in the PSS. As a result, this yields an asymmetry of the chaotic sea with respect to $p = 0$. Furthermore, we have explained that this asymmetry will give rise to directed transport, if it persists after an average over a complete phase of the driving. In Sec. 3.3 it has been elucidated that the FISCs delimiting the chaotic sea are located in the same momentum regimes because the maximal barrier velocity in positive and negative direction are equal, too. Exactly this fact makes the difference to the biharmonic driving law, where additionally

to the different area of the elliptic islands with winding number $w = r/s$ and $w = -r/s$ the FISC for positive momentum is not in the same regime as the FISC for negative momentum. As a result the phase space asymmetry is stronger and thus the transport velocity larger.

4.2 Localization of particles

This section is devoted to the discussion of the localization of particles. Let us start with a short summary of the different possibilities for trapping.

4.2.1 Mechanisms of particle localization

In general, there are three possibilities for trapping, which we have introduced in Chap. 3. In the case of small potential heights, which have been used for instance in the setups with monochromatic driving and a constant / perturbed phase gradient, this can be done by means of the elliptic island at $p = 0$ corresponding to trapping in a single barrier. For larger values of V_0 this regular structure is gone, but islands belonging to trapped trajectories between two barriers are present in phase space (see the discussion in Sec. 3.2.5). Furthermore, for $V_0 \geq 13$ there is the possibility of trapping particles in the confined chaotic seas. Finally, we want to remark that for setups with very specifically chosen potential heights and phase gradients it is possible to achieve regular, localized dynamics, which extends over the scattering regions of several barriers. However, this is a case, which requires fine-tuning, because the associated elliptic islands are very tiny and for the parameter regime chosen in our setups this kind of dynamics does not occur. In Sec. 3.2.5 it has been elucidated that the confined chaotic seas occur simultaneously between adjacent barriers with increasing potential height V_0 for the constant phase gradient. Due to the fact that the localization of particles is most sensitive to V_0 and since we want to control the sites at which trapping is established we focus on the monochromatically driven lattice with broken phase gradient, i.e. the sequence of phase shifts is $\{\ldots, 0, \frac{\pi}{10}, \frac{3\pi}{10}, \ldots\}$.

4.2.2 Localization properties for a broken phase gradient

In the course of the discussion of the diffusion properties (Sec. 4.1.2) it has been shown that the diffusive trajectories, which contribute to the directed current in the lattice, still obey long-time transient phases of motion during which they are localized in the scattering region of one barrier. For small potential heights these events originate from stickiness to the elliptic island at $p = 0$, whose properties are defined exclusively by (V_0, l). Since these parameters are equal for all barriers, i.e. a single barrier property [70], the stickiness of trajectories to this structure is identical independently of the phase periods: the particles get localized in the scattering region of the first, second etc. barrier on average for the same time. In the case of very large potential heights, e.g. $V_0 = 32$ for the broken phase gradient, there are confined chaotic seas between the barriers. Yet, the particles belonging to the directed flow cannot enter these regions in phase space, because these parts are separated by impenetrable tori.

In the following we will show that it is possible for certain parameter values to obtain a dynamics that exhibits phases of trapped motion in certain wells, i.e. in between certain definite barriers, of the driven unit cell of the lattice. To this end we look in the case of

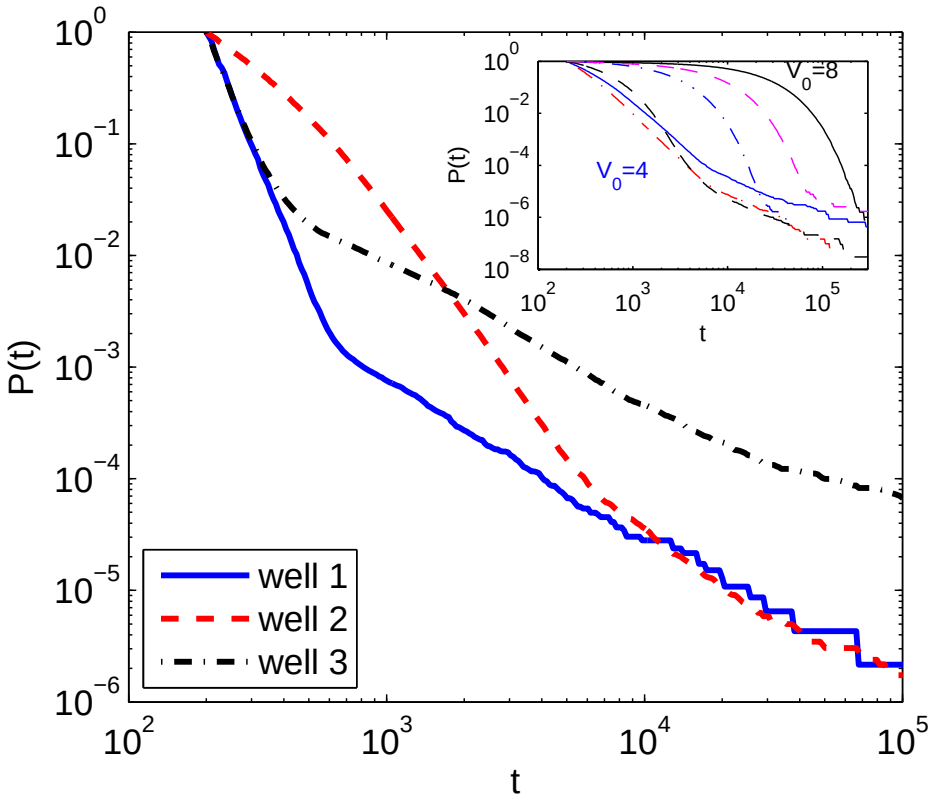

Figure 4.7: Cumulative distribution function $P(t)$ of the dwell time for the three different wells with fixed potential height $V_0 = 4$ for the lattice with broken phase gradient. In the inset $P(t)$ belonging to the second well for different values of $V_0 = 4 \ldots 8$ is shown.

the lattice with the broken phase gradient for time intervals during which the particles, that move diffusively through the lattice, are localized between two barriers. Fig. 4.7 shows for $V_0 = 4$ the cumulative probability distribution of dwell times $P(t)$ for particles between two consecutive barriers in one spatial unit cell, i.e. $i = -1$ to $i = 0$, $i = 0$ to $i = 1$ and $i = 1$ to $i = 2$, which will be labeled as well one, two and three, respectively. For this value of the potential height (see Sec. 3.2.5) the elliptic island at $p = 0$ has disappeared and thus there is no stickiness to this regular structure anymore. Furthermore, no trapped chaotic dynamics between barriers is possible. Instead all chaotic trajectories in the large chaotic sea move diffusively through the lattice. Obviously, $P(t)$ is not equal for the different wells. A particle, which has been localized in the first well is trapped with less probability (for a time span $t \geq 10^3$) compared to a particle trapped in the third well. By recalling the discussion of the PSS for this values of V_0 in Sec. 3.2.5 this behavior can be resolved. Accordingly, with increasing potential height the particles bouncing between two neighboring barriers are able to probe parts of the phase space of the corresponding FUM, which are located at higher momentum. However, the phase space of the FUM in general is very sensitive to the phase relations the walls have with respect to each other. Not only the position in momentum space of the FISC p_b, but also both the momentum p_s below which the FUM is completely chaotic and the momentum of elliptic islands belonging to trajectories shown in Fig. 3.7 (b)

depend critically on the phase relations between the barriers. Due to the non-equidistant gradient these phase relations are not equal, i.e. the barriers belonging to different wells possess different relative phases with respect to each other. Thus, for a fixed potential height it is possible that in a certain well only the chaotic part of the corresponding FUM's phase space is accessible to the particles, whereas in another well already elliptic islands embedded in the chaotic sea are present. Escape rates from these different parts of phase space are understandably not equal, because stickiness to regular structure leads to phases of motion during which particles are trapped for long times between two barriers. By changing the phase gradient for a fixed potential height, it is possible to "engineer" the phase space of the lattice in such a way that the events with very long dwell times take place only at specific positions. Nevertheless, the trapping is only transient so far, i.e. the particles leave eventually the wells again. If the localization shall be permanent, then the potential height V_0 has to be increased instantaneously at a certain time ("ramping") [85]. For example, by ramping the potential in the lattice with broken phase gradient from $V_0 = 2$ to $V_0 = 13$ one switches instantaneously from the PSS shown in Fig. 3.6 (a) to (b). As a result of the ramp of V_0 the particle are trapped in the localized chaotic seas between adjacent barriers forever. An interesting perspective is to combine this mechanism of localization with the transport properties. Accordingly, an ensemble of diffusive particles can be transported to a certain position in the lattice and afterwards trapped there in a pattern which can be manipulated by the phase gradient [85]. Of course, trajectories can also stay for a comparatively long time in a well, which does not contain any elliptic island at all, which is due to the so-called *low velocity peaks* [86]. Particles, that are slightly faster than the barrier at a collision, get decelerated to a very small velocity v_ϵ but still leave the scattering region without experiencing a second collision. Afterwards they travel the spatial distance between the scattering regions of two barriers, which yields for the dwell time $t_d = \frac{D-l-2C}{v_\epsilon}$. Yet, the portion of trajectories, which are "trapped" according to this mechanism, is negligible. For $V_0 = 4$ all wells contain elliptic islands. In fact, the characteristic asymptotic power-law behavior $P(t) \sim t^{-\mu}$ of the cumulative probability distributions of dwell times is a hallmark of the associated stickiness to this regular structure in phase space. Generally, whenever a region in phase space contains elliptic islands, the occurrence of long algebraic tails in the escape rate is generic [76]. Indeed, we observe that the exponent of the probability distribution $p(t) \sim t^{-\nu}$, which is related to the exponent of the cumulative distribution $P(t)$ through the equation $\nu = \mu + 1$, is always larger than two. Similarly to the setups with small potential height V_0 and constant phase gradient the dynamics shows the characteristic interplay between ballistic flights and waiting times. Accordingly, we find that there is super-diffusion in coordinate space even for very large values of V_0.

4.2.3 Impact of potential height on localization properties

In this section discuss we discuss how the variation of V_0 influences $P(t)$ for a given well. In the inset of Fig. 4.7 the cumulative probability distribution of the dwell time in the second well for various values of V_0 between 4 and 8 is shown. With increasing V_0 this is the first well with a localized chaotic sea (see Fig. 3.6 (b)). Especially for small and intermediate dwell times ($10^2 < t < 3 \cdot 10^3$) the function $P(t)$ changes significantly. $P(t)$ decreases less rapidly for larger values of V_0, which is understandable, because with increasing potential height the particles need to accumulate more collisions in order to become fast enough to surpass the

potential. Still, by doubling V_0 the probability for the particles to be trapped in the well for dwell times longer than 10^4 grows up five orders of magnitude. Furthermore, the PSSs of trajectories with dwell times in this range show that beside the particles, which are sticky to elliptic islands, a great portion still obeys chaotic dynamics. In order to answer the question how chaotic particles, which move diffusively through the lattice, can be trapped between two barriers for such a long time, we have to exploit one more time the FUM. Close to the FISC of the FUM exist again cantori with small flux across them. Depending on the properties of these partial barriers the particles obeying chaotic dynamics are prevented for a significant time from sampling the phase space of the FUM, which is located at high momenta close to the FISC and associated to the kinetic energy a trajectory has to gain in order to leave the well. Consequently, once the potential height is chosen such that this cantori are stabilized, the escape rate from the region between barriers is lowered significantly.

Chapter 5

Block-structured lattices

This chapter is devoted to the study of henceforth called "block-structured driven lattices" which are reminiscent of superlattices in the physics of semiconductor heterostructures but with a spatiotemporal embedding. Specifically, the system under investigation consists of a lattice of domains or blocks, each containing many unit cells which are exposed to different time-periodic forces. The driving is chosen such that neighboring domains possess oppositely directed currents ("local" ratchets). At the interfaces between the differently driven domains trajectories exhibit crossovers from diffusive to ballistic dynamics and vice versa. Our focus is the analysis of the non-equilibrium dynamics in such bimodally driven devices leading to these dynamical conversion processes.

5.1 Setup and transport properties of the lattice

Evidently, the Hamiltonian of the block-structured driven lattice is given as before by equation (2.1). In order to create domains in the lattice with locally different particle currents we have chosen for the site-dependent driving law $f_i(t)$ the following form

$$f_i(t) = (-1)^{\lfloor i/N \rfloor}\, g(t), \tag{5.1}$$

where $\lfloor x \rfloor$ is the largest integer k with $k \leq x$ and $g(t) = C\{\cos(\omega t) + \sin(2\omega t)\}$ is the biharmonic driving. Thus, the lattice is composed of domains each consisting of N later-

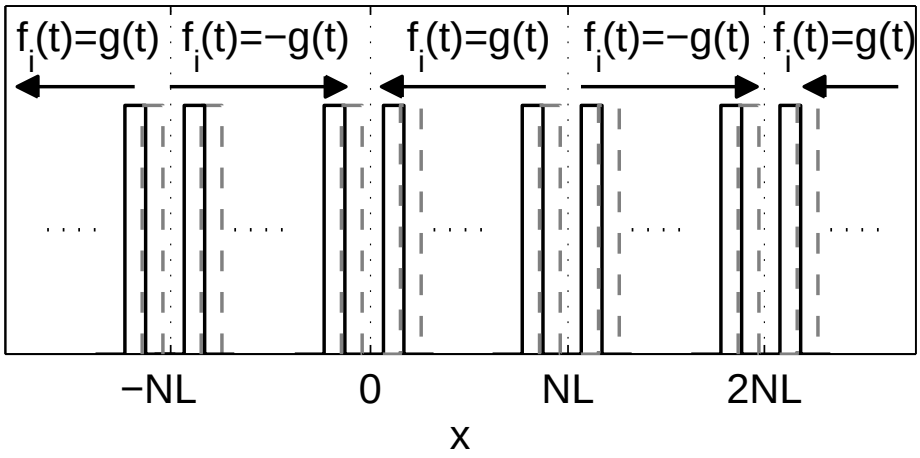

Figure 5.1: Schematic illustration of the driven lattice. Interfaces between the domains with different driving laws are at the positions $\{0, \pm NL, \pm 2NL\}$. Arrows indicate the direction of the local currents.

ally oscillating barriers obeying the same driving law and which are connected at positions $\{0, \pm NL, \pm 2NL \ldots\}$ called "interfaces" in the following (Fig. 5.1). Each domain possesses the length $L_\mathrm{B} = N \cdot L$ ($N = 10^4$), where L is the equilibrium distance of neighboring barriers and, as shown in Fig. 5.1, the driving law $f_i(t)$ alternates from one domain to the next. The amplitude C of the driving is fixed such that $-1 \leq g(t) \leq 1$, i.e. $C \approx 0.57$ like for the phase-modulated driven lattices. Without loss of generality we can fix $\omega = 1$ and $m = 1$. Furthermore, we assume for the other parameters $l = 1$, $V_0 = 2.2$ and $L = 5$.

5.2 Transport properties of the lattice

According to the results of the previous chapter applying the biharmonic driving law $g(t)$ to the entire lattice leads to directed transport. Fig. 5.2 shows the stroboscopic Poincaré surface of section (PSS) of the laterally oscillating lattice for $g(t) = C\{\cos(\omega t) + \sin(2\omega t)\}$ (amplitude $C \approx 0.57$, potential height $V_0 = 2.2$, barrier width $l = 1$, length of the unit cell $L = 5$). Evidently, the PSS reveals the typical mixed structure of the phase space. For momenta $|p| \gtrsim 4.3$ the dynamics is mostly regular, i.e. in this region the phase space is foliated predominantly by deformed tori of the unperturbed system. A big elliptic island centered around a period one orbit at $x \approx 0, p \approx -4.9$ is encountered. Furthermore, we observe a chaotic sea confined by invariant curves to $3.9 \lesssim p \lesssim 4.3$. Trajectories which start in this chaotic layer traverse the lattice in positive direction whereas particles starting in the large sea ($-4.3 \lesssim p \lesssim 3.9$) obey diffusive dynamics. Trajectories belonging to the embedded regular islands travel only in the direction of their initial momentum. The white rectangular area is due to illustrative reasons its origin has been elucidated in Sec. 3.2. Fig. 5.2 reveals an asymmetry of the chaotic sea with respect to $p = 0$, that is the area of the chaotic sea in the PSS with $p < 0$ is larger than the area with $p > 0$ which persists if the PSS is done for another phase of driving. According to the discussion in the previous chapter we expect therefore a negative transport velocity v_T. Performing the integration over the chaotic sea in phase space (see Eq. (4.1)) yields $v_\mathrm{T} = -0.2649$. Consequently, in a domain with the driving law $f_i(t) = g(t)$ the particles in the chaotic sea are hence on average transported in negative x-direction. Since the driving changes its sign from one domain to the next one, i.e. $f_{i+N}(t) = -f_i(t)$, the direction of the local current alternates, too, and transport is reversed. There are two types of interfaces that repeat in an alternating manner in the lattice. One type is characterized by incoming ("convergent") currents from both neighboring domains whereas the second one has outgoing ("divergent") currents pointing towards the neighboring interfaces (see Fig. 5.1). Naturally, one could therefore expect that interfaces with incoming currents show particle accumulation whereas those with outgoing currents exhibit particle depletion. Although each domain shows directed transport and an according local drift of the particles, the complete lattice consisting of infinitely many domains does not exhibit directed currents since the equations of motion are invariant under the transformation [44]

$$T : x \to -x + NL,\ t \to t. \tag{5.2}$$

Yet, an ensemble of particles reaches this zero current limit of the complete driven lattice only for extremely long time scales by far not reached for the results shown in upcoming sections.

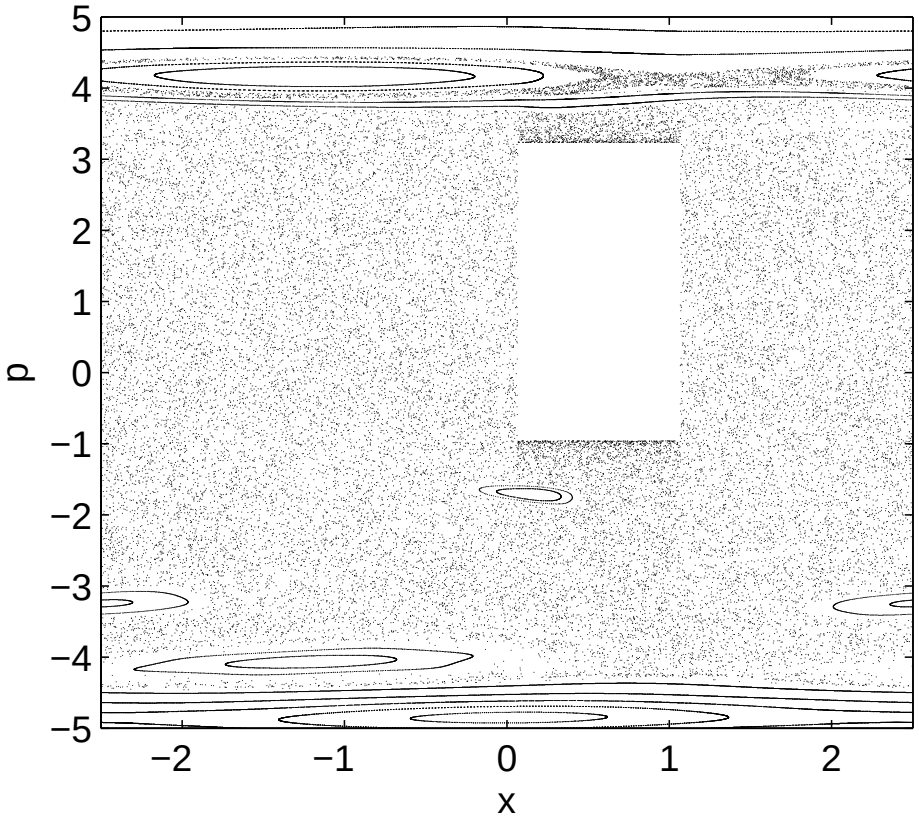

Figure 5.2: Stroboscopic Poincaré surface of section (PSS) for a lattice with biharmonic driving law $g(t) = C\{\cos(\omega t) + \sin(2\omega t)\}$ ($C \approx 0.57$, $V_0 = 2.2$, $l = 1$, $L = 5$)

5.3 Single particle dynamics

In this section we derive an intuitive understanding of the dynamics in such block-structured driven lattice by studying trajectories belonging to single particles. To this end figure 5.3 shows four trajectories with small initial velocities corresponding to the chaotic sea of phase space. Let us first look at the trajectory starting from the the origin of the lattice (blue curve in Fig. 5.3). Obviously, the dynamics consists of alternating phases of chaotic (diffusive) and ballistic behavior. Initially, the particle remains localized in a spatial region close to the interface because the local currents of the adjacent blocks are incoming at this position. After some time it starts to propagate ballistically opposite to the direction of the local particle current until it reaches the next interface at $x = -0.5 \cdot 10^5$ where a conversion to chaotic dynamics occurs. In the next domain ($-0.5 \cdot 10^5 \leq x \leq -1 \cdot 10^5$) the trajectory diffuses chaotically with a net drift in direction of the local current. When it arrives at the second interface a conversion back to ballistic behavior is observed. The dynamical conversion process repeats at each interface until we have stopped the simulation at $t = 10^6$. The trajectory starting at $x = -3 \cdot 10^5$ (black curve in Fig. 5.3) shows in the beginning a similar behavior. After a short time during which the particle is localized close to the interface a ballistic flight starts opposite to the direction of the current in the adjacent block until it reaches the

interface at $x = -2.5 \cdot 10^5$ where a conversion to diffusive dynamics occurs. Afterwards, the particle moves chaotically through the subsequent domain. Once it reaches the next interface at $x = -2 \cdot 10^5$ a dynamical crossover back to ballistic dynamics occurs. However, this time the particle continues its flight until it reaches the interface at $x = 0.5 \cdot 10^5$. Accordingly, the ballistic flight lasts over five blocks. Afterwards, the trajectory shows again the typical behavior of alternating phases of ballistic and chaotic dynamics on the scale of one block. A remarkable feature of the particle starting close to $x = 2 \cdot 10^5$ (red curve in Fig. 5.3) is that its trajectory is reflected at two consecutive interfaces which can be seen in figure 5.3 at $t \approx 7 \cdot 10^5 - 7.5 \cdot 10^5$. During this period the particle traverses ballistically the same block three times. Finally, the trajectory corresponding to the initial condition close to $x \approx -4 \cdot 10^5$ (green curve in Fig. 5.3) reveals that the ballistic flights need not to start always at an interface. Instead in this case the ballistic flight begins in the middle of a block at $t \approx 7.9 \cdot 10^5$, $x \approx -2.25 \cdot 10^5$ and stops at $t \approx 7.9 \cdot 10^5$ when the particles reaches the interface at $x = -1.5 \cdot 10^5$. Such ballistic flights which do not start at an interface are due to stickiness of the particles to the ballistic islands in phase space. Nevertheless, Fig. 5.3 reveals that most ballistic flights begin and end at the position of an interface.

Besides the fact that particles can change their dynamical character (ballistic / chaotic) when the corresponding trajectory crosses an interface between differently driven domains we observe that a block is never (or very rarely) traversed chaotically opposite to the direction of the local current. We can understand this behavior straightforwardly. According to the previous section the particles obeying chaotic dynamics in a domain are subjected to the local directed transport. Consequently, when a diffusive trajectory enters a block opposite to the direction of the chaotic drift velocity it is most likely transported back to the interface. A particle in the chaotic sea can traverse the domain only if it enters with a high velocity close to the FISC of the PSS which is not very probable or when the block contains few barriers. Since each domain consists of 10^4 barriers, it is therefore an unlikely event that the particles traverse diffusively a block opposite to the direction of the local current.

5.3.1 Dynamical conversion processes

Let us now derive an understanding of the origin for the dynamical conversion processes of trajectories happening at the interfaces. In the following we trace this behavior back to the overlap of different phase space components at the interfaces of adjacent blocks which can be understood simplest by visualizing the dynamics by means of the "Poincaré surface of section of a domain". In simple terms, the PSSD for a block with driving law $g(t)$ is just the Poincaré surface of section of a lattice with global driving $g(t)$. Consequently, the PSSD cannot capture the asymptotic behavior of a trajectory. Still, for the description of the transient dynamics in the block structured lattice characteristic for times $t \leq 10^6$ and especially for the understanding of the dynamical conversion processes the PSS of a domain (PSSD) is adequate.[1] The stroboscopic PSSD for a block with the driving law $g(t) = C\{\cos(\omega t) + \sin(2\omega t)\}$ is identical to the PSS of a lattice exposed to $g(t)$ which is shown in Fig. 5.2. Yet, since the particles are injected from the phase space belonging to the domain with driving law $g(t)$ to the other phase space associated to $-g(t)$ or vice versa by

[1] A super PSS containing the detailed dynamics for times up to $t \gg 10^7$ over the entire lattice possesses an enormously rich structure at any scale and is in practice inaccessible. Furthermore, the structure of this super PSS determines the asymptotic dynamics for $t \gg 10^7$ which are anyway not the focus of this chapter.

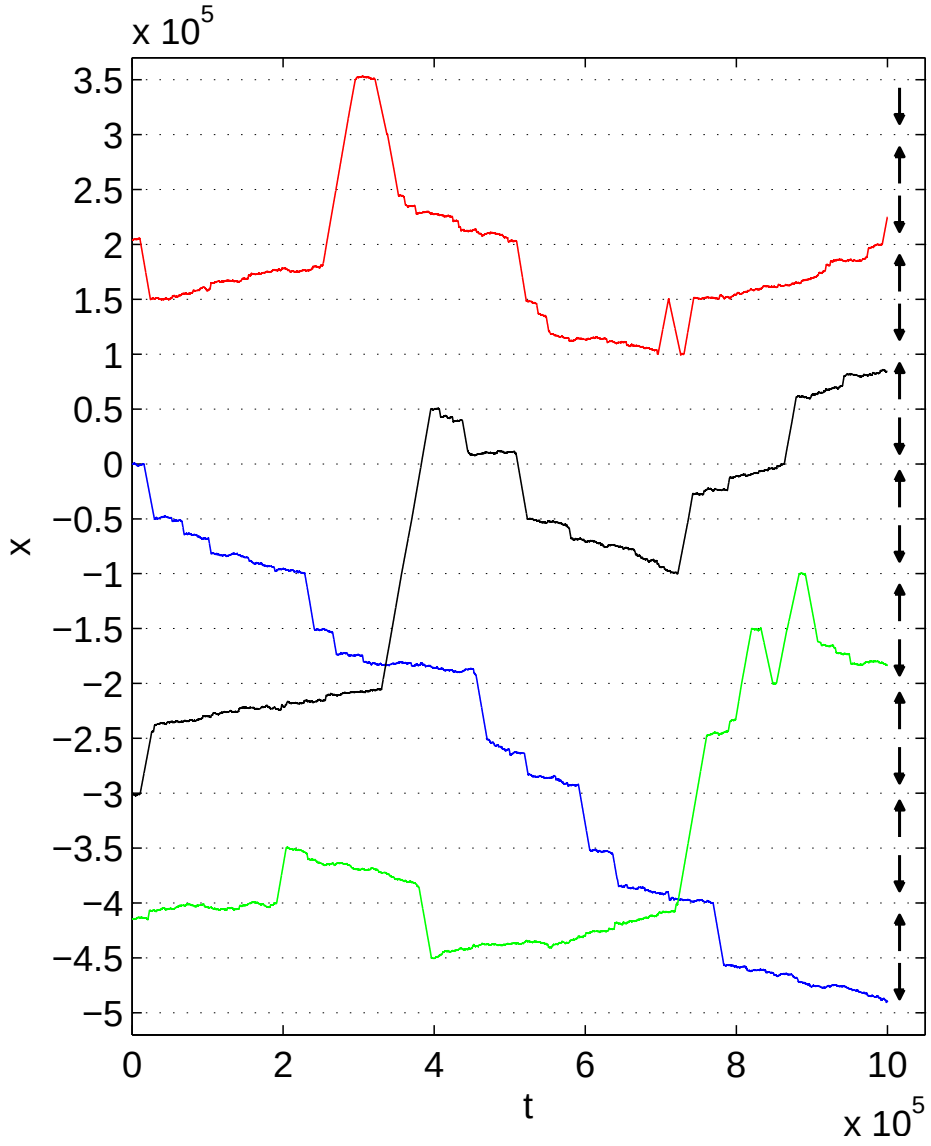

Figure 5.3: Individual trajectories launched at various positions in the block-structured lattice in different transporting blocks ($C \approx 0.57$, $V_0 = 2.2$, $l = 1$, $L = 5$).

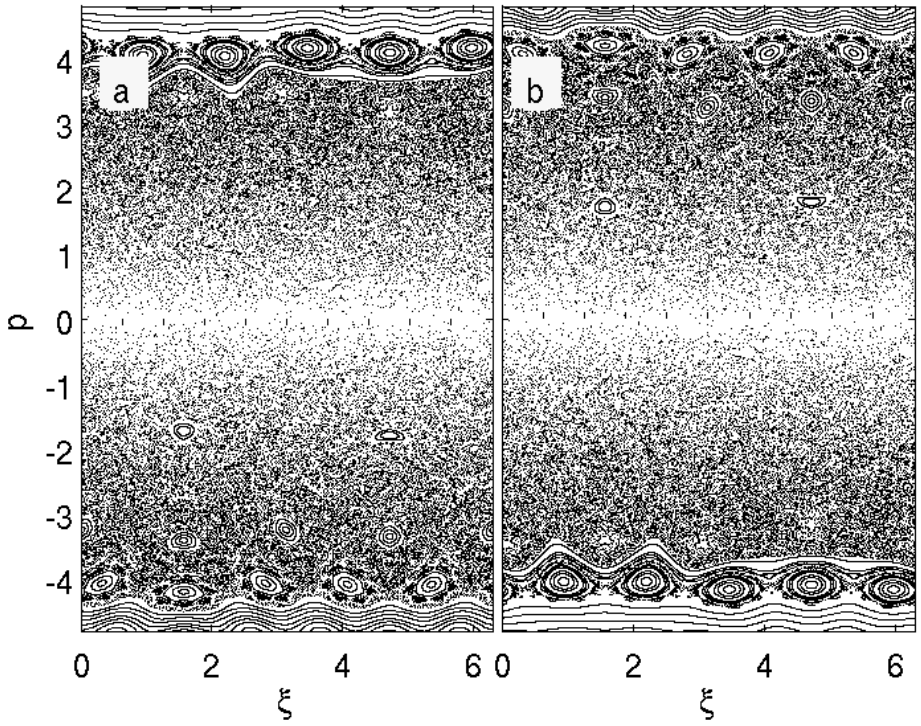

Figure 5.4: (a) shows the "momentum versus phase" Poincaré surface of section for single domain (PSSD) of the lattice with $g(t) = C\{\cos(\omega t) + \sin(2\omega t)\}$ ($C \approx 0.57$, $V_0 = 2.2$, $l = 1$, $L = 5$). (b) shows the PSSD for the block with driving $-g(t)$.

crossing an interface, their dynamical state at a certain point in space matters. Accordingly, the "momentum versus phase" Poincaré surface of section, that is a cut along the ξ-p-plane through the three-dimensional phase space, is most suitable for the following discussion (for details see Sec. 3.2). Fig. 5.4 (a) reveals that the "momentum versus phase" PSSD possesses qualitatively the same structure as the stroboscopic PSSD shown in Fig. 5.2. We observe a mixed phase phase with a large chaotic sea and embedded elliptic islands. Still, the number of islands is not equal in Fig. 5.2 and 5.4 (a) respectively, e.g. for $3.7 \lesssim p \lesssim 4.5$ Fig. 5.4 (a) shows a sequence of five elliptic with a surrounding chaotic layer, whereas in Fig. 5.2 there is only one island. (for a corresponding discussion see Sec. 3.2). As we see, the PSSD shown in Fig. 5.4 (a) is asymmetric with respect to $p = 0$, e.g. the area of the chaotic sea in the PSSD with $p < 0$ and $p > 0$ is not equal. Domains with driving laws $g(t)$ and $-g(t)$ possess mirror symmetric PSSDs with respect to $p = 0$ (compare Fig. 5.4 (a) and (b)). At the interfaces between the regions with different driving laws the PSSDs of the two domains are concatenated. By crossing such an interface it is thus possible that a trajectory is injected from one phase space component to another, e.g. from the chaotic sea into a ballistic island or vice versa. In the following we explain this behavior in more detail.

For example, let us consider a particle which is started in the block with positive local directed transport, i.e. it is launched in the phase space corresponding to the PSSD shown Fig. 5.4 (b). Furthermore, we assume that the particle has been started in one of the elliptic islands located at $\xi \approx 1.58$, $p \approx 1.73$ and $\xi \approx 4.73$, $p \approx 1.78$ which belong to an orbit with

period two in the PSSD. In an infinite lattice where the driving law $-g(t)$ is applied everywhere this initial condition would correspond to a trajectory traveling ballistically into the positive direction forever. Accordingly, in the present case the particle traverses ballistically the block where it has been started. Once the trajectory arrives at the interface an injection into the phase space belonging to the domain with driving law $g(t)$ occurs. In order to determine the particle's dynamical state in the next block we have to overlap the corresponding PSSDs. Since the trajectory comes from a block with driving law $-g(t)$ and is injected with positive momentum into a domain driven according to $g(t)$, the upper half ($p > 0$) of the PSSDs associated to the driving law $-g(t)$ and $g(t)$ must be overlapped. In doing so, it is obvious that the two elliptic islands at $\xi \approx 1.58$, $p \approx 1.73$ and $\xi \approx 4.73$, $p \approx 1.78$ in Fig. 5.4 (b) in which we have started the initial condition are mapped completely onto the chaotic sea in Fig. 5.4 (a). Consequently, the particle experiences by crossing the interface a crossover in its dynamical state from ballistic to chaotic motion. In the adjacent block the trajectory moves thus diffusively until it reaches next time an edge of the domain.

Similarly, it can also happen that a particle obeying chaotic dynamics becomes ballistic after it crosses an interface. To see this let us consider a trajectory which is started in the chaotic sea of a block with positive local current (PSSD shown in Fig. 5.4 (b)), i.e. the particle experiences a drift in positive direction. Moreover, let us assume that the trajectory is in the high momentum part of the chaotic sea surrounding the chain of elliptic islands at $p \approx 4$ (Fig. 5.4) when it crosses the interface and is injected into the phase space of the block with driving law $g(t)$ possessing negative transport velocity (PSSD shown in Fig. 5.4 (a)). Analogous to the discussion in the previous paragraph we have to overlap the upper half ($p > 0$) of the two PSSDs shown in Figs. 5.4 (a) and (b) in order to determine the particle's dynamical state in the next domain. Evidently, the high momentum part $p \gtrsim 3.5$ of the chaotic sea of phase space belonging to the domain with driving law $-g(t)$ is mapped largely onto the region above the FISC in the phase space corresponding to the domain driven according to $g(t)$ (compare Figs. 5.4 (a) and (b)). In an infinite lattice with global driving $g(t)$ this phase space part above the FISC belongs to particles which travel ballistically in the positive direction. Hence, in the present case the trajectory experiences a crossover from diffusive to ballistic dynamics and traverses ballistically the block with driving $g(t)$ until it arrives at the next interface.

Proceeding in this vein with the other phase space structures it stands to reason that the dynamics of particles can also remain ballistic or chaotic by crossing an interface between differently driven domains in the lattice. For example, if a diffusive trajectory, which is started in a block with driving law $-g(t)$, possesses the momentum $0 \lesssim p \lesssim 3.5$ when it enters the domain driven according to $g(t)$ its dynamics will remain chaotic. In this range of the momentum the chaotic sea of the PSSD belonging to the block with driving $-g(t)$ is mapped entirely on the chaotic sea of the domain with driving $g(t)$.

Let us now show that the conversion properties of the interfaces with incoming and outgoing flux are not equal. To this end we start by discussing the interfaces with convergent current (Fig.5.5 (a)) In this case the question whether a particles experiences a change in its dynamical character (ballistic / chaotic) or not can be answered in the following way. When a trajectory crosses the interface from the block with positive local current (block I) to the domain with negative transport velocity (block II) it is injected from the part with $p > 0$ of the PSSD of block I to the corresponding part in the PSSD of block II (Fig. 5.5 (a)). Consequently, a dynamical conversion process will occur, if the particle's position in the two PSSDs do

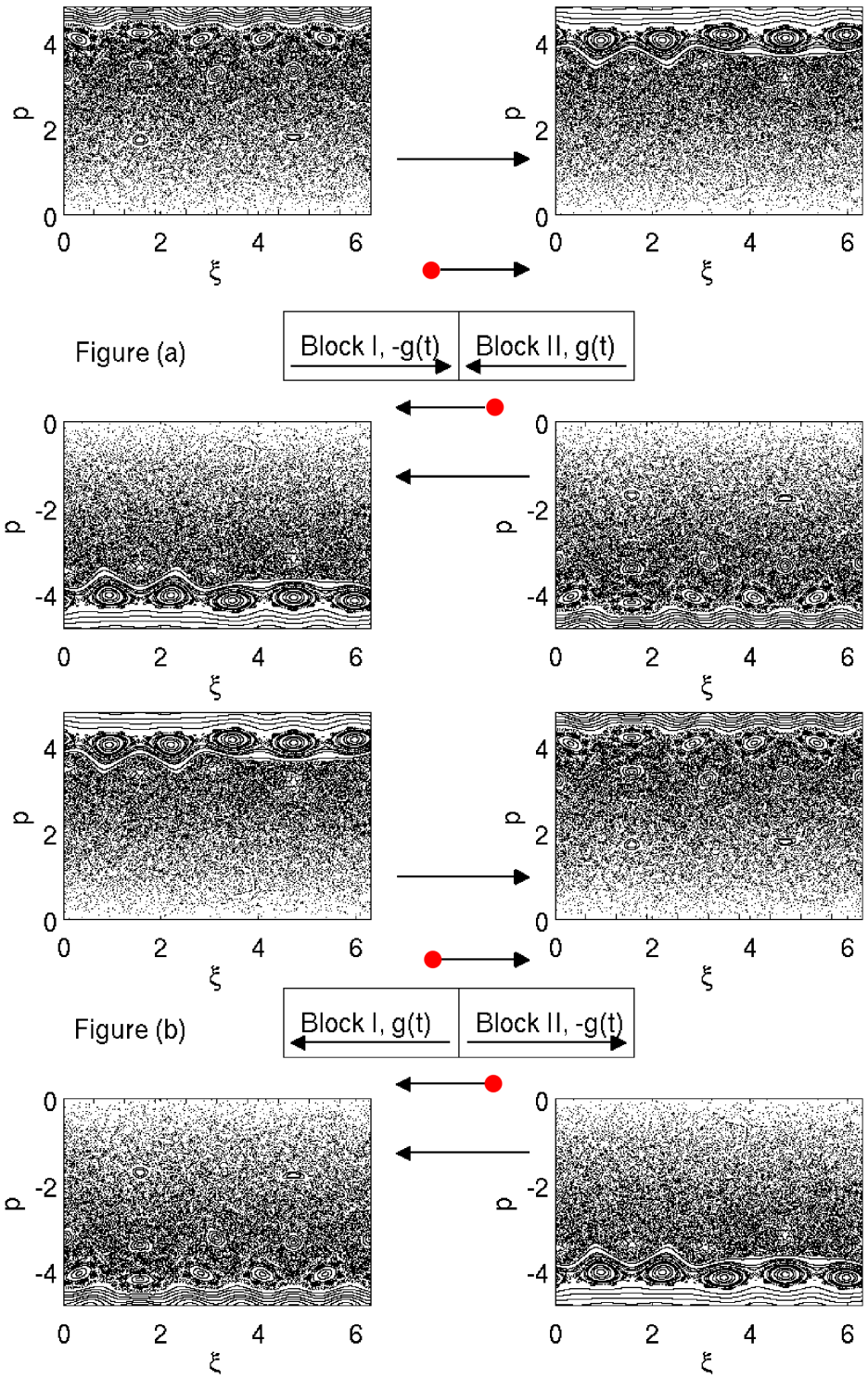

Figure 5.5: In Fig. (a) / (b) it is shown between which phase spaces the injection of the particle takes place when it crosses an interface with convergent / divergent flux. For example, in the upper part of Fig. (a) a particle crosses an interface with incoming current from block I to block II. In the PSSD this crossing corresponds to an injection from the left PSSD to the right one. In the lower part of Fig. (a) where the trajectory enters block I coming from block II the injection process happens evidently between other PSSDs. Fig. (b) visualizes the corresponding processes at an interface with outgoing currents.

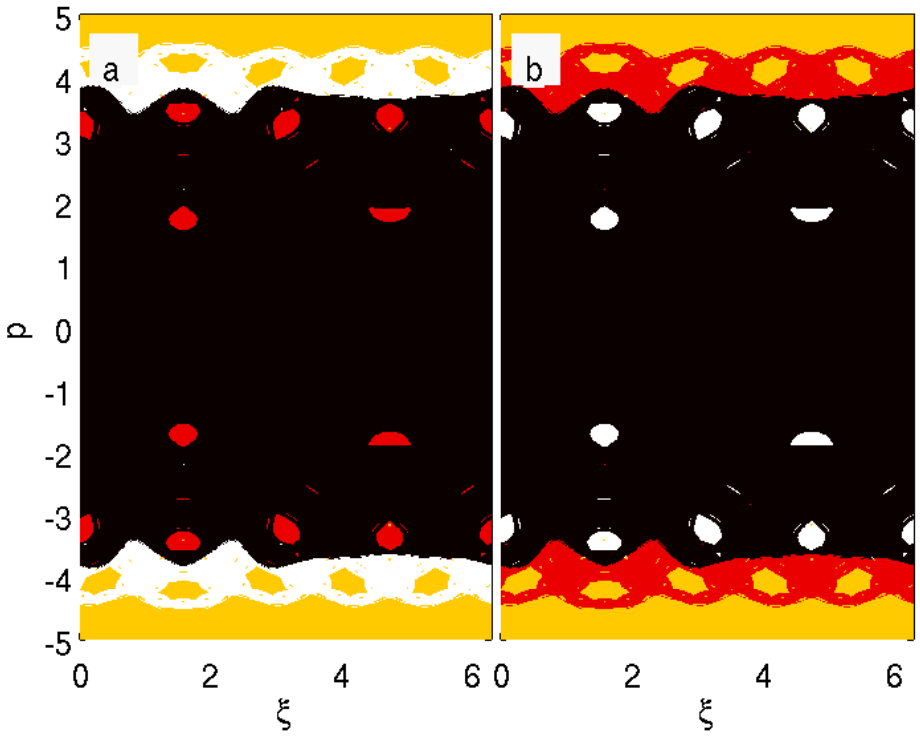

Figure 5.6: (a) and (b) show both the so-called "conversion sections" of an interface with incoming (a) and outgoing (b) current. The different colors symbolize the various possible conversion processes which can happen when a particle crosses an interface, e.g. white stands for a trajectory which experiences a crossover from diffusive to ballistic dynamics (for details see Sec. 5.3).

not belong to the same phase space component. For example, a diffusive particle in block I becomes ballistic in block II when it is injected from the chaotic sea in the PSSD of block I in a ballistic island or in the region above the FISC in the PSSD of block II (Fig. 5.5 (a)). Similarly, the other conversion process from ballistic to diffusive motion can be also classified by means of the PSSDs. For a trajectory crossing the interface from block II to block I the situation is similar. In this case the particle is injected from the lower part ($p < 0$) of the PSSD of block II to the corresponding part of the PSSD of block I (Fig. 5.5 (a)). Let us now discuss the conversion properties of an interface with outgoing currents (Fig. 5.5 (b)). A particle going from block I to block II is injected from the positive momentum part of the PSSD of block I to the corresponding part of the PSSD of block II and vice versa for a trajectory going from block II to I. By comparing Figs. 5.5(a) and (b) we see that the phase space injection processes at an interface with outgoing and incoming flux occur not in the same manner. More precisely, although the involved parts of the PSSDs are equal in both cases, the injection processes happen in the PSSDs in the reverse order. It is evident that this fact makes a big difference. For example, a diffusive particle going from block I to II at an interface with incoming flux can be injected into the region of phase space above the FISC whereas at an interface with outgoing flux it can only enter ballistic islands.

5.3.2 Conversion sections

The previous discussion is visualized in Figs. 5.6 (a) and (b) which are obtained by overlapping appropriately the PSSDs according to the just presented scheme. Specifically, Fig. 5.6 (a) shows in a color-code the various conversion processes as a function of the phase and the momentum when a particle crosses an interface with convergent flux from both sides. For example, the red area stands for regular structure which is mapped onto the chaotic sea, i.e. for the conversion of ballistic to diffusive motion. Accordingly, if the phase of the driving and the particle's momentum fall into a red marked area when the trajectory crosses the interface, then the particle experiences a crossover from regular to chaotic dynamics. Analogous black, white and yellow stand for processes with chaotic to chaotic, chaotic to ballistic and ballistic to ballistic conversion. Fig. 5.6 (b) shows the same information for the interface with divergent flux. In the following we will call these plots for reasons of brevity "conversion sections". Both figures are mirror-symmetric with respect to $p = 0$ which reflects only the mirror-symmetry of the PSSDs of the two blocks. Furthermore, the figures reveal one remarkable characteristic of the conversion properties of the two different interfaces. The area describing the ballistic to chaotic conversions (red color) in Fig. 5.6 (a) is identical to the area associated with the opposite (chaotic to ballistic) process in Fig. 5.6 (b) and vice versa. Thus it is a very likely event that a trajectory which is injected from the chaotic sea into regular structure experiences a conversion back to chaotic sea once it reaches the next interface which gives rise to the typical dynamics of alternating phases of diffusive and ballistic motion on the scale of one block (see Fig. 5.3). Nevertheless, the conversion back to chaos does not occur always and the reasons for this are discussed in the following.

Fig. 5.7 (a) shows an extract of the blue trajectory in Fig. 5.3 for $t \leq 1.6 \cdot 10^4$. Fig. 5.7 (b) shows the conversion section associated to the interface with incoming currents from both sides. The green stars in Fig. 5.7 (b) are the phase space coordinates in the PSSD of the first twenty-two crossings of the trajectory with the interface and the blue star is the last intersection before the ballistic flight across the block starts. Apparently, all green stars lie in the black area. Accordingly, the particle maintains its chaotic behavior because it is always injected into the chaotic sea. Therefore, it is several times transported back to the interface due to the convergent flux until its position in phase space overlaps with regular structure of the adjacent block (blue star in the white are in Fig. 5.7 (b)). By looking at the PSSD of the domain with positive directed transport (Fig. 5.4 (b)) we see that this injection occurs obviously into the regular part of phase space beyond the FISC, i.e. the particle is now trapped on a regular curve and traverses the block ballistically (compare blue curve in Fig. 5.3 for $1.5 \cdot 10^4 < t < 3 \cdot 10^4$) until it reaches the subsequent interface with divergent flux (outgoing currents). In Fig. 5.7 (c) we show the corresponding magnification of the trajectory for the period of time during which the particle remains close to the interface of the neighboring domains. In Fig. 5.7 (d) the associated conversion section together with the phase space coordinates of the crossings of the trajectory with the interface is presented. The blue star is the first intersection and the green stars are the subsequent ones. Obviously, the blue star lies in a red area, i.e. after being injected from the chaotic sea into regular structure at the previous interface with convergent flux the particle experiences now a crossover from ballistic back to diffusive motion. In the trajectory (Fig. 5.7 (c)) this behavior can be seen as the almost abrupt end of the ballistic flight at the interface. Afterwards the particle crosses several times the interface and its coordinates in phase space at the intersections fall always

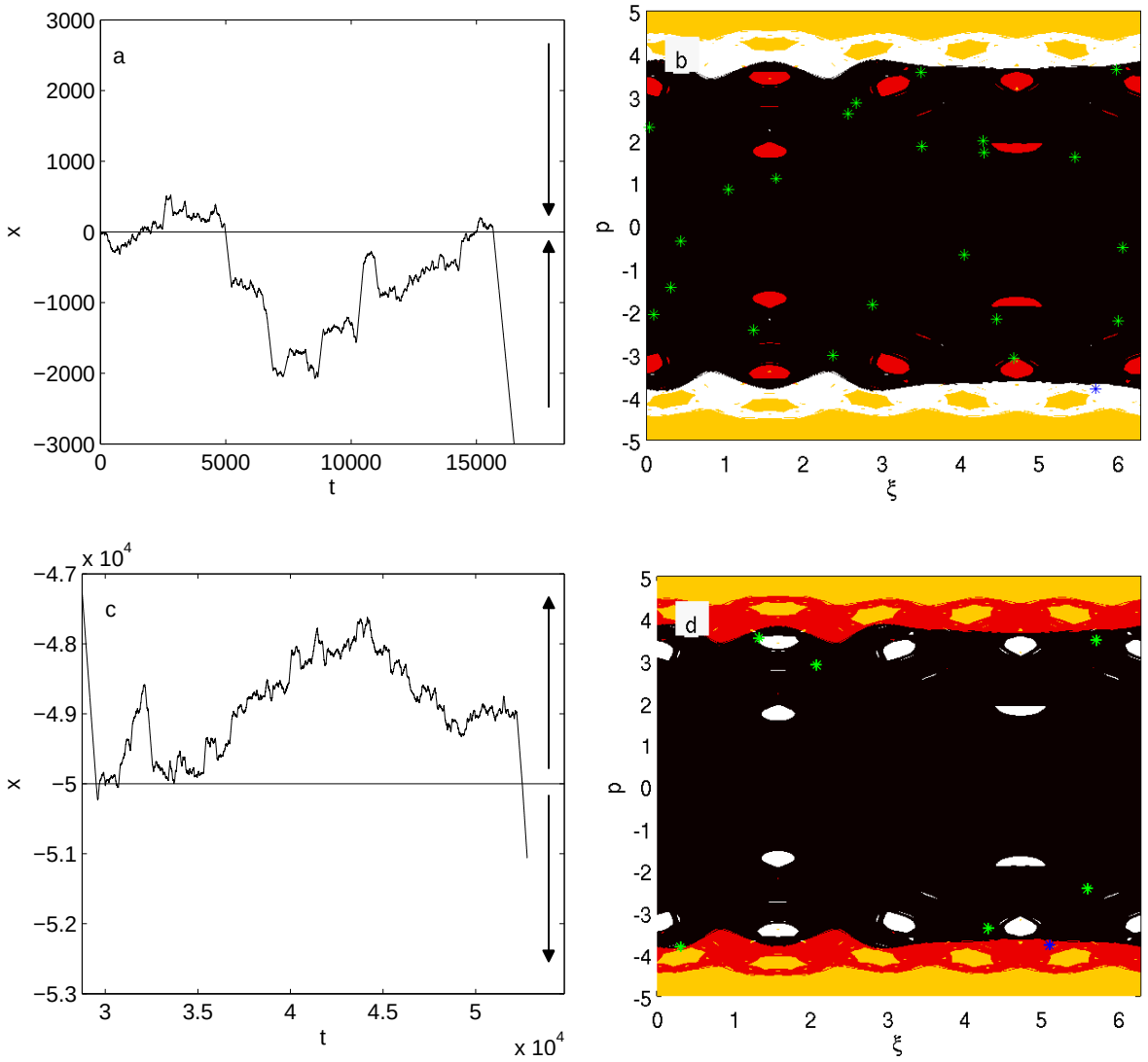

Figure 5.7: (a) shows a diffusive trajectory which remains close to an interface with incoming current and experiences multiple crossovers until it becomes ballistic at $t \approx 1.5 \cdot 10^4$. (b) shows the corresponding "conversion section" together with phase space coordinates marked as colored symbols when the trajectory crosses the interface. (c) shows the extract of the trajectory when it arrives at the next interface with outgoing currents. (d) shows the "conversion section" and the phase space coordinates.

into the chaotic sea of the adjacent block. Consequently, the particle's dynamics remains diffusively which can be observed in the trajectory for $t \approx 3 \cdot 10^4 - 5.3 \cdot 10^4$ (Fig. 5.7 (c)). Especially, the position in phase space of the trajectory at the last crossing with the interface occurring at $t \approx 5.3 \cdot 10^4$ coincides with the chaotic sea of the adjacent block. Yet, this time the injection into the block is deeper than before because the particle has a comparatively high negative velocity as Fig. 5.7 (c) reveals. Afterwards, the particle moves diffusively until it reaches the subsequent interface where a conversion back to ballistic dynamics occurs (blue curve, $t \approx 2.3 \cdot 10^5$, $x = -1 \cdot 10^5$ in Fig. 5.3). For the present trajectory (blue curve in Fig. 5.3) this alternating phases of ballistic and diffusive motion on the scale of one block continues until we have stopped the simulation at $t = 10^6$.

Nevertheless, it can also occur that a particle traverses several blocks ballistically without changing its dynamical state when crossing an interface as the trajectories shown in Fig. 5.3 reveal. To understand such a behavior let us analyze the dynamics of the particle starting at $x \approx -3 \cdot 10^5$ (black curve in Fig. 5.3) in more detail. To this end we focus on the time period during which the trajectory traverses ballistically five blocks after it has been injected at an interface with convergent flux ($t \approx 3.3 \cdot 10^5$, $x = -2 \cdot 10^5$ in Fig. 5.3) from the chaotic sea into the regular structure of the phase space of the adjacent domain. The ballistic flight ends at an interface with outgoing currents ($t \approx 3.9 \cdot 10^5$, $x = 0.5 \cdot 10^5$ in Fig. 5.3) where a conversion back to the chaotic sea occurs. Fig. 5.8 shows the sequence of the conversion sections together with the coordinate in phase space (blue stars) of the trajectory when it crosses the interface at $x = -2 \cdot 10^5$ (a), $x = -1.5 \cdot 10^5$ (b) etc. Fig. 5.8 (a) reveals that the ballistic flight is initialized by a conversion process of the particle from the chaotic sea into the part of the phase space beyond the FISC. In fact, from the corresponding PSSD shown in Fig. 5.4 (a) we can conclude that the trajectory is injected into the chaotic layer surrounding the chain of elliptic islands above the FISC. In the course of the following ballistic flight across the block the orbit in the PSSD fills uniformly this layer until the particle arrives at the next interface with divergent flux. At this position the trajectory does not experience a conversion back to the diffusive dynamics as Fig. 5.8 (b) reveals. Instead, by comparing Fig. 5.8 (b) and Fig. 5.4 (b) we see that its position in phase space coincides with the elliptic island in the PSSD at $\xi \approx 0.3$, $p \approx 4.1$ belonging to the chain of five islands embedded in the chaotic layer. Consequently, the particle maintains its ballistic behavior. According to Fig. 5.8 (c)-(e) the trajectory remains in this dynamical state for three more crossings. By comparing the Fig. 5.8 (c)-(e) with the appropriate PSSDS we see that the process of alternating injection into elliptic islands and the chaotic layer above the FISC repeats at each interface until the particle arrives at $x = 0.5 \cdot 10^5$. At this interface with outgoing local currents the ballistic flight ends because a conversion in the particle's dynamical state occurs (see Fig. 5.8 (f)). Obviously, the position in phase space of the trajectory coincides with the chaotic sea corresponding to diffusive motion in the adjacent block.

Let us finally investigate more closely the dynamics of the particle starting at $x \approx 2 \cdot 10^5$ (red curve in Fig. 5.3). Specifically, we discuss in the following the period of time during which it traverses ballistically the same block three times ($7 \cdot 10^5 < t < 7.5 \cdot 10^5$ in Fig. 5.3). Although at first glance it seems as if the trajectory is immediately reflected at the position of the interface, a magnification reveals that the particle first crosses the interface and experiences a conversion from ballistic to diffusive dynamics. It enters however the adjacent domain only insignificant and visits the interface again. Evidently, at this second intersection the trajectory is injected into a phase space structure of the subsequent block leading to ballistic dynamics.

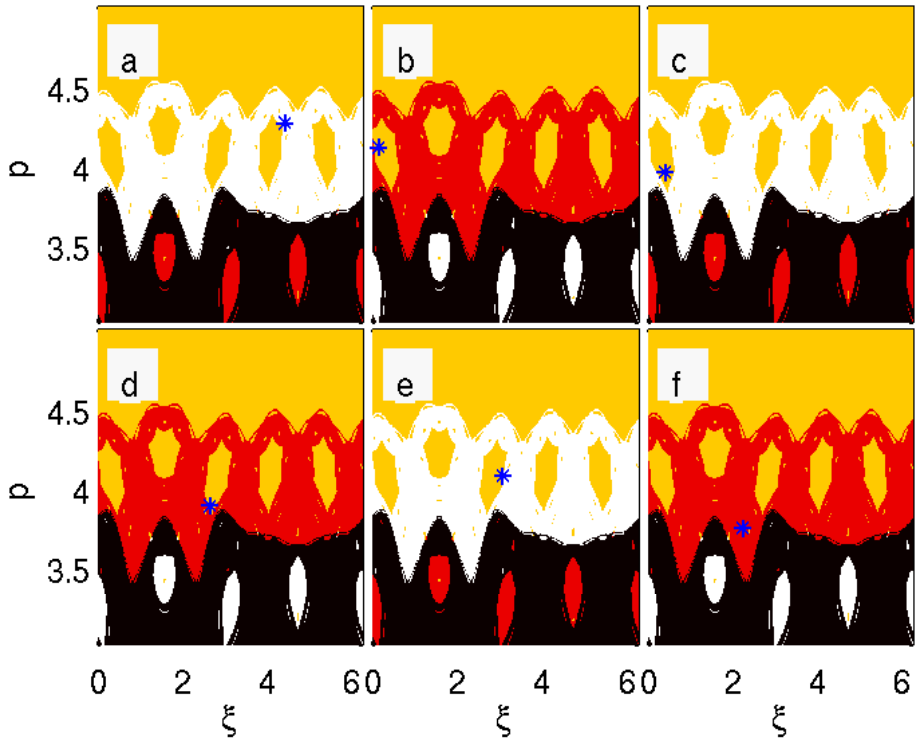

Figure 5.8: Sequence of the conversion sections together with the coordinate in phase space (blue stars) of the trajectory started at $x \approx -3 \cdot 10^5$ when it traverses ballistically five blocks and crosses the interface at $x = -2 \cdot 10^5$ (a), $x = -1.5 \cdot 10^5$ (b), $x = -1.0 \cdot 10^5$ (c), etc.

Thus, the particle traverses the domain opposite to the direction of the previous ballistic flight until it arrives at the next interface where the just described process recurs. In other words a ballistic particle has to experience a conversion to diffusive dynamics beforehand in order to traverse the same block again ballistically because the phase structures for a ballistic flight in positive and negative direction have no overlap.

In this vein the dynamics of other trajectories can be analyzed, too. In a nutshell we can say that the dynamics of a particle in a block can be predicted by its coordinate in phase space when it crosses the corresponding interface. We have discussed moreover that the trajectories exhibit typically conversion processes between ballistic and diffusive motion. By analyzing the Poincaré surface of section of the domains (PSSD) these processes have been traced back to the overlap of the different phase space structures at an interface leading to ballistic or diffusive dynamics, i.e. when a trajectory is injected from a domain with driving law $g(t)$ into a domain with $-g(t)$ it can experience a crossover in its dynamical state. With this knowledge at hand we have explained the characteristic alternating phases during which the particles traverse either ballistically a block or move chaotically according to local transport. In the following we will study how this behavior leaves its hallmarks in the dynamical evolution of the spatial distribution of an ensemble of particles.

5.4 Particle density modulations

In this section we discuss the dynamics of an ensemble of 10^6 particles which are initially uniformly distributed in the lattice occupying 20 domains centered around the origin and homogeneously fill the chaotic sea at low velocities $|v| \leq 0.1$. The spatiotemporal evolution of the particle density profile (see Fig. 5.9) shows, due to the diffusion of the chaotic trajectories, a significant spatial broadening. More importantly, we observe the emergence of a periodic, stripe-like modulation of the density, i.e. for a fixed time the spatial distribution of the particles has alternating flat maxima and minima corresponding to the length of one domain. This behavior persists until $t \approx 5 \cdot 10^6$ and gradually disappears thereafter. Let us analyze this in some more detail.

For $t = 10^4$ (Fig. 5.9 (a)) the envelope behavior of $\rho(x)$ is still similar to the initial distribution $\rho_0(x)$ but there occur sharp dips at the positions of the interfaces. The magnification reveals that the dips are significantly more pronounced at the interfaces with outgoing flux (Fig. 5.9 (b)). At $t = 10^6$ (Fig. 5.9 (c)) the envelope of $\rho(x)$ has broadened and the density modulations are much more pronounced extending over an entire domain of the lattice (Fig. 5.9 (c)). For $x > 0$ $\rho(x)$ possesses plateau-like maxima in domains with $v_\mathrm{T} > 0$ and corresponding minima in domains with $v_\mathrm{T} < 0$ and vice versa for $x < 0$. With the knowledge on the single particle dynamics which we have acquired in the previous section this behavior is elucidated in the next paragraph.

Let us start with the discussion of the evolution of $\rho(x)$ for short times $t \leq 10^4$. In the beginning ($t = 10^4$) we observe a sharp depletion of the particle density at the positions of the interfaces (Fig. 5.9 (a) and (b)) which is explained in the following. Since the initial velocities of the trajectories are small, the ensemble is localized in the chaotic sea of phase space, i.e. the particles obey diffusive dynamics. According to the discussion in the previous section it is possible that a ballistic flight starts at an interface every time a diffusive trajectory crosses this position. According to the previous section such an event occurs when the particle's coordinate in phase space at the point in time when it crosses the interface coincides with e.g. an elliptic island in the phase space of the adjacent block. In Fig. 5.10 the number ballistic flights starting at position x_start ($n(x_\mathrm{start})$) where the particle traverses more than 10^3 barrier without reversing the sign of its velocity is shown. Evidently, we find narrow peaks localized at the interfaces, i.e. many ballistic flights start at the positions of the interfaces between the differently driven domains. Furthermore, we observe that the number of ballistic flights starting at an interface with convergent flux ($x = 0, \pm 1 \cdot 10^5, \pm 2 \cdot 10^5$ in Fig. 5.10) is higher than at an interface with divergent flux ($x = \pm 0.5 \cdot 10^5, \pm 1.5 \cdot 10^5$ in Fig. 5.10). This surprising behavior is due to the fact that at an interface with incoming currents crossings of diffusive particles occur more frequently. Apparently, this process of ballistic flight production leads to a fast local reduction of the spatial particle distribution $\rho(x)$ at the positions of the interfaces since compared to diffusive trajectories, the ballistic particles travel with a high velocity away from the interface. However, if the local currents are incoming this effect competes with the accumulation of particles obeying chaotic dynamics. Therefore, the dip is more pronounced for interfaces with outgoing local currents.

Let us now develop an understanding of the longer-time transient behavior leading to the plateau-like density modulations (Fig. 5.10 (c) and (d)). For reasons of brevity interfaces with incoming / outgoing flux are called interface I / II in the following. The initial ensemble is localized in the chaotic sea of the phase space of the lattice. In every domain the chaotic

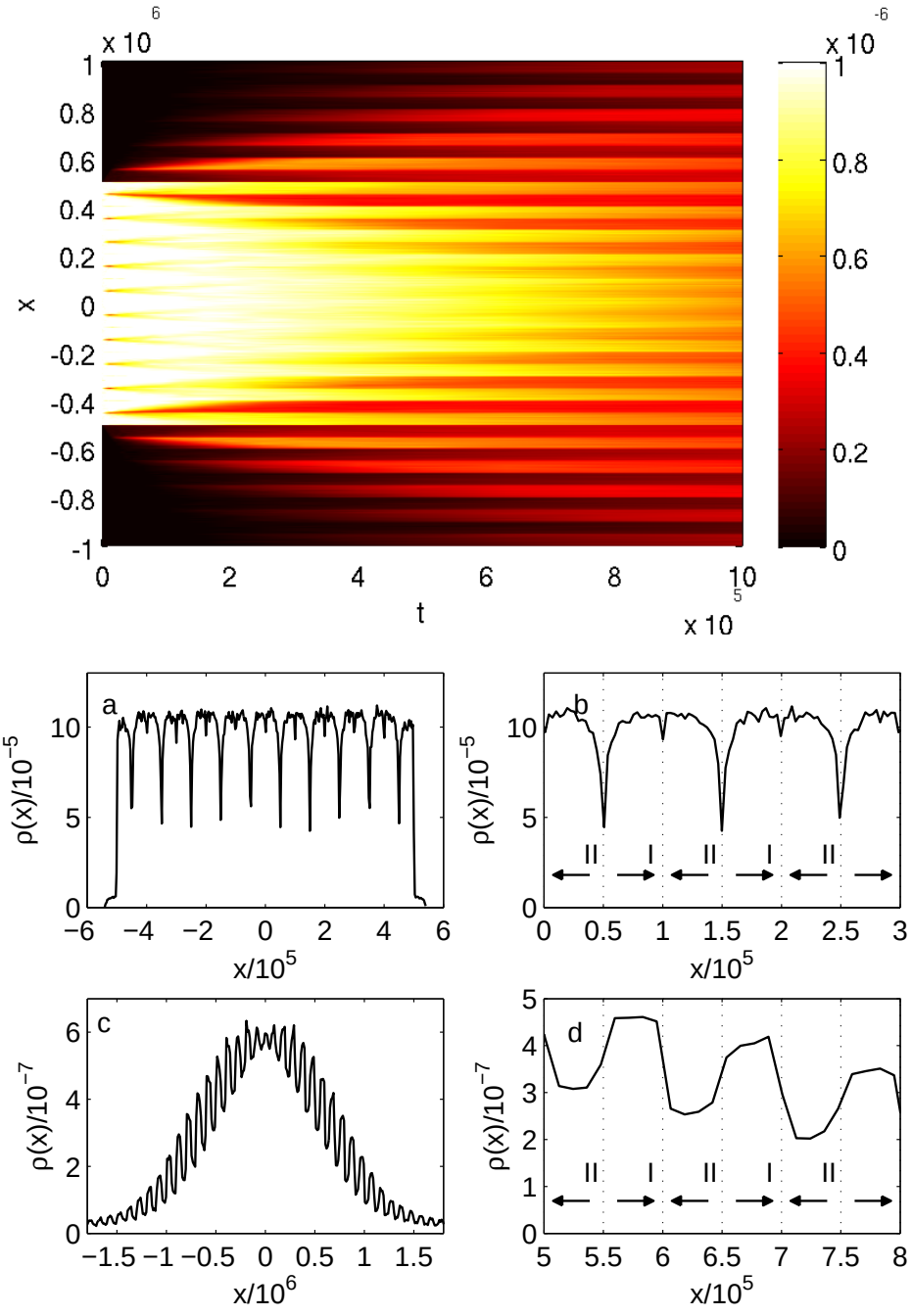

Figure 5.9: In the upper figure a color plot of the particle density $\rho(x,t)$ is shown. The initial ensemble is distributed according to $\rho(x,t=0) = 10^{-6} \cdot \Theta(10^5 L - |x|)$ and $\rho(v,t=0) = 5 \cdot \Theta(0.1 - |v|)$ ($V_0 = 2.2$). For $t \gtrsim 10^5$ a periodic modulation of the spatial distribution of the particles in the lattice is clearly visible. (a) and (c) show the spatial distribution of the particles $\rho(x)$ for $t = 10^4$ (a) and $t = 10^6$ (c). (b) and (d) are magnifications of (a) and (c) respectively. The arrows in the magnifications indicate the direction of the local current in the domain.

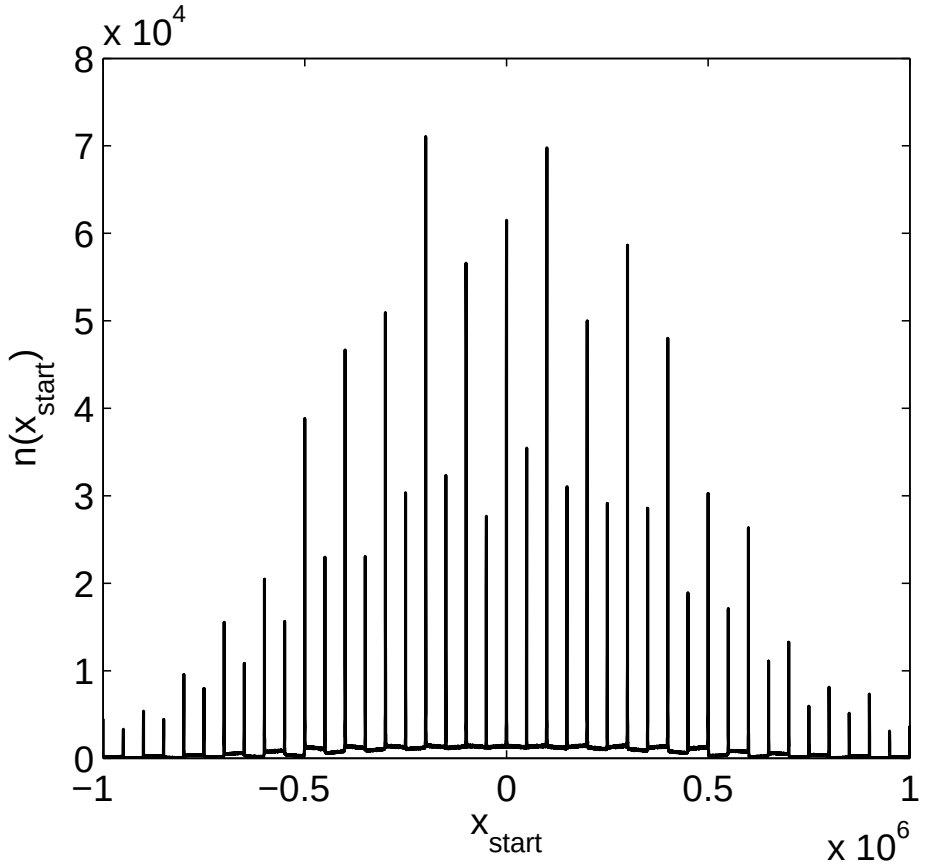

Figure 5.10: Distribution of number of ballistic flight starting at the positions x_{start} in the blockstructured lattice.

trajectories experience the corresponding drift velocity and accumulate at the interfaces I with incoming directed currents. Even if a 'deeper' reinjection from the interface into an adjacent domain again occurs (which is a rare event) it will return to this interface at a somewhat later point in time. Hence, chaotic trajectories are transported several times back to the interface until a conversion from chaotic to ballistic dynamics occurs. Accordingly, diffusive particles are localized in a small spatial region around these interfaces I until a conversion into regular ballistic motion takes place. When such a ballistic particle reaches the next interface II (outgoing directed currents) the trajectory can either remain ballistic and traverse the subsequent domain in a comparatively short time or the particle is injected from the ballistic island back into the chaotic sea. It is however important to keep track of the fact that the ballistic trajectories cross the interface II and typically enter $10^2 - 10^3$ unit cells into the next domain before they acquire a diffusive character. More precisely, the particles are injected into the chaotic sea at the interface, yet their velocity is large enough so that the trajectories traverse several barriers before the diffusive character of the dynamics becomes evident. In the latter domain the particles experience a drift to the adjacent interface I, since the local current points away from the interface II. Obviously, this process does not occur at the interface I with exclusively incoming currents. Note that domains with left pointing

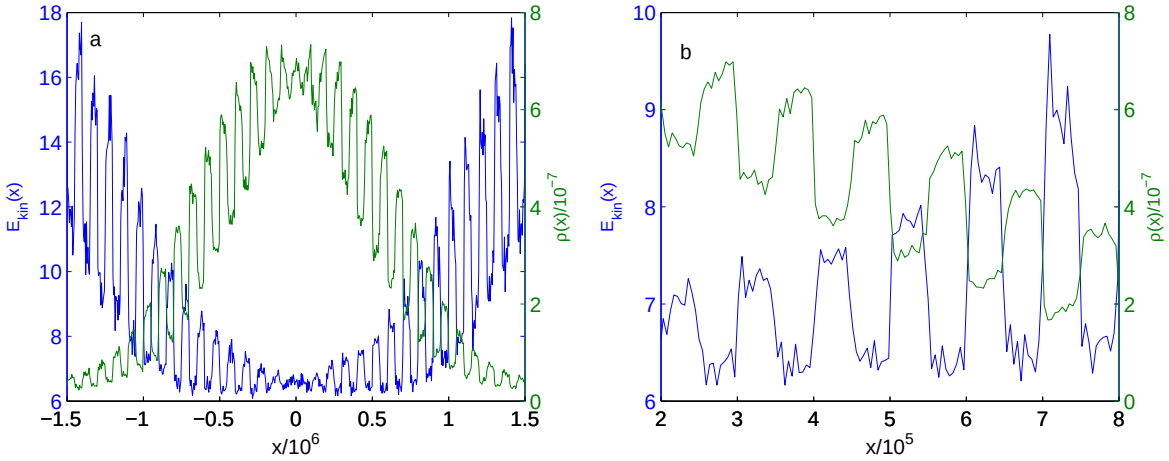

Figure 5.11: (a) shows the spatial particle distribution $\rho(x)$ at $t = 10^6$ together with the spatial distribution of the mean kinetic energy $E_{\mathrm{kin}}(x)$. (b) is a magnification of (a).

current can be traversed to the right only by ballistic trajectories. As a result an enhanced number of diffusive trajectories occurs in domains with right pointing current for $x > 0$ and vice versa. Since the dwell time of chaotic trajectories in a domain is approximately one order of magnitude larger than the dwell time of ballistically travelling particles due to their lower average velocity this results in a periodic modulation of $\rho(x)$. It is crucial to note that the Hamiltonian itself does not reflect such an asymmetry with respect to the domains with left and right-pointing currents corresponding to driving laws $g(t)$ and $-g(t)$ respectively. Indeed, the asymptotic steady state of the time-evolved ensemble ($t \gg 10^7$) possesses a uniform density.

5.4.1 Distribution of kinetic energy and dwell times

By considering the spatial distribution of the kinetic energy we can substantiate further the argument that the periodic modulations of $\rho(x)$ are due to the inhomogeneous distribution of particles obeying diffusive dynamics. For this purpose we show in Fig. 5.11 the spatial distribution of the kinetic energy $E_{\mathrm{kin}}(x)$ together with $\rho(x)$ for $t = 10^6$. Fig. 5.11 (a) reveals that the particles in the tail of the spatial distribution $\rho(x)$ have higher kinetic energies compared to the trajectories in the center of $\rho(x)$ which can be explained straightforwardly: for a fixed time the particles which have travelled the longest distance away from their starting position must have been for the most time in the portion of phase space with high momentum, e.g. trajectories experiencing long ballistic flights. Therefore, it is intuitively clear why $E_{\mathrm{kin}}(x)$ has an envelope which increases with x. Fig. 5.11 (a) shows additionally that $E_{\mathrm{kin}}(x)$ possesses the same periodic modulations on the scale of one block as the spatial particle distribution $\rho(x)$, i.e. the kinetic energy of the particles within a domain is approximately constant and alternates between a local maximum and minimum respectively. In the magnification of Fig. 5.11 (a) shown in Fig. 5.11 (b) we see that the spatial distribution of the kinetic energy $E_{\mathrm{kin}}(x)$ possesses a local maximum where $\rho(x)$ has a local minimum and vice versa. Since the kinetic energy of a diffusively travelling particle is on average small compared to a particle

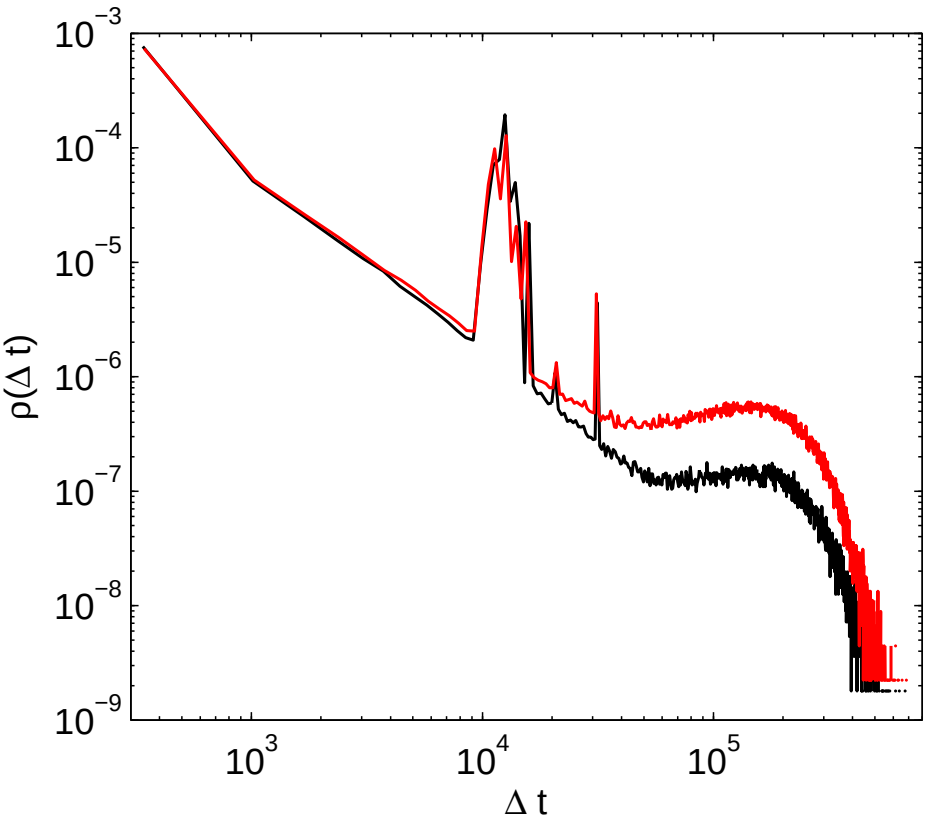

Figure 5.12: The black curve is the probability distribution of dwell-times of trajectories $\rho(\Delta t)$ for the block extending from $x = 5 \cdot 10^5$ to $x = 5.5 \cdot 10^5$ which is a domain with a local minimum of the particle density $\rho(x)$. The red curve shows $\rho(\Delta t)$ for the adjacent block ($x = 5.5 \cdot 10^5$ to $x = 6 \cdot 10^5$) which possesses a local maximum of $\rho(x)$.

obeying ballistic dynamics, this finding confirms indeed that in a block where the spatial particle distribution has a local maximum an increased number of diffusive trajectories is present.

Finally, let us discuss the behavior of the dwell-time in a domain of trajectories Δt for the simulation corresponding to Fig. 5.9, that is we examine how long particles which cross an interface remain in the block before leaving it again. Fig. 5.12 shows the probability distribution of dwell-times of particles $\rho(\Delta t)$ for two different spatial regions. The black curve belongs to the block extending from $x = 5 \cdot 10^5$ to $x = 5.5 \cdot 10^5$ where the particle distribution $\rho(x)$ possesses a local minimum. The red curve corresponds to the domain with a local maximum of $\rho(x)$ ($x = 5.5 \cdot 10^5$ to $x = 6 \cdot 10^5$). Both curves are apparently almost identical for $t \leq 10^4$. Such events of comparatively short dwell-times are for example due to diffusive trajectories which remain close to an interface and cross it repeatedly (see Fig. 5.7 (a) and (c)). For $t \geq 10^4$ the curves deviate from each other whereas $\rho(\Delta t)$ belonging to the block with a local maximum of $\rho(x)$ lies systematically above the curve corresponding to the domain with a local minimum of the particle density. At $10^4 \leq t \leq 1.6 \cdot 10^4$, $t \approx 2.2 \cdot 10^4$ and $t \approx 3 \cdot 10^4$ are pronounced peaks in $\rho(\Delta t)$ which can be associated to particles traversing ballistically the block. In order to verify this statement we have determined the phase ξ and

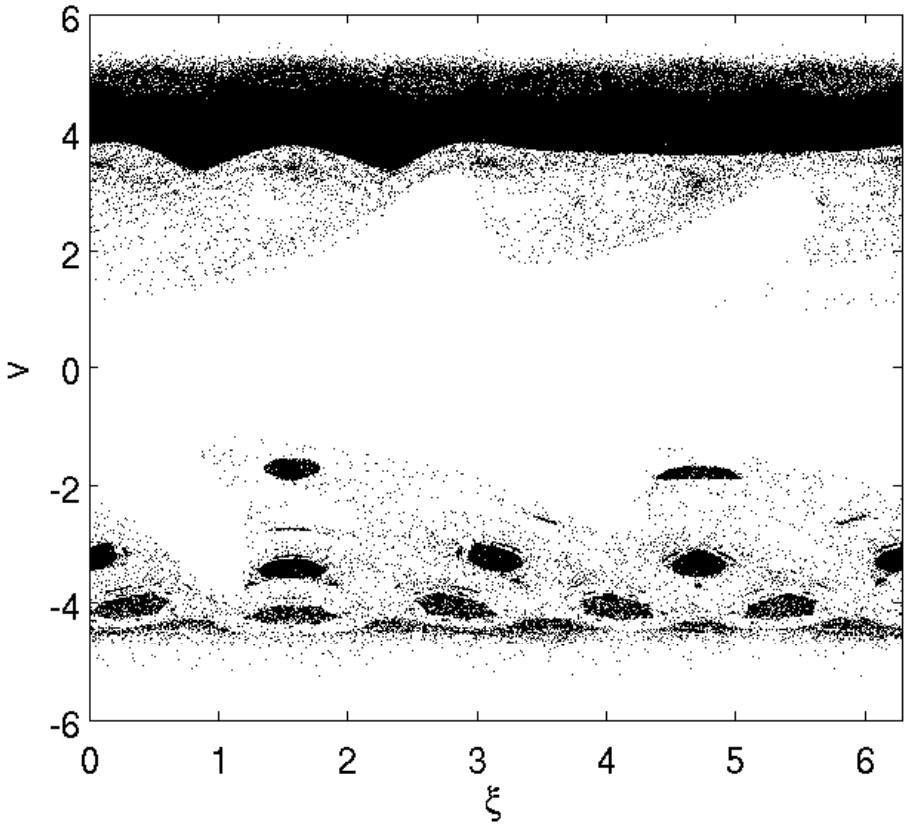

Figure 5.13: Scatter plot of the phase space coordinates ξ, v of trajectories belonging to the peaks in the black curve in Fig. 5.12 when the corresponding particles enter the block by crossing the interface at $x = 5 \cdot 10^5$ or $x = 5.5 \cdot 10^5$.

the velocity v of trajectories corresponding to these peaks when they enter the block. In Fig. 5.13 the phase space coordinates ξ, v are shown for particles belonging to the pronounced peaks of the black curve in Fig. 5.12. Evidently, the points in Fig. 5.13 with positive / negative velocity are the trajectories which have entered the domain by crossing the interface at $x = 5{\cdot}10^5$ / $x = 5.5{\cdot}10^5$. By comparing Fig. 5.13 with Fig. 5.4 (a) which depicts the PSSD for the block with negative transport velocity we observe a strong accumulation of particles in the parts of the phase space which correspond to trajectories traversing the block ballistically. For example the points in Fig. 5.13 with positive velocity are mostly scattered in a region of the PSSD beyond the FISC, whereas the points with negative velocity are predominantly found in elliptic islands. Consequently, the peaks in the distributions of dwell-times shown in Fig. 5.12 can be indeed attributed to trajectories traversing ballistically the blocks. For even longer dwell-times $t \geq 5 \cdot 10^5$ (see Fig. 5.12 both curves possess a broadened maximum at $t \approx 1.9 \cdot 10^5$ which is due to particles crossing diffusively the domains. In Sec. 5.2 we have determined the transport velocity of the block as $v_{\mathrm{T}} = -0.2649$. Accordingly, the time a diffusive particle needs on average to traverse diffusively the block is

$$\Delta t_{\mathrm{D}} = \frac{L_B}{v_{\mathrm{T}}} = \frac{N \cdot L}{v_{\mathrm{T}}}, \tag{5.3}$$

where $L = N \cdot L$ is the domain's length. Inserting the parameters' values, i.e. $N = 10^4$, $D = 5$ and $v_{\mathrm{T}} = -0.2649$ we find $\Delta t_{\mathrm{D}} \approx 1.89 \cdot 10^5$ which coincides well with the maxima of the distributions $\rho(\Delta t)$. Of course not all diffusive trajectories need exactly this time to traverse the block because the dynamics is intermittent, i.e. the diffusive motion is interrupted by ballistic flights. If such a ballistic flight has the same direction as the local current, then this particle will cross the domain in shorter time than Δt_{D} and vice versa. In this range of the dwell-times the red curve is systematically above the black curve which implies again that there are more diffusive particles in a block with a local maximum of $\rho(x)$. Although we have chosen two specific blocks to analyze the dwell-times $\rho(\Delta t)$, the qualitative behavior is identical for the other domains, i.e. $\rho(\Delta t)$ for a block with a local maximum of $\rho(x)$ exceeds systematically $\rho(\Delta t)$ associated to a domain with a local minimum of $\rho(x)$ in the range of dwell-times corresponding to diffusive particles. Nevertheless, it is important to note that the behavior shown in Fig. 5.13 is not stationary but only valid until we have stopped the simulation at $t = 10^6$. In fact, the differences of the dwell-times becomes less subsequently and in the limit $t \to \infty$ the curves coincide. Evidently, this behavior can be associated to the asymptotic limit when the periodic modulations of the particle density are smoothed out due to the symmetry properties of the whole lattice. Since the Hamiltonian is invariant under the transformation given by equation (5.2) the system shows for $t \to \infty$ a super-diffusive broadening of the particle distribution similarly to a uniformly, monochromatically driven lattice. Consequently, in this asymptotic limit the periodic modulations of $\rho(x)$ are gone and the transient differences in the dwell-times must disappear, too.

5.4.2 Role of the initial ensemble

In order to verify that the density modulations are not an artifact of the initial conditions we have chosen other ensembles, too. In the upper part of Fig. 5.14 the evolution of the spatial particle density distribution $\rho(x)$ as a color-plot is shown for an ensemble of particles which have initially small velocities, i.e. $|v_0| \leq 0.1$ and start close to the origin of the lattice $|x_0| \leq 0.1$. All parameters of the lattice are unchanged as before ($V_0 = 2.2$, $L = 5$). Obviously, $\rho(x)$ gets smeared out due to diffusion such that more domains are sequently populated. In the course of the dynamics the periodic modulation on the scale of one block of the particle distribution develops, i.e. the density has alternately a local maximum or minimum. Similarly as before these modulations of the particle density are only a transient phenomenon but they prevail temporally in the same range $10^5 \leq t \leq 5 \cdot 10^6$. Consequently, the appearance of this phenomenon is independent from the initial ensemble. Still, on shorter time-scales the spatial particle distribution $\rho(x)$ obeys a different behavior depending on the initial ensemble. Fig. 5.14 (a) shows $\rho(x)$ for $t = 10^4$ with three pronounced peaks at $x \approx -3.5 \cdot 10^4$, $x \approx 0$ and $x \approx 3.5 \cdot 10^4$. Obviously, $\rho(x)$ is symmetric with respect to the origin which is due to the fact that we have chosen the initial ensemble symmetrically in phase space. Since the particles start at an interface with convergent flux, it is a very unlikely event that a diffusive trajectory traverses one of the adjacent blocks. Instead, the diffusive particles remain localized close to the origin of the lattice which explains the peak at $x = 0$, i.e. these are chaotic trajectories which get transported continuously back to the interface. Due to the fact that the particle density is very large in the beginning at $x \approx 0$, the rate with which diffusive particles are injected into regions of the phase of the neighboring blocks corresponding to ballistic dynamics is high, too. Consequently, many particles experience

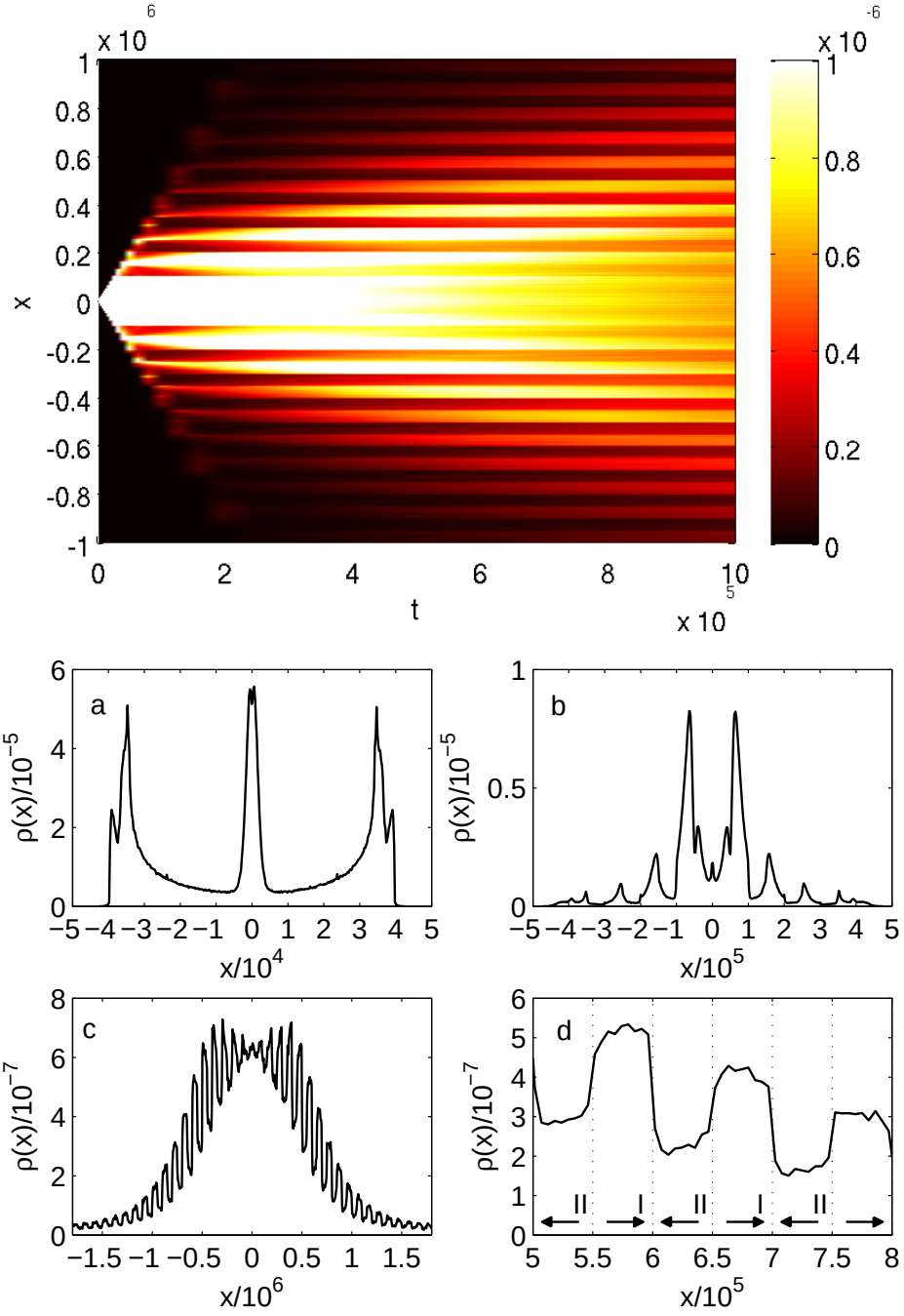

Figure 5.14: In the upper figure a color plot of the particle density $\rho(x,t)$ is shown. The initial ensemble is distributed such that the particles start in the chaotic sea of the phase space $|v_0| \leq 0.1$ and close to the origin of the lattice $|x_0| \leq 0.1$ ($V_0 = 2.2$). For $t \gtrsim 10^5$ the periodic modulation of the spatial distribution of the particles on the scale of one block is again visible. (a), (b) and (c) show the spatial distribution of the particles $\rho(x)$ for $t = 10^4$ (a), $t = 10^5$ and $t = 10^6$ (c) respectively. (d) is a magnifications of (c). The arrows in the magnification indicate the direction of the local current in the domain.

crossovers from diffusive to ballistic motion during the first few periods of the driving which is the origin of the peaks at $x \approx \pm 3.5 \cdot 10^4$. Afterwards, the conversion rate decreases rapidly with time and therefore the spatial distribution of particles drops, i.e. not only the trajectories in the peaks of $\rho(x)$ at $x \approx \pm 3.5 \cdot 10^4$ are predominantly ballistic but also the particles in the range between them $0 \leq |x| \leq 3.5 \cdot 10^4$. Figure (b) shows $\rho(x)$ for $t = 10^5$. Obviously, the distribution has broadened further and the first indications of the periodic modulations of the spatial particle distribution $\rho(x)$ on the scale of one block are already visible. Still, the local maxima and minima are not completely defined, i.e. $\rho(x)$ is not yet constant within one block. For $t = \cdot 10^6$ this behavior has completely developed as figure (c) reveals. The spatial particle distribution $\rho(x)$ possesses alternately local maxima and minima on the scale of one block which can be seen in the corresponding magnification shown in figure (d). Furthermore, a comparison of Fig. 5.14 (d) with Fig. 5.9 (d) shows that the extrema are in the same blocks, i.e. for $x > 0$ the maxima / minima are in the block with positive / negative transport velocity and vice versa for $x < 0$. Accordingly, the appearance of the density modulation is independent from the choice of the initial conditions. Since we have considered two "extreme" cases, that is a broad, uniform and a very narrow initial distribution, it is reasonable that for other ensemble which are distributed in space according to e.g. a Gaussian the periodic modulation will occur, too.

5.5 Markov Chain Model

In this section we show that the mechanism leading to the periodic density modulations can be understood qualitatively by a Markov chain which represents an "interface mapping" comprising the dynamics within a domain. Components of the Markov state $\mathcal{X}$ are the dynamical character of a trajectory denoted by $\gamma = \{\mathrm{d}, \mathrm{b}\}$ ($\mathrm{d} \mathrel{\widehat{=}}$ diffusive / $\mathrm{b} \mathrel{\widehat{=}}$ ballistic), the direction of motion $\delta = \{\mathrm{l}, \mathrm{r}\}$ ($\mathrm{l} \mathrel{\widehat{=}}$ left / $\mathrm{r} \mathrel{\widehat{=}}$ right), the position of the particle x and the point in time t it reaches the current interface, i.e.

$$\mathcal{X}_n = \begin{pmatrix} \gamma_n \\ \delta_n \\ x_n \\ t_n \end{pmatrix}, \tag{5.4}$$

where n symbolizes the n-th step of the chain. The conditional transition probabilities p_{ij} of a dynamical conversion at an interface, which constitute the transition matrices can be obtained by calculating the overlap of the different regular and chaotic structures in phase space and augmenting it by local characteristics of the different interfaces. To this end we simulate the dynamics of an ensemble which is initialized close to the origin of the lattice. For each particle the phase ξ and the velocity v is recorded every time when the corresponding trajectory crosses an interface. In this way we get two sets of datapoints $\mathcal{C} = \{(\xi_1, v_1), \ldots, (\xi_n, v_n)\}$ and $\mathcal{C}' = \{(\xi'_1, v'_1), \ldots, (\xi'_n, v'_n)\}$, whereas $\mathcal{C}$ / $\mathcal{C}'$ contains the trajectories' intersections for the interfaces with convergent / divergent flux. In order to calculate for example the probability for a crossover from diffusive to ballistic dynamics p_{db} the following steps have to taken. First, we have to determine the number of datapoints corresponding to the conversion processes from diffusive to ballistic dynamics N_{db}. Additionally, we need the number of datapoints where the trajectory remains diffusive after crossing the interface (diffusive to diffusive) N_{dd}. To

	p_{db}	p_{dd}	p_{bd}	p_{bb}
convergent flux	0.18	0.82	0.16	0.84
divergent flux	0.06	0.94	0.51	0.49

Table 5.1: Conditional conversion probabilities for the interface with convergent and divergent flux.

obtain N_{db} and N_{dd} we exploit the conversion sections. From the discussion in Sec. 5.3.2 it is known that the white / black area in the conversion sections shown in Fig. 5.6 (a) and (b) stand for injection processes from diffusive to ballistic / diffusive to diffusive dynamics. Consequently, the numbers N_{db} and N_{dd} can be determined by counting the datapoints which fall in the white and black area respectively. Altogether the probability p_{db} is then given by

$$p_{\mathrm{db}} = \frac{N_{\mathrm{db}}}{N_{\mathrm{db}} + N_{\mathrm{dd}}}. \tag{5.5}$$

Analog, the probability for a diffusive particle to remain in its dynamical state p_{dd} is derived by

$$p_{\mathrm{dd}} = \frac{N_{\mathrm{dd}}}{N_{\mathrm{db}} + N_{\mathrm{dd}}}. \tag{5.6}$$

We can proceed similarly for the other conditional conversion probabilities. Since the red / yellow area in the conversion sections shown in Figs. 5.6 (a) and (b) stands for ballistic to diffusive / ballistic to ballistic injection processes, the number N_{bd} and N_{bb} are obtained by counting the datapoints which lie in the corresponding regions. Finally, the probabilities are calculated via

$$p_{\mathrm{db}} = \frac{N_{\mathrm{bd}}}{N_{\mathrm{bd}} + N_{\mathrm{bb}}}, \tag{5.7}$$

$$p_{\mathrm{db}} = \frac{N_{\mathrm{bb}}}{N_{\mathrm{bd}} + N_{\mathrm{bb}}} \tag{5.8}$$

Due to the fact that the respective areas in the conversion section shown in Fig. 5.6 (a) and (b) are not identical, the conditional conversion probabilities are different for the interface with convergent and divergent flux, too. In Table 5.1 the results of evaluating equations (5.5)-(5.8) by means of Figs. 5.6 (a) and (b) is shown. Obviously, the probabilities fulfill the normalization condition

$$p_{\mathrm{db}} + p_{\mathrm{dd}} = 1, \tag{5.9}$$

$$p_{\mathrm{bd}} + p_{\mathrm{bb}} = 1. \tag{5.10}$$

Furthermore, we want to draw attention to the following facts. At an interface with convergent flux the probability for a diffusive particle to experience a dynamical conversion to ballistic dynamics p_{db} is three times larger compared to an interface with outgoing currents (see Table 5.1). Evidently, this is a reasonable result because according to the discussion in Sec. 5.3.2 the overlap of the chaotic sea with the parts of phase space associated to ballistic motion is larger when the blocks are concatenated such that the currents are incoming at the interface (white area in Fig. 5.6 (a) is larger than in (b)). Conversely, we find for the interface with divergent flux that the conditional probability for a crossover of a trajectory from ballistic

to diffusive dynamics p_{bd} is approximately three times larger which can be also attributed to the overlap properties, i.e. at such an interface a larger area of the PSSD associated to ballistic dynamics is projected onto the chaotic sea.

Let us now describe the procedure how the state $\mathcal{X}_n$ is iterated. It is most convenient to introduce a mapping $\mathcal{T}$ from the state $\mathcal{X}_n$ to $\mathcal{X}_{n+1}$, i.e.

$$\mathcal{X}_{n+1} = \mathcal{T}\mathcal{X}_n, \tag{5.11}$$

where $\mathcal{X}_{n+1} = (\gamma_{n+1}, \delta_{n+1}, x_{n+1}, t_{n+1})^t$ is derived according to the following procedure. After the crossing of an interface the dynamical state of the trajectory γ_{n+1} is evidently related through the conditional conversion probabilities to its previous dynamical state γ_n such that γ_{n+1} is given by the relations

$$P(\gamma_{n+1} = b) = \begin{cases} p_{\mathrm{bb}} & \text{if } \gamma_n = \mathrm{b} \\ p_{\mathrm{db}} & \text{else} \end{cases} \tag{5.12}$$

$$P(\gamma_{n+1} = d) = \begin{cases} p_{\mathrm{dd}} & \text{if } \gamma_n = \mathrm{d} \\ p_{\mathrm{bd}} & \text{else} \end{cases} \tag{5.13}$$

To obtain the direction of propagation δ_{n+1} we remark the following. If a particle crosses an interface and remains in its dynamical state ($\gamma_{n+1} = \gamma_n$), the direction of propagation will obviously stay unaltered, that is $\delta_{n+1} = \delta_n$. However, if the dynamical state of the particle changes when the trajectory crosses the interface ($\gamma_{n+1} \neq \gamma_n$), the direction of propagation can be reversed, too. To simplify matters we assume that the direction is just randomized in this case, i.e. if the dynamical state of the particle changes both directions are equally probable. In a nutshell this yields the equations

$$P(\delta_{n+1} = \delta_n) = 1 \qquad \text{if } \gamma_{n+1} = \gamma_n \tag{5.14}$$

$$P(\delta_{n+1} = \mathrm{l}) = P(\delta_{n+1} = \mathrm{r}) = 0.5 \qquad \text{else.} \tag{5.15}$$

In order to obtain the next position of the particle x_{n+1} and the arrival time t_{n+1} we must distinguish whether it is currently at an interface with convergent or divergent flux. The reasons for this will become clear in the course of the following discussion. Let us assume that the particle is currently at an interface with incoming currents. In Sec. 5.3 we discussed that it is a very unlikely event for a trajectory to traverse diffusively a block to the next interface opposite to the direction of the local current. On the contrary, at an interface with convergent flux the diffusive particles are localized and get sequentially transported back within a short period of time until a conversion to ballistic dynamics occurs. In our model the position of a diffusive particle remains the same as in the step before, i.e. $x_{n+1} = x_n$ if $\gamma_{n+1} = \mathrm{d}$. Furthermore, we keep in this case the arrival time unchanged because the diffusive particles remain so close to the interface that the time which elapses until the next crossing occurs is negligible, that is $t_{n+1} = t_n$ if $\gamma_{n+1} = \mathrm{d}$. Otherwise, if the particle is ballistic, it will traverse one of the adjacent blocks until it arrives at the next interface. Consequently, the position of the particle changes by the domain's length L_B, that is $x_{n+1} = x_n + L_B$ if the particle travels to the right $\delta_{n+1} = \mathrm{r}$ or vice versa $x_{n+1} = x_n - L_B$ if $\delta_{n+1} = \mathrm{l}$ ($L_B = N \cdot L = 5 \cdot 10^4$). In each case the arrival time is increased by the period of time a ballistic particle needs to traverse

a block t_b. For simplicity we have chosen $t_\mathrm{b} = 1.2 \cdot 10^4$ which is the mean of the dominant ballistic peak in Fig. 5.12 (see discussion in Sec. 5.4.1). In a summary the relations are at an interface with incoming current

$$x_{n+1} = \begin{cases} x_n & \text{if } \gamma_{n+1} = \mathrm{d} \\ x_n + L_B & \text{if } \gamma_{n+1} = \mathrm{b} \text{ and } \delta_{n+1} = \mathrm{r} \\ x_n - L_B & \text{if } \gamma_{n+1} = \mathrm{b} \text{ and } \delta_{n+1} = \mathrm{l}. \end{cases} \tag{5.16}$$

$$t_{n+1} = \begin{cases} t_n & \text{if } \gamma_{n+1} = \mathrm{d} \\ t_n + t_\mathrm{b} & \text{else.} \end{cases} \tag{5.17}$$

At an interface with divergent flux the situation is slightly different since a diffusive particle is not localized. Instead, it traverses one of the adjacent blocks, i.e. $x_{n+1} = x_n \pm L_B$. However, compared to a ballistic trajectory the timescale for a diffusive particle is larger because the average velocity is less. In our model we incorporate this fact by assigning $t_\mathrm{d} = 1.9 \cdot 10^5$, i.e. the characteristic time a diffusive particle needs to traverse a block (see Sec. 5.4.1), to such a "diffusive step" which is of course a rough approximation. Altogether, when the particle is currently at an interface with outgoing currents this yields

$$x_{n+1} = \begin{cases} x_n + L_B & \text{if } \delta_{n+1} = \mathrm{r} \\ x_n - L_B & \text{else.} \end{cases} \tag{5.18}$$

$$t_{n+1} = \begin{cases} t_n + t_\mathrm{b} & \text{if } \gamma_{n+1} = \mathrm{b} \\ t_n + t_\mathrm{d} & \text{else.} \end{cases} \tag{5.19}$$

Eqs. (5.12) - (5.19) define the map describing the effective "interface dynamics". For a given initial condition $\mathcal{X}_0$ this yields a sequence $\{\mathcal{X}_0, \ldots, \mathcal{X}_n\}$ which contains the information when the corresponding particle is at an interface. For this reason we can determine obviously at any point in time in which block the particle currently is. Moreover, for an ensemble of initial conditions it is thus possible to obtain in each block the number of the particles $n(x)$. Yet, the details of the spatial distribution within a domain cannot be resolved by the model because it is defined on a more coarse grained scale. In order to simplify matters we compare the results of iterating the model with the real dynamics of the ensemble of particles which has been placed in the chaotic sea close to the interface with incoming currents at the origin of the lattice. For this case the initial conditions $\mathcal{X}_0$ for the model are given by

$$\mathcal{X}_0 = (\gamma_0 = \mathrm{d}, \delta_0 = \{\mathrm{l/r}\}, x_0 = 0, t_0 = 0), \tag{5.20}$$

where both directions of propagation are equally probable, i.e. $P(\delta_0 = \mathrm{l}) = P(\delta_0 = \mathrm{r}) = 0.5$. For $t = 10^6$ the number of particles $n(x)$ obtained by iterating the mapping $\mathcal{T}$ with $5 \cdot 10^5$ initial conditions is shown in Fig. 5.15. Obviously, the curve is not smooth but has a zigzag shape because the model does not include the dynamics within a block, e.g. short ballistic flights due to stickiness to elliptic islands. Still, a comparison with the spatial distribution $\rho(x)$ shown in Fig. 5.14 (c) reveals that the Markov model reproduces qualitatively the form of $\rho(x)$. Especially, the position of the local extrema coincide, i.e. $n(x)$ possesses obviously in the same blocks as $\rho(x)$ its maxima / minima. However, we observe clear differences, too.

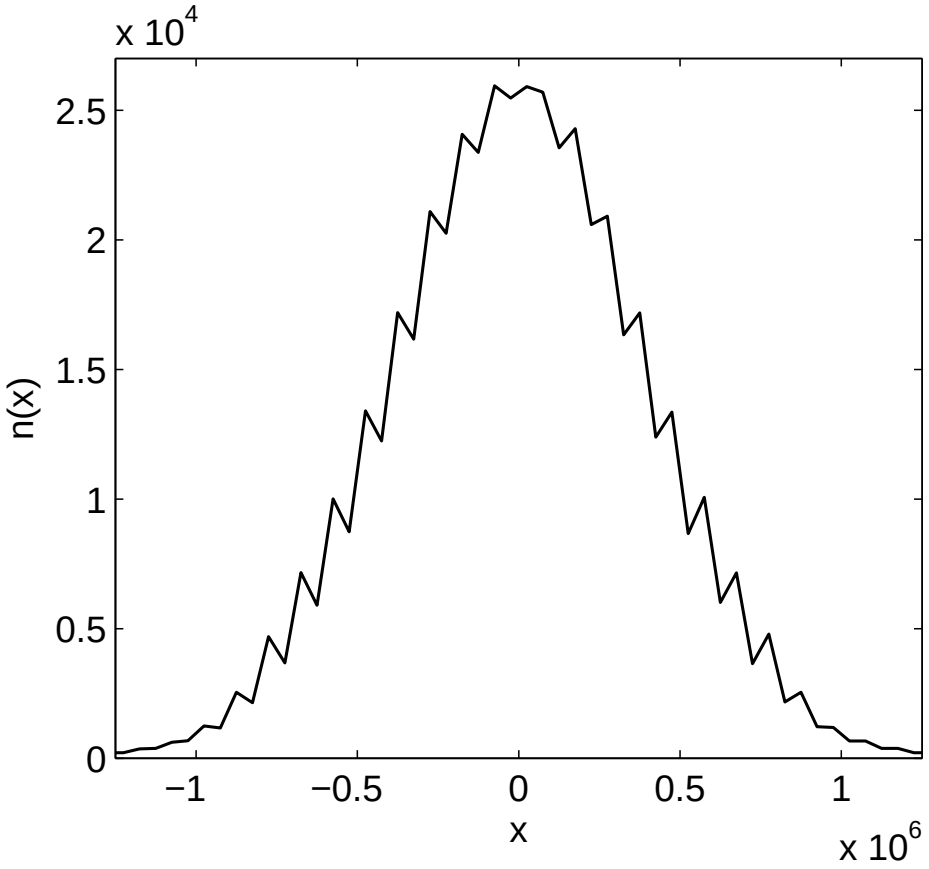

Figure 5.15: Number of particles resolved on the scale of a block $n(x)$ obtained by iterating the mapping for $5 \cdot 10^5$ particles started at the origin $x = 0$ of the lattice.

Apparently, the local extrema of $n(x)$ are not as pronounced as in $\rho(x)$. Furthermore, $\rho(x)$ obtained by simulating the real dynamics in the lattice is broader than the results from the mapping $n(x)$. Additionally, we remark that the mapping cannot reproduce the persistence of the local extrema, i.e. at some instants the peaks of $n(x)$ get smoothed out. In fact, the dynamics simulated by the mapping is very sensitive to the relation $t_\mathrm{b}/t_\mathrm{d}$, i.e. to the values we assigned for the time a ballistic / diffusive particle needs to cross a block. Since in the mapping's derivation several rough approximations have been done, it is not too surprising that the agreement is not exact. Nevertheless, the qualitative agreement of $n(x)$ with $\rho(x)$, that is the fact that the local extrema in the blocks are reproduced by the mapping, confirms that the dynamical conversion processes of the trajectories at the interfaces are the most crucial ingredient for the occurrence of the periodic density modulations.

5.6 Formation of density waves

So far the periodic density modulation has been merely a transient phenomenon, i.e. asymptotically the local extrema are smoothed out and the spatial particle density $\rho(x)$ converges to a Gaussian-shaped distribution. In this section we present a setup for which the periodic

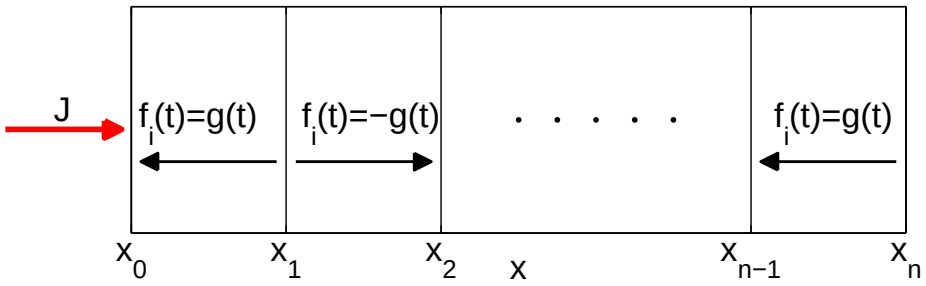

Figure 5.16: Sketch of the finite block system with constant beam of particles J entering the system at x_0. The arrows indicate the direction of the local current.

modulation becomes a steady state. Afterwards, it is shown how this steady state can be rendered into a propagating density wave.

To this end, we consider an extract of the infinite lattice, that is a finite open system composed of ten domains with an incoming constant current of particles (see Fig. 5.16 for a sketch). The driving law $f_i(t)$ in each block and the parameters of the barriers are chosen as before, i.e. the number of barriers in a block $N = 10^4$, potential height $V_0 = 2.2$, potential width $l = 1$, equilibrium distance $L = 5$, frequency $\omega = 1$ and amplitude $C = 0.57$. At the positions $x_i = i \cdot N \cdot L$ for $i = \{1, \ldots, 9\}$ are the interfaces with alternately incoming or outgoing currents from the neighboring domains, where the dynamical conversion processes of the trajectories occur. Since the parameters of the finite system are identical to the infinite lattice, the Poincaré surface of section of the domains (PSSD) are the same, too. Accordingly, the PSSD of block in the finite system with driving law $f_i(t) = g(t)$ / $f_i(t) = -g(t)$ are those shown in Fig. 5.4 (a) / (b). Similarly, the conversion sections at the interfaces with convergent / divergent flux are depicted in Fig. 5.6 (a) / (b). Moreover, the dynamical properties of the interfaces which have been discussed in the previous sections apply as well for the present finite system, i.e. at the interfaces with incoming flux the probability is high that a diffusive particle experiences a crossover to ballistic dynamics. Conversely, a ballistic particle is often injected into the chaotic sea at the interfaces with divergent currents. We feed the system with a constant beam of particles entering at x_0 (see Fig. 5.16) and the initial momenta are uniformly distributed with $0.1 \leq p \leq 4$. Once a corresponding trajectory reaches the position x_0 or x_{10} it is considered to be lost, i.e. we have absorbing boundary conditions. In the PSSD of the first block shown in Fig. 5.4 (c) the constant beam of particles is equivalent to a uniform distribution both in phase ξ and momentum p, i.e. ξ and p are randomly chosen from the intervals $[0, 2\pi[$ and $[0.1, 4]$ respectively. Consequently, most particles of the beam are injected into the chaotic sea of phase space with some ballistic initial conditions above the FISC.

Fig. 5.17 shows snapshots of the spatial density distribution of particles $\rho(x)$ at different instants. At $t = 10^4$ (Fig. 5.17 (a)) only the first block has been gradually filled with particles, i.e. $\rho(x) = 0$ for $x \gtrsim 0.5 \cdot 10^5$. Furthermore, $\rho(x)$ possesses a sharp peak at $x = 0$ which appears for the other snapshots, too (compare Fig. 5.17 (a) to (f)). Evidently, this peak is a trivial phenomenon due to the constant particle feed at $x = 0$. With increasing time $t = 10^5$ (Fig. 5.17 (b)) the trajectories have travelled deeper into the system whereas the particles show a accumulation at the interfaces with outgoing currents. Consequently, $\rho(x)$ has peaks

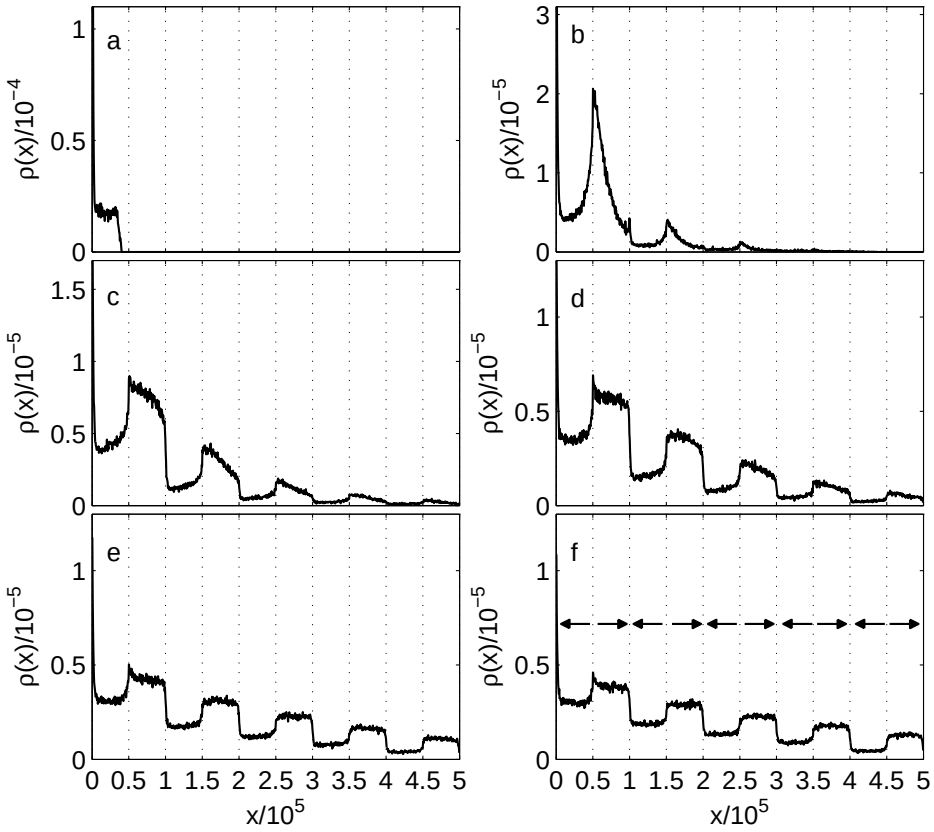

Figure 5.17: Spatial density distribution of particles $\rho(x)$ for a finite system composed of ten blocks and a constant beam of particles J entering at $x_0 = 0$. (a)-(f) show successively $\rho(x)$ for $t = 10^4$, 10^5, $3 \cdot 10^5$, $5 \cdot 10^5$, 10^6, 10^7. The black arrows in Fig. (f) indicate the direction of the local currents in the blocks.

at the positions $x_1 = 0.5 \cdot 10^5$, $x_3 = 1.5 \cdot 10^5$, $x_5 = 2.5 \cdot 10^5$. For $t = 3 \cdot 10^5$ (Fig. 5.17 (c)) the alternating local extrema on the scale of one block start to emerge. In Fig. 5.17 (d) ($t = 5 \cdot 10^5$) the system has been filled with more particles and their spatial distribution $\rho(x)$ has developed further to the expected form of piecewise constant local extrema on the scale of one block. Nevertheless, afar from $x_0 = 0$, where the system is fed by the particle beam, $\rho(x)$ still changes, e.g. in the sixth block $\rho(x)$ is not yet constant. For $t = 10^6$ (see Fig. 5.17 (e)) the characteristic periodic modulations of $\rho(x)$ have developed completely. An equilibrium has been established between the number of particles which still get injected into the system at x_0 and the number of trajectories leaving at x_0 and x_{10}. $\rho(x)$ is in each block constant and possesses alternately a local maximum or minimum. Afterwards, no more changes of $\rho(x)$ occur as Fig. 5.17 (e) ($t = 10^6$) and Fig. 5.17 (f) ($t = 10^7$) reveal. Comparing Fig. 5.17 (f) with Fig. 5.9 (d) shows that the extrema of $\rho(x)$ emerge for both the finite system and the infinite lattice in the blocks with the same local currents, i.e. the maxima are in the domains with positive transport velocity and vice versa for the minima. Contrary to the infinite lattice where the periodic modulations are smoothed out asymptotically, the form of $\rho(x)$ shown in Fig. 5.17 (f) is converged due to the constant feeding of the finite system. In Fig. 5.17 (f) we observe furthermore that $\rho(x)$ has a local minimum / maximum in the next-to-last / last

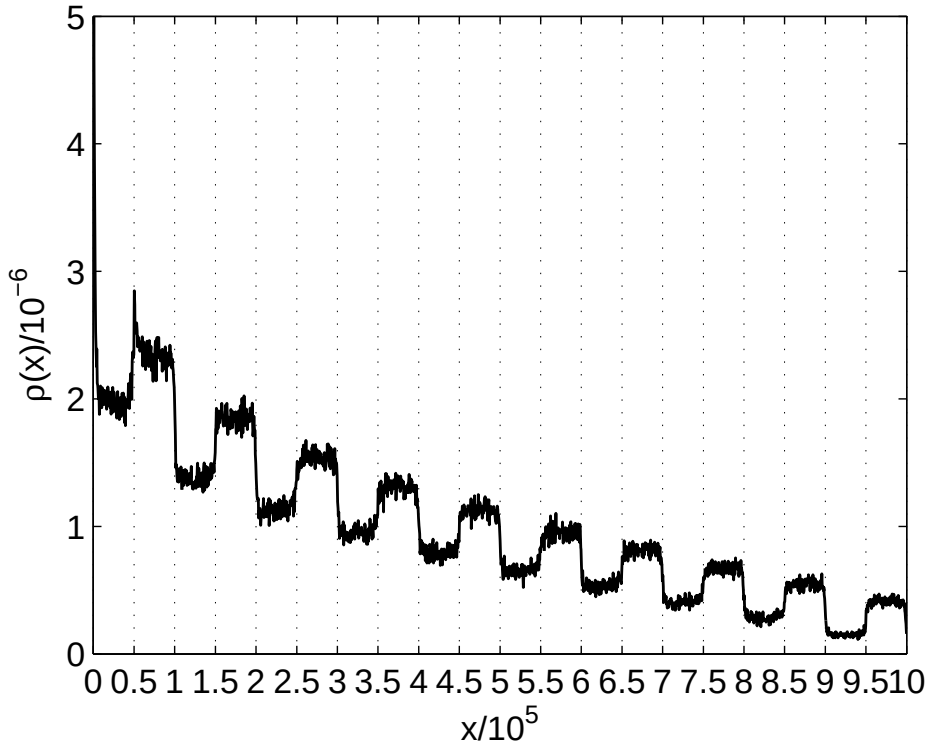

Figure 5.18: Spatial density distribution of particles $\rho(x)$ at $t = 10^7$ for a finite system composed of twenty blocks and a constant beam of particles J entering at $x_0 = 0$

block which is a counterintuitive behavior at first glance. Due to the fact that the particles reaching the end of the system at $x_{10} = 5 \cdot 10^5$ are gone, the spatial distribution of particles $\rho(x)$ in the last block should be less because it is closer to the absorbing boundary. At least this is the expectation, if the dynamical composition of the trajectories would be equal over the system, i.e. no accumulation of particles with e.g. diffusive dynamics in certain blocks. Accordingly, we can assume that similar to infinite lattice the interfaces and the dynamical conversion processes are the origin for periodic modulations of $\rho(x)$ in the finite system shown in Fig. 5.17 (f). A final observation made from Fig. 5.17 (f) is that $\rho(x)$ has a decreasing envelope. Evidently, this behavior is just due to the fact that the particles enter permanently the system at $x_0 = 0$ and are absorbed at $x_{10} = 5 \cdot 10^5$.

In the following we discuss the occurrence of the asymptotic state shown in Fig. 5.17 (f) in more detail. Since the beam is injected in a block whose local current points into the opposite direction only the particles obeying ballistic dynamics are able to reach the interface at $x_1 = 0.5 \cdot 10^5$. The diffusive trajectories are transported back to the opening of the system and absorbed at $x_0 = 0$. Therefore, the initial momentum p must be large enough[1]. When the ballistic trajectories reach the interface at $x_1 = 0.5 \cdot 10^5$ with divergent flux a decent

[1]For example, in a simulation, where p is chosen randomly from the interval $[0.1, 1]$, no particle ever reaches the second domain because in this case the initial conditions overlap solely with the chaotic sea of the first block's phase space.

amount of them experiences a conversion to diffusive dynamics and maintains the direction of propagation. Consequently, these particles move diffusively according to the direction of the local transport until they arrive at the interface with convergent flux at $x = 10^5$. Now the diffusive trajectories cannot cross the next block because the local current points into the opposite direction unless a crossover back to ballistic dynamics occurs. In this case the particles traverse the domain and the described procedure repeats at the subsequent interfaces, i.e. typically the particles obey alternately diffusive and ballistic dynamics. Accordingly, we get an enhanced number of particles obeying diffusive dynamics in blocks whose local transport points into the same direction as the incoming beam. Due to the larger average dwell-time (or smaller average velocity) of a diffusive trajectory compared to a particle obeying ballistic dynamics, the inhomogeneous distribution of diffusive trajectories in the system yields the local maxima / minima of $\rho(x)$ in domains with positive / negative transport velocity. Similarly to the previously studied infinite lattice the key to understand the periodic modulations of $\rho(x)$ are the dynamical conversion processes occurring at the interfaces. In Ref. [84] the aforementioned ideas have been included in a model which predicts $\rho(x)$ in each block.

Of course the occurrence of the local extrema does not depend on the size of the system. Fig. 5.18 shows the spatial distribution of particles $\rho(x)$ at $t = 10^7$ for twenty blocks. Obviously, $\rho(x)$ possesses as before maxima in blocks with positive local transport and minima in blocks with negative current. Nonetheless, the time when $\rho(x)$ reaches its equilibrium state increases linearly with the size of system, e.g. for ten blocks the spatial particle distribution $\rho(x)$ has converged at $t \approx 10^6$ whereas for the system consisting of twenty blocks $\rho(x)$ reaches its equilibrium state at $t \approx 2 \cdot 10^6$.

Let us now come to the procedure with which the equilibrium state of the spatial particle distribution $\rho(x)$ can be rendered into a temporally propagating density wave. To this end we consider again a finite system composed of ten blocks, feed it with a constant beam of particles entering at $x_0 = 0$ and wait until $t = 10^6$ when $\rho(x)$ reaches its equilibrium state. Afterwards, we start to move the interfaces through the system by switching consecutively the driving laws of the barriers. Fig. 5.19 shows a sequence of snapshots of the spatial particle distribution $\rho(x)$ for different points in time. The blue / red lines are the positions of the interfaces with divergent / convergent flux. At $t = 10^6$ (Fig. 5.19 (a)) the equilibrium state of the spatial particle distribution $\rho(x)$ with alternating local extrema on the scale of one block has fully developed. Figs. 5.19 (a)-(e) reveal that $\rho(x)$ follows subsequently the movement of the interfaces while the characteristic form of $\rho(x)$ with periodic modulations on the scale of one block is preserved. For example, at $t = 1.5 \cdot 10^6$ (Fig. 5.19 (e)) the local current in each block has been reversed, i.e. compared to the snapshot at $t = 10^6$ the interfaces and the maxima / minima have interchanged their positions. Since the spatial distribution of the particles follows adiabatically the change of the lattice, this movement of the interfaces results in a propagating density wave in the system. Fig. 5.19 (f) shows $\rho(x)$ for $t = 9.25 \cdot 10^6$ which reveals that the wave does not get smoothed out significantly even for very long propagation times. Still, it is important to note that the movement of the interfaces through the system must not be too fast. Otherwise, the spatial particle distribution cannot follow the change of the lattice and the periodic modulations vanish.

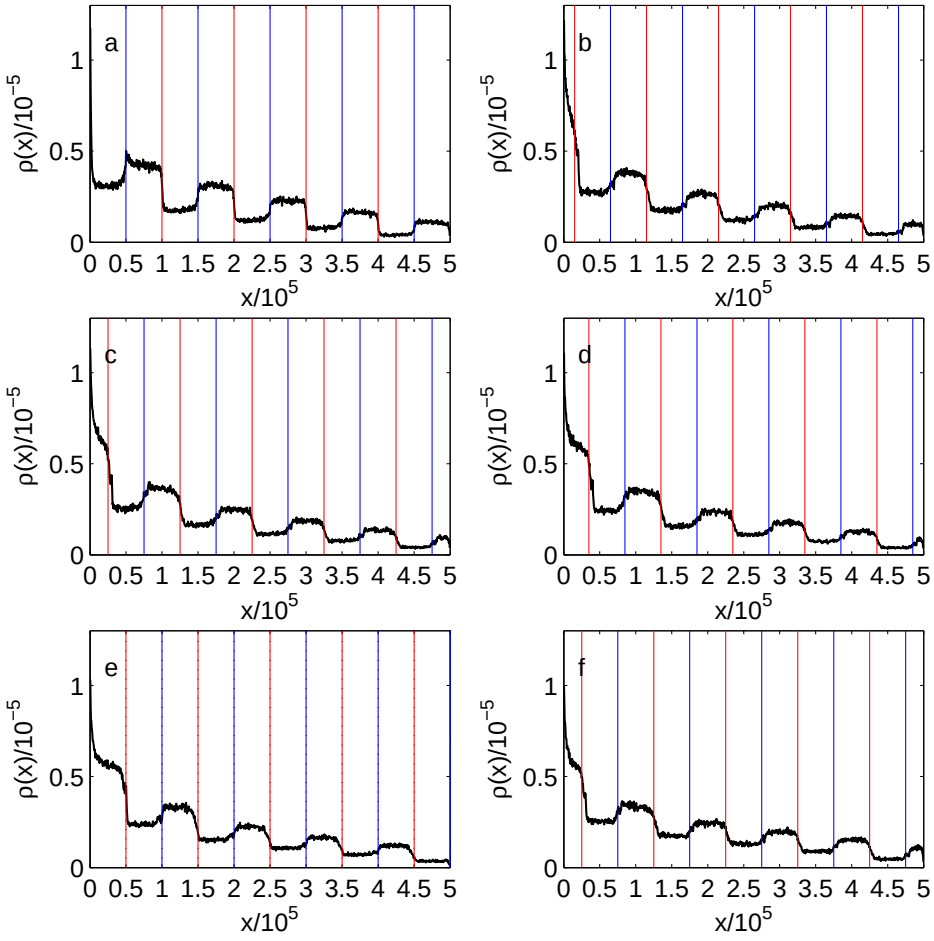

Figure 5.19: Snapshots of the spatial particle distribution $\rho(x)$ at different times when the interfaces move through the system.Sketch of the finite block system with constant beam of particles J entering the system at x_0. Figs. 5.19 (a)-(f) show $\rho(x)$ for $t = 10^6$, $1.16 \cdot 10^6$, $1.25 \cdot 10^6$, $1.35 \cdot 10^6$, $1.5 \cdot 10^6$ and $t = 9.25 \cdot 10^6$. The blue / red lines are the positions of the interfaces with outgoing / incoming flux.

5.7 Summary

In this chapter the properties of block-structured infinite lattices as well as finite systems have been analyzed. By concatenating domains with different local transport properties it is possible to evoke conversion processes of trajectories from diffusive to ballistic dynamics and vice versa. We have traced these dynamical conversion processes back to the overlap of the phase space structures at the positions of the interfaces. Subsequently, it has been shown that they leave their hallmarks in the evolution of an ensemble of trajectories leading to the periodic modulations of the spatial particle distribution $\rho(x)$, i.e. local extrema of $\rho(x)$ on the scale of one block which can be reproduced qualitatively by a simple Markov chain model. As the next step we have considered a finite system which is fed by a constant beam of particles. In this system the density modulation, which has been a transient phenomenon for the case of infinite lattice, becomes a steady state that can be rendered into a propagating wave by manipulating temporally the driving laws of the barriers.

In a summary these results demonstrate that the local driving of the barriers induces a rich phenomenology like the the dynamical conversion process of trajectories at interfaces between differently driven domains. In a system with uniform driving we can have stickiness of chaotic trajectories to elliptic islands leading to ballistic flights. However, this is not a controllable effect since the start and the end of such a ballistic flight cannot be predicted. Contrary, in the block-structured lattice the particles can be injected at an interface from the chaotic sea into an elliptic island. Subsequently, these trajectories are trapped in the island until they arrive at the next interface. In Ref. [84] it has been shown meanwhile that by manipulating appropriately the dynamical conversion properties of the interfaces one can transform an ensemble of diffusive particles into a mono-energetic beam.

Chapter 6

Quantum Dynamics

In this chapter the dynamics of a quantum particle loaded in a phase-modulated driven lattice is studied. We present the numerical scheme for obtaining the time-evolution operator and show how observables like the transport velocity can be obtained. Afterwards, we discuss the transport of the lattice and its dependence on the local phase shifts or the frequency of the driving.

6.1 General definitions

Analogous to the classical case we consider non-interacting, identical particles loaded into a one-dimensional driven lattice. Accordingly, the quantum dynamics is governed by the time-dependent Schrödinger equation

$$i\hbar\frac{\partial\Psi(x,t)}{\partial t} = H(x,t)\Psi(x,t), \tag{6.1}$$

where the Hamiltonian $H(x,t)$ is given by

$$H(x,t) = -\frac{\hbar^2}{2m}\frac{\partial^2}{\partial x^2} + V(x,t), \tag{6.2}$$

whereas we take $\hbar = m = 1$ in the following. For the potential $V(x,t)$ we have chosen an infinite lattice of laterally oscillating Gaussian potentials[1], i.e.

$$V(x,t) = \sum_{i=-\infty}^{\infty} V_0 \exp\left(-\left(\frac{x - x_{0,i} - f_i(t)}{\delta}\right)^2\right), \tag{6.3}$$

with equal potential height V_0 and width δ. $x_{0,i}$ is the equilibrium position and $f_i(t)$ the driving law of the i-th barrier. As in the classical case the static counterpart is a lattice of equidistant barriers. Fig. 6.1 shows a sketch of the system with all parameters. Although the Gaussian function has only faint tails, it does not vanish exactly. Therefore, the parameters of the potential, i.e. its height V_0, the equilibrium distance D, the width δ and the amplitude of the driving laws $f_i(t)$, must be chosen appropriately such that the overlap of neighboring Gaussians is negligible. Just as in the classical case we take for the driving law of the i-th Gaussian barrier a harmonic function with the same frequency and amplitude but a site-

[1] The reasons why we consider in the quantum system smooth potentials rather than rectangular barriers as in the classical case are addressed at a later point in this thesis.

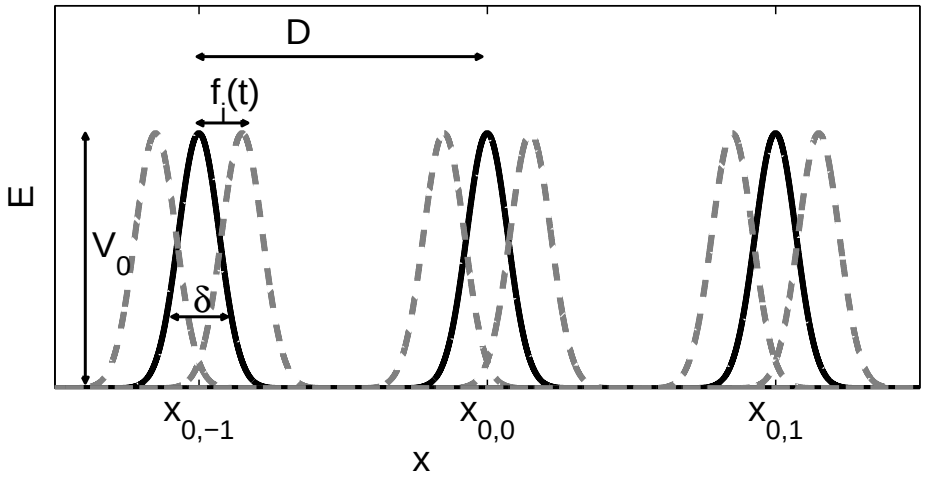

Figure 6.1: Schematic illustration of the driven lattice

dependent local phase shift φ_i. Accordingly, $f_i(t)$ is given by

$$f_i(t) = C\cos(\omega(t+t_0)+\varphi_i), \tag{6.4}$$

where t_0 is the initial phase of the driving. In the classical system t_0 has been omitted because a global phase shift is irrelevant for the transport properties of particles initialized in the chaotic sea which can be understood straightforwardly. Chaotic dynamics leads to an exponentially fast decay of correlations [5, 87]. Consequently, for the classical lattice the initial information is erased completely after a few periods of the driving. Thus, the transport velocity is independent from t_0, as long as the initial ensemble is started in the chaotic sea. On the contrary, the quantum dynamics depends on the initial state so that a dependency of the magnitude and the direction of the transport on t_0 can be expected [60, 88]. In fact, we will see later that even when no transport is observed in the classical case because the spatiotemporal symmetries are not broken the quantum system can show a nonzero current for specific t_0.

Before we proceed to the numerical scheme for obtaining the time-evolution operator of the Schrödinger equation, let us specify briefly the setups whose transport properties will be studied. In the following the parameters of the potential are fixed to $V_0 = 1$, $D = 10$, $\delta = 1/2$ and $C = 1$. In this case the Gaussians decrease rapidly such that the potential between neighboring barriers becomes negligible, i.e. $V(x,t) < 10^{-16}$. Accordingly, for this choice of the parameters $V(x,t)$ can be considered as a sum of localized Gaussian functions which is an important condition for the later discussion. Analogous to the classical case the local phase shifts φ_i can be modulated spatially. More precisely, we have chosen the following two setups:

(a) The local phase shift is zero for all barriers, i.e. $\varphi_i = 0$, which corresponds to a lattice of uniformly, laterally oscillating Gaussian potential barriers. In this case the potential $V(x,t)$

is invariant under the parity and the time-reversal transformation, that is

$$T : x \to -x, \;\; t \to t + \frac{\pi}{\omega}, \tag{6.5}$$

$$T' : x \to x, \;\; t \to -t, \tag{6.6}$$

which implies the absence of directed transport for symmetry reasons in the classical system.

(b) The local phase shifts φ_i are modulated periodically, i.e. $\varphi_{i+n_P} = \varphi_i$. We have chosen the constant phase gradient with $n_P = 3$. Accordingly, the sequence of phase shifts φ_i is $\{\ldots, 0, \frac{2\pi}{3}, \frac{4\pi}{3}, \ldots\}$. In this case both spatiotemporal symmetries are broken, hence in the classical system a current is expected to occur.

6.2 Floquet theory

Since the Hamiltonian is periodic in time $H(x, t+T) = H(x, t)$, $(T = \frac{2\pi}{\omega})$ we can apply "Floquet theory" [67–69]. According to the Floquet theorem there are solutions of the Schrödinger equation which have the form

$$\Psi_\lambda(x, t) = e^{-i\epsilon_\lambda t/\hbar}\Phi_\lambda(x, t), \tag{6.7}$$

where $\Phi_\lambda(x, t)$ is called "Floquet mode" and has the same period as the Hamiltonian, i.e.

$$\Phi_\lambda(x, t + T) = \Phi_\lambda(x, t). \tag{6.8}$$

ϵ_λ is a real number which is referred to as "Floquet energy" or often also "quasienergy". A term chosen due to the formal analogy of Eq. (6.7) to the Bloch states with "quasimomentum" κ appearing in solid state physics. Substituting the Floquet solutions (6.7) into the Schrödinger equation (6.1) yields the following eigenvalue equation for the quasienergies and the corresponding Floquet modes

$$H_F(x, t)\Phi_\lambda(x, t) = \epsilon_\lambda\Phi_\lambda(x, t), \tag{6.9}$$

where $H_F(x, t)$ is the "Floquet Hamiltonian" given by

$$H_F(x, t) = H(x, t) - i\hbar\frac{\partial}{\partial t}. \tag{6.10}$$

Straightforward algebra shows that a Floquet solution $\Psi_\lambda(x, t)$ has the following shift symmetry

$$\Psi_\lambda(x, t) = e^{-i\epsilon_\lambda t/\hbar}\Phi_\lambda(x, t) \tag{6.11}$$

$$= e^{-i(\epsilon_\lambda + n\hbar\omega)t/\hbar}e^{in\omega t}\Phi_\lambda(x, t), \tag{6.12}$$

Evidently, we get a new Floquet eigenstate

$$\Phi_{\lambda n}(x, t) = e^{in\omega t}\Phi_\lambda(x, t) \tag{6.13}$$

and its corresponding quasienergy $\epsilon_{\lambda n} = \epsilon_\lambda + n\hbar\omega$. For $n \in \mathbb{Z}$ the mode $\Phi_{\lambda n}(x,t)$ obeys the same periodicity as $\Phi_\lambda(x,t)$, i.e. $\Phi_{\lambda n}(x,t+T) = \Phi_\lambda(x,t)$. Still, the physical state $\Psi_\lambda(x,t)$ remains unchanged under this shift transformation which implies that the quasienergies ϵ_λ are defined modulo $\hbar\omega$. Consequently, we can map ϵ_λ to the interval $[-\hbar\omega/2, \hbar\omega/2]$, which is sometimes also called the first Brillouin zone. Another term borrowed from the physics of periodic solids.

In face of the further discussion it is convenient to define for the Floquet Hamiltonian $H_F(x,t)$ the composite Hilbert space $\mathcal{R}\otimes\mathcal{T}$ consisting of the Hilbert space $\mathcal{R}$ of the Hamiltonian $H(x,t)$ and the space $\mathcal{T}$ of the time-periodic functions (period $T = \frac{2\pi}{\omega}$) [68, 89, 90]. The Hilbert space $\mathcal{R}$ is spanned by any set of square-integrable functions forming an orthonormal basis $\{|\alpha\rangle\}$ in configuration space whereas the inner product is defined by

$$\langle\alpha|\beta\rangle = \int_{-\infty}^{\infty} dx\, \alpha^*(x)\beta(x) = \delta_{\alpha\beta} \tag{6.14}$$

The temporal part is spanned by the orthonormal set of Fourier vectors $\{|n\rangle\}$ satisfying $\langle t|n\rangle = e^{in\omega t}$, $n \in \mathbb{Z}$. The inner product in $\mathcal{T}$ is given by

$$\langle n|m\rangle = \frac{1}{T}\int_0^T dt\, e^{i(m-n)\omega t} = \delta_{nm}. \tag{6.15}$$

Accordingly, in the composite Hilbert space $\mathcal{R}\otimes\mathcal{T}$ the inner product is defined by

$$\langle\langle\Phi_{\lambda n}|\Phi_{\nu m}\rangle\rangle = \frac{1}{T}\int_0^T dt \int_{-\infty}^{\infty} dx \Phi^*_{\lambda n}(x,t)\Phi_{\nu m}(x,t). \tag{6.16}$$

The Floquet eigenstates $\Phi_{\lambda n}(x,t)$ satisfy the orthonormality condition

$$\langle\langle\Phi_{\lambda n}|\Phi_{\nu m}\rangle\rangle = \delta_{\lambda\nu}\delta_{nm} \tag{6.17}$$

and form a complete set in $\mathcal{R}\otimes\mathcal{T}$

$$\sum_{\lambda n} |\Phi_{\lambda n}\rangle\rangle\langle\langle\Phi_{\lambda n}| = \mathbf{1} \tag{6.18}$$

It is important to note that the Floquet eigenstates $\Phi_{\lambda n}(x,t)$ and $\Phi_{\lambda m}(x,t)$ with $n \neq m$ are distinct vectors in composite Hilbert space $\mathcal{R}\otimes\mathcal{T}$, i.e. for the expansion of a wavefunction in $\mathcal{R}\otimes\mathcal{T}$ all values of n are needed [67]. Yet, for the expansion of a physical wavefunction $\Psi(x,t)$ in the Hilbert space $\mathcal{R}$ the Floquet modes $\Phi_\lambda(x,t)$ of the first Brillouin zone $n = 0$ are sufficient.

6.3 Time-evolution operator

The time evolution operator $U(t,t_0)$ which is defined by

$$\Psi(x,t+t_0) = U(t,t_0)\Psi(x,t_0), \tag{6.19}$$

$$U(t_0,t_0) = \mathbf{1} \tag{6.20}$$

obeys special properties for periodic Hamiltonians $H(t+T) = H(t)$. Formally, $U(t, t_0)$ can be written as

$$U(t, t_0) = \mathbb{T} \exp\left(-\frac{i}{\hbar}\int_{t_0}^{t} dt' H(t')\right), \tag{6.21}$$

where $\mathbb{T}$ denotes the time ordering operator. For time-periodic Hamiltonians it can be shown (Ref. [91]) that the time evolution operator has the following property

$$U(t+T, 0) = U(t, 0)U(T, 0), \tag{6.22}$$

from which immediately follows that

$$U(nT, 0) = U(T, 0)^n. \tag{6.23}$$

Consequently, the time evolution operator over one period $U(T, 0)$ contains the full information needed to propagate stroboscopically a time-periodic quantum system.

Additionally, it is easy to show that the Floquet modes $\Phi_\lambda(x, 0)$ are eigenstates of $U(T, 0)$ which becomes immediately obvious from the following considerations [92]. Applying $U(T, 0)$ to the Floquet solution $\Psi_\lambda(x, 0)$ yields

$$\begin{aligned} U(T,0)\Psi_\lambda(x,0) &= \Psi_\lambda(x,T) \\ &= e^{-i\epsilon_\lambda T/\hbar}\Phi_\lambda(x,T) \\ &= e^{-i\epsilon_\lambda T/\hbar}\Phi_\lambda(x,0) \end{aligned} \tag{6.24}$$

Moreover, it follows from Eq. (6.7) for $t = 0$ that we have $\Psi_\lambda(x, 0) = \Phi_\lambda(x, 0)$, i.e.

$$U(T,0)\Phi_\lambda(x,0) = e^{-i\epsilon_\lambda T/\hbar}\Phi_\lambda(x,0) \tag{6.25}$$

Evidently, Eq. (6.25) is an eigenvalue problem for the Floquet modes $\Phi_\lambda(x, 0)$ with eigenvalues $e^{-i\epsilon_\lambda T/\hbar}$.

6.4 Floquet matrix method

In general, the exact analytical solution of the time-dependent Schrödinger equation with a Hamiltonian periodic in time is not possible. Therefore, we rely on numerical approaches in order to compute the Floquet modes and their quasienergies. In this section we address the so-called "Floquet matrix method" which is based on a representation of the Floquet Hamiltonian H_F in a complete basis of the composite Hilbert space $\mathcal{R} \otimes \mathcal{T}$ [67, 68, 92]. We follow the discussion in [92]. According to the previous discussion it is known that the Floquet modes $\Phi_\lambda(x, t)$ and the quasienergies ϵ_λ are the solutions of the Eq. (6.9). Since the Floquet mode $\Phi_\lambda(x, t)$ is time-periodic, we can expand it in a Fourier series, i.e.

$$\Phi_\lambda(x, t) = \sum_m \phi_\lambda^{(m)}(x) e^{im\omega t}, \tag{6.26}$$

with $m \in \mathbb{Z}$. Let us now assume that we have chosen a complete basis for the Hilbert space $\mathcal{R}$ which is denoted in the following by $\{|\beta\rangle\}$. Each function $\phi_\lambda^{(m)}(x)$ can be represented in

terms of the complete set $\{|\beta\rangle\}$, that is

$$\phi_\lambda^{(m)}(x) = \sum_\beta \phi_{\beta\lambda}^{(m)} |\beta\rangle. \tag{6.27}$$

Inserting Eqs. (6.26) and (6.27) in the Eq. (6.9) yields

$$\sum_{\beta m} (H(x,t) + m\hbar\omega)\phi_{\beta\lambda}^{(m)} |\beta\rangle e^{im\omega t} = \sum_{\beta m} \epsilon_\lambda \phi_{\beta\lambda}^{(m)} |\beta\rangle e^{im\omega t} \tag{6.28}$$

Multiplying this expression from the left with $\langle\alpha|e^{-in\omega t}$ gives

$$\sum_{\beta m} (\langle\alpha|H(x,t)e^{i(m-n)\omega t}|\beta\rangle + m\hbar\omega\langle\alpha|\beta\rangle e^{i(m-n)\omega t})\phi_{\beta\lambda}^{(m)} = \sum_{\beta m} \epsilon_\lambda \phi_{\beta\lambda}^{(m)} \langle\alpha|\beta\rangle e^{i(m-n)\omega t}. \tag{6.29}$$

With the orthonormality conditions (6.14) and (6.15) we get after averaging over one period T a set of coupled equations for the quasienergies ϵ_λ and the expansion coefficients $\phi_{\alpha\lambda}^{(n)}$ of the Floquet modes [92]

$$\sum_{\beta m} (\langle\alpha|H^{(n-m)}(x)|\beta\rangle + m\hbar\omega\delta_{nm}\delta_{\alpha\beta})\phi_{\beta\lambda}^{(m)} = \epsilon_\lambda \phi_{\alpha\lambda}^{(n)}, \tag{6.30}$$

where the following definition has been used

$$H^{(n-m)}(x) = \frac{1}{T}\int_0^T dt H(x,t) e^{i(m-n)\omega t}. \tag{6.31}$$

Since the Hamiltonian $H(x,t)$ is periodic, $H^{(n-m)}(x)$ is the n-m-th expansion coefficient of the Fourier series of $H(x,t)$, i.e.

$$H(x,t) = \sum_{n=-\infty}^{\infty} H^{(n)}(x) e^{in\omega t}. \tag{6.32}$$

If we define the product states $|\alpha n\rangle\rangle = |\alpha\rangle \otimes |n\rangle$ in the composite Hilbert space $\mathcal{R} \otimes \mathcal{T}$, where $\{|\alpha\rangle\}$ is the chosen basis in $\mathcal{R}$ and $\{|n\rangle\}$ are the Floquet vectors forming the basis in $\mathcal{T}$ ($\langle t|n\rangle = e^{in\omega t}$), Eq. (6.30) can be written in form of a matrix eigenvalue equation

$$\sum_{\beta m} \langle\langle \alpha n|H_F|\beta m\rangle\rangle \phi_{\beta\lambda}^{(m)} = \epsilon_\lambda \phi_{\alpha\lambda}^{(n)}. \tag{6.33}$$

$\langle\langle \alpha n|H_F|\beta m\rangle\rangle$ is the time-independent matrix representation of the Floquet Hamiltonian ("Floquet matrix" [92]) which is given by

$$\langle\langle \alpha n|H_F|\beta m\rangle\rangle = H_{\alpha\beta}^{(n-m)} + n\hbar\omega\delta_{\alpha\beta}\delta_{nm}, \tag{6.34}$$

where $H_{\alpha\beta}^{(n-m)} = \langle\alpha|H^{(n-m)}(x)|\beta\rangle$ is the matrix representation of the n-m-th Fourier component of the Hamiltonian $H^{(n-m)}(x)$ (Eq. (6.31)) in a basis $\{|\alpha\rangle\}$ of the Hilbert space $\mathcal{R}$, i.e.

$H_{\alpha\beta}^{(n-m)}$ is a (block) matrix in $\mathcal{R}$. In the following we show the typical form of the Floquet matrix $[H_F] = \langle\langle \alpha n | H_F | \beta m \rangle\rangle$

$$
[H_F] = \begin{array}{c}
\begin{array}{ccccc} m=2 & m=1 & m=0 & m=-1 & m=-2 \end{array} \\
\begin{pmatrix}
\ddots & & & & & \\
H_{\alpha\beta}^{(0)} + 2\hbar\omega\mathbf{1} & H_{\alpha\beta}^{(1)} & H_{\alpha\beta}^{(2)} & H_{\alpha\beta}^{(3)} & H_{\alpha\beta}^{(4)} & \\
H_{\alpha\beta}^{(-1)} & H_{\alpha\beta}^{(0)} + \hbar\omega\mathbf{1} & H_{\alpha\beta}^{(1)} & H_{\alpha\beta}^{(2)} & H_{\alpha\beta}^{(3)} & \\
H_{\alpha\beta}^{(-2)} & H_{\alpha\beta}^{(-1)} & H_{\alpha\beta}^{(0)} & H_{\alpha\beta}^{(1)} & H_{\alpha\beta}^{(2)} & \\
H_{\alpha\beta}^{(-3)} & H_{\alpha\beta}^{(-2)} & H_{\alpha\beta}^{(-1)} & H_{\alpha\beta}^{(0)} - \hbar\omega\mathbf{1} & H_{\alpha\beta}^{(1)} & \\
H_{\alpha\beta}^{(-4)} & H_{\alpha\beta}^{(-3)} & H_{\alpha\beta}^{(-2)} & H_{\alpha\beta}^{(-1)} & H_{\alpha\beta}^{(0)} - 2\hbar\omega\mathbf{1} & \\
& & & & \ddots
\end{pmatrix}
\begin{array}{l} n=2 \\ n=1 \\ n=0 \\ n=-1 \\ n=-2 \end{array}
\end{array}
$$

Evidently, $[H_F]$ is a matrix whose elements are again matrices. According to Eq. (6.33) the quasienergies ϵ_λ are the eigenvalues of $[H_F]$, that is solutions of the secular equation [69]

$$\det |[H_F] - \epsilon\mathbf{1}| = 0. \tag{6.35}$$

However, the direct diagonlization of the Floquet matrix $[H_F]$ has the major drawback that $[H_F]$ is unbounded and must therefore be truncated for numerical calculations. In general, the number of blocks of the Floquet matrix $[H_F]$, which have to be taken into account in order to obtain numerically accurate results depends on the question how fast the Fourier series of the Hamiltonian converges. For example, let us assume that the potential of the Hamiltonian has the form $V(x,t) \propto \cos(\omega t)$. Due to the fact that the Fourier series of the cosine is simply $\cos(\omega t) = \frac{1}{2}(e^{i\omega t} + e^{-i\omega t})$, the Floquet matrix $[H_F]$ has in this case a tridiagonal structure because the Fourier components of the Hamiltonian $H^{(n)}(x)$ (Eq. (6.31)) vanish for $|n| > 1$, i.e. $H_{\alpha\beta}^{(\pm 2, \pm 3, \ldots)} = \langle \alpha | H^{(\pm 2, \pm 3, \ldots)}(x) | \beta \rangle = 0$. Usually, a moderate number of blocks of the Floquet matrix (e.g. 50 in Ref. [93]) is then sufficient to get converged results. Evidently, for driving laws with several frequencies, e.g. $V(x,t) \propto \cos(\omega t) + \cos(2\omega t)$ where the Fourier series of the Hamiltonian possess more nonzero expansion coefficients, the number of necessary blocks of the Fourier matrix increases, too. Later we will see that in our case the Fourier expansion of the potential $V(x,t)$ is a relatively slowly converging series so that a huge number of blocks of the Floquet matrix $[H_F]$ would be needed. Additionally, each element of $[H_F]$ is again a matrix whose rank depends on the dimension of the basis $\{|\alpha\rangle\}$ of the Hilbert space $\mathcal{R}$. Consequently, the memory needed on a computer for storing the Floquet matrix $[H_F]$ becomes very large which makes the diagonlization of $[H_F]$ inconvenient if not impossible. Therefore, in order to determine the Floquet modes and the quasienergies we have chosen the so-called "propagator method" which makes use of the Floquet matrix $[H_F]$ but is numerically much easier to handle.

6.5 Propagator method

Contrary to the "Floquet matrix method" which is based on transforming the time-dependent Floquet problem (6.9) into an infinitely dimensional time-independent eigenvalue equation

(6.35) the propagator methods exploits the fact that the Floquet modes $\Phi_\lambda(x,0)$ are eigenvectors of the time-evolution operator over one period $U(T,0)$ to complex eigenphases $e^{-i\epsilon_\lambda T/\hbar}$ (Eq. (6.25)). Consequently, representing $U(T,0)$ in a truncated basis $\{|\alpha\rangle\}$ of the Hilbert space $\mathcal{R}$ and diagonalizing the resulting matrix $U_{\alpha\beta}(T,0)$ yields the Floquet modes $\Phi_\lambda(x,0)$ and their corresponding quasienergies ϵ_λ. In the following we explain how $U_{\alpha\beta}(T,0)$ is calculated. According to [67, 69, 90] the matrix representation of the time evolution operator $U(t,t_0)$ for a time-periodic Hamiltonian in a basis $\{|\alpha\rangle\}$ of the Hilbert space $\mathcal{R}$ is given by

$$U_{\alpha\beta}(t,t_0) = \sum_{n=-\infty}^{\infty} \langle\langle \alpha n | e^{-iH_F(t-t_0)/\hbar} | \beta 0 \rangle\rangle e^{in\omega t}, \tag{6.36}$$

where H_F is the Floquet Hamiltonian operator (Eq. (6.10)). To determine the one period time-evolution operator $U(T,0)$, we divide the period T into small intervals of length $\Delta t = T/N$ such that

$$U(T,0) = U(N\Delta t,(N-1)\Delta t)\cdot U((N-1)\Delta t,(N-2)\Delta t)\cdot \ldots \cdot U(\Delta t,0). \tag{6.37}$$

Due to Eq. (6.36) each $U(k\Delta t,(k-1)\Delta t)$ $(k \in 1,2,\ldots,N)$ can be written as

$$U_{\alpha\beta}(k\Delta t,(k-1)\Delta t) = \sum_{n=-\infty}^{\infty} \langle\langle \alpha n | e^{-iH_F\Delta t/\hbar} | \beta 0 \rangle\rangle e^{in\omega k\Delta t}. \tag{6.38}$$

When N is chosen large enough, the exponential function can be truncated and replaced by a finite series, i.e.

$$e^{-iH_F\Delta t/\hbar} = \sum_{k=0}^{k_{max}} \left(-\frac{i\Delta t}{\hbar}\right)^k \cdot \frac{H_F^k}{k!}. \tag{6.39}$$

Inserting Eq. (6.39) in (6.38) leads to

$$\begin{aligned} U_{\alpha\beta}(k\Delta t,(k-1)\Delta t) &= \sum_{n=-\infty}^{\infty} \langle\langle \alpha n | \sum_{k=0}^{k_{max}} \left(-\frac{i\Delta t}{\hbar}\right)^k \cdot \frac{H_F^k}{k!} | \beta 0 \rangle\rangle e^{in\omega k\Delta t} \\ &= \sum_{n=-\infty}^{\infty} e^{in\omega k\Delta t} \sum_{k=0}^{k_{max}} \frac{1}{k!} \left(-\frac{i\Delta t}{\hbar}\right)^k \langle\langle \alpha n | H_F^k | \beta 0 \rangle\rangle. \end{aligned} \tag{6.40}$$

Each $\langle\langle \alpha n | H_F^k | \beta 0 \rangle\rangle$ is an element in the column $m = 0$ of the matrix representation of the Floquet Hamiltonian's k-th power $\langle\langle \alpha n | H_F^k | \beta m \rangle\rangle$, i.e. $\langle\langle \alpha n | H_F^k | \beta 0 \rangle\rangle$ is a (block) matrix in the Hilbert space $\mathcal{R}$. For $k = 0$ we get

$$\begin{aligned} \langle\langle \alpha n | H_F^0 | \beta 0 \rangle\rangle &= \langle\langle \alpha n | \mathbf{1} | \beta 0 \rangle\rangle \\ &= \delta_{\alpha\beta}\delta_{n0}, \end{aligned} \tag{6.41}$$

i.e. the unit matrix in $\mathcal{R}$ for $n = 0$ and the zero matrix elsewise. For $k = 1$ we have according to Eq. (6.34)

$$\langle\langle \alpha n | H_F | \beta 0 \rangle\rangle = H_{\alpha\beta}^{(n)} + n\hbar\omega\delta_{\alpha\beta}\delta_{n0}. \tag{6.42}$$

Since the Kronecker delta δ_{n0} is zero except for $n = 0$ the expression can be simplified to

$$\langle\langle \alpha n | H_F | \beta 0 \rangle\rangle = H^{(n)}_{\alpha\beta}, \tag{6.43}$$

that is for $k = 1$ the matrices are given by the Hamiltonian's n-th Fourier component (Eq. (6.31)) represented in the basis of the Hilbert space $\mathcal{R}$. For higher powers $k \geq 2$ the matrices $\langle\langle \alpha n | H_F^k | \beta 0 \rangle\rangle$ can be calculated by means of the following scheme [94]. Evidently, the matrix $\langle\langle \alpha n | H_F^k | \beta m \rangle\rangle$ is given by the basis representation of the k-th power of the Floquet Hamiltonian H_F. It can be obtained by raising the Floquet matrix $[H_F] = \langle\langle \alpha n | H_F | \beta m \rangle\rangle$ to the k-th power, which can be calculated by multiplying $[H_F]$ with the power $k-1$ of the Floquet matrix, i.e.

$$[H_F^k] = [H_F] \cdot [H_F^{k-1}] \tag{6.44}$$

In order to simplify the consideration we forget for the time being that each matrix element of $[H_F^k]$, $[H_F]$ and $[H_F^{k-1}]$ is again a matrix and write in a short form $[H_F^k]_{nm}$, $[H_F]_{nm}$ and $[H_F^{k-1}]_{nm}$. From Eq. (6.40) we know that only the elements in the column $m = 0$ are needed. According to the formula for matrix products

$$c_{ij} = \sum_k a_{ik} \cdot b_{kj} \tag{6.45}$$

these elements can be calculated as

$$[H_F^k]_{n0} = \sum_{m=-\infty}^{\infty} [H_F]_{nm} \cdot [H_F^{k-1}]_{m0}, \tag{6.46}$$

where the sum runs from $-\infty$ to ∞ because we multiply two infinite matrices. Now we take into account that the $[H_F]_{nm}$, $[H_F^{k-1}]_{nm}$, $[H_F^k]_{nm}$ are matrices and go back to the notation in the composite Hilbert space. For instance, the element $[H_F]_{nm}$ in the n-th row and the m-th column of the Floquet matrix $[H_F]$ is the (block) matrix $\langle\langle \alpha n | H_F | \beta m \rangle\rangle$ in the Hilbert space $\mathcal{R}$, i.e. $[H_F]_{nm} = \langle\langle \alpha n | H_F | \beta m \rangle\rangle$. Correspondingly, the other elements are the matrices $[H_F^k]_{n0} = \langle\langle \alpha n | H_F^k | \beta 0 \rangle\rangle$ and $[H_F^{k-1}]_{m0} = \langle\langle \alpha m | H_F^{k-1} | \beta 0 \rangle\rangle$. Inserting these expressions into Eq. (6.46) and considering the formula for $\langle\langle \alpha n | H_F | \beta m \rangle\rangle$ given by Eq. (6.34) yields the following recursion formula for $\langle\langle \alpha n | H_F^k | \beta 0 \rangle\rangle$

$$\langle\langle \alpha n | H_F^k | \beta 0 \rangle\rangle = \sum_{m=-\infty}^{\infty} \left(H^{(n-m)}_{\alpha\beta} + n\hbar\omega\delta_{\alpha\beta}\delta_{nm} \right) \cdot \langle\langle \alpha m | H_F^{k-1} | \beta 0 \rangle\rangle. \tag{6.47}$$

Note that this formula is for the block matrices in $\mathcal{R}$. The Kronecker delta δ_{nm} in Eq. (6.47) is zero except for $n = m$ which yields finally [94]

$$\langle\langle \alpha n | H_F^k | \beta 0 \rangle\rangle = \sum_{m=-\infty}^{\infty} H^{(n-m)}_{\alpha\beta} \cdot \langle\langle \alpha m | H_F^{k-1} | \beta 0 \rangle\rangle + n\hbar\omega\delta_{\alpha\beta} \cdot \langle\langle \alpha n | H_F^{k-1} | \beta 0 \rangle\rangle. \tag{6.48}$$

Let us discuss a very nice feature of this recursion formula. From Eq. (6.40) we know that for the computation of the time-evolution operator the storage of the complete matrices of the sequential powers of the Floquet Hamiltonian $\langle\langle \alpha n | H_F^k | \beta m \rangle\rangle$ is not necessary. Instead, the

elements in the column $m = 0$ are sufficient, i.e. $\langle\langle \alpha n|H_F^k|\beta 0\rangle\rangle$. Fortunately, the recursion formula (6.48) reveals that for the calculation of the k-th power elements $\langle\langle \alpha n|H_F^k|\beta 0\rangle\rangle$ we need from the matrices belonging to the power $k-1$ only the elements in the column $m = 0$, that is $\langle\langle \alpha n|H_F^{k-1}|\beta 0\rangle\rangle$, which reduces significantly the memory requirements on a computer [94]. Furthermore, the sum over m in Eq. (6.48) can be truncated for the following reason. In general, the strength of the Fourier components of the Hamiltonian $H^{(n)}(x)$ (Eq. (6.31)), which is defined by

$$c_n = \int_{-\infty}^{\infty} |H^{(n)}(x)|dx, \tag{6.49}$$

decreases with increasing n. Accordingly, within numerical precision it can be assumed that $H^{(n)}(x) = 0$ holds for $|n| > n_{max}$. In this case the sum over m in the recursion formula (6.48) runs for $k = 2$ from $m = -n_{max}$ to n_{max} because for $|m| > n_{max}$ we have $\langle\langle \alpha m|H_F|\beta 0\rangle\rangle = H_{\alpha\beta}^{(m)} = \langle\alpha|H^{(m)}(x)|\beta\rangle = 0$. Additionally, we get from the Eq. (6.48) that the elements of the squared Floquet Hamiltonian $\langle\langle \alpha n|H_F^2|\beta 0\rangle\rangle$ are zero if $|n| > 2n_{max}$ since for larger n the terms $H_{\alpha\beta}^{(n-m)}$ in the sum over m vanishes [94]. In general, for an arbitrary power $k \geq 2$ the sum runs from $m = -(k-1)n_{max}$ to $(k-1)n_{max}$ and we have $\langle\langle \alpha n|H_F^k|\beta 0\rangle\rangle = 0$ if $|n| > k \cdot n_{max}$, which can be understood straightforwardly. According to the previous section the Floquet matrix $[H_F]$ is a bandmatrix when the condition $H^{(n)}(x) = 0$ holds for $|n| > n_{max}$. If $[H_F]$ is raised to a given power, the number of its nonzero secondary diagonals thus doubles, triples, etc. Consequently, for $k \geq 2$ the recursion formula (6.48) can be written as [94]

$$\langle\langle \alpha n|H_F^k|\beta 0\rangle\rangle = \sum_{m=-(k-1)n_{max}}^{(k-1)n_{max}} H_{\alpha\beta}^{(n-m)} \cdot \langle\langle \alpha m|H_F^{k-1}|\beta 0\rangle\rangle + n\hbar\omega\delta_{\alpha\beta} \cdot \langle\langle \alpha n|H_F^{k-1}|\beta 0\rangle\rangle \tag{6.50}$$

Evidently, the formula for the small step time-evolution operators (6.40) can be simplified to

$$U_{\alpha\beta}(k\Delta t, (k-1)\Delta t) = \sum_{n=-k_{max}\cdot n_{max}}^{k_{max}\cdot n_{max}} e^{in\omega k\Delta t} \sum_{k=0}^{k_{max}} \frac{1}{k!}\left(-\frac{i\Delta t}{\hbar}\right)^k \langle\langle \alpha n|H_F^k|\beta 0\rangle\rangle, \tag{6.51}$$

since for $|n| > k_{max} \cdot n_{max}$ the elements $\langle\langle \alpha n|H_F^k|\beta 0\rangle\rangle$ in the truncated exponential series vanish. Finally, the one-period time-evolution operator $U_{\alpha\beta}(T, 0)$ is obtained by multiplying the sequential $U_{\alpha\beta}(k\Delta t, (k-1)\Delta t)$. Afterwards, the matrix $U_{\alpha\beta}(T, 0)$ is diagonalized which yields according to Eq. (6.25) the Floquet modes $\Phi_\lambda(x, 0)$ and their corresponding quasienergies ϵ_λ. Consequently, the next question is which basis $\{|\alpha\rangle\}$ to choose for the Hilbert space $\mathcal{R}$. In the following section this problem is discussed.

6.6 Bloch theory

As previously mentioned, the Gaussian barriers are equipped with a periodic phase gradient, i.e. the local phase shifts obey $\varphi_{i+n_p} = \varphi_i$ with n_P being the period of the phase gradient. Obviously, this gives rise to a spatial periodicity of the Hamiltonian $H(x + L, t)$, where $L = n_P \cdot D$ is the spatial period with D being the barriers' equilibrium distance. In the simultaneous presence of a spatial translation invariance and a temporal periodicity the Bloch

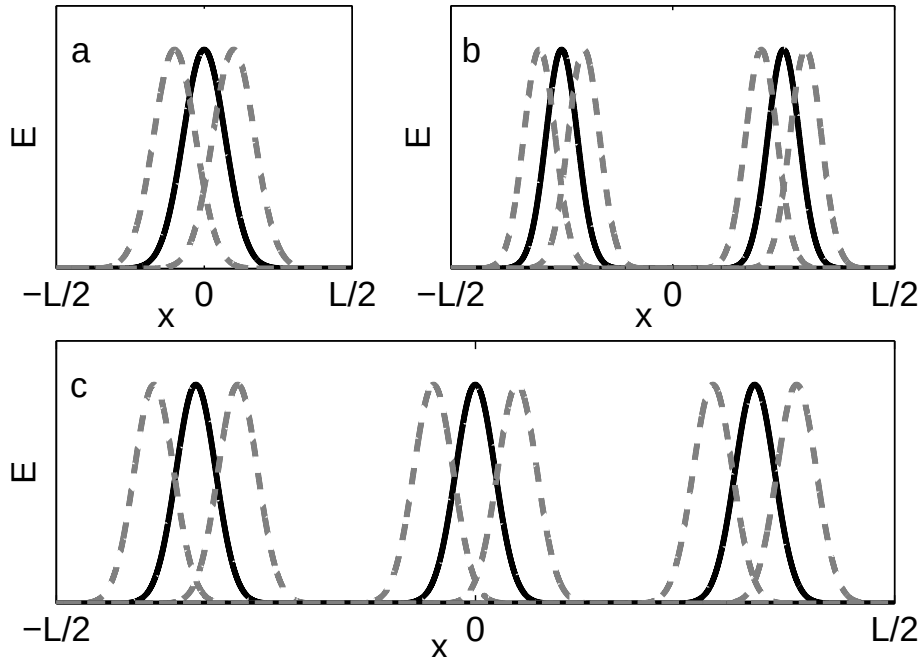

Figure 6.2: Sketch of the lattice's unit cell for phase gradient of period one (a), two (b) and three (c).

theorem applies to the Floquet modes, that is

$$\Phi_{\lambda,\kappa}(x,t) = e^{i\kappa x}\varphi_{\lambda,\kappa}(x,t), \tag{6.52}$$

with quasimomentum $\kappa \in [-\pi/L, \pi/L]$ so that $\Phi_{\lambda,\kappa}(x,t)$ and $\epsilon_{\lambda,\kappa}$ carry besides λ another index κ. $\varphi_{\lambda,\kappa}(x,t)$ is a function which has the same spatial period as the Hamiltonian $\varphi_{\lambda,\kappa}(x+L,t) = \varphi_{\lambda,\kappa}(x,t)$. Due to the spatial periodicity the lattice can be reduced to a unit cell. In Fig. 6.2 a sequence is shown how the unit cell is defined for phase gradients of different periods, e.g. for the lattice of uniformly oscillating barriers ($n_P = 1$), the unit cell contains only one barrier (Fig. 6.2 (a)). Apparently, the number of barriers in a unit cell is equal to the period of the phase gradient n_P. Moreover, the equilibrium positions of the barriers are always symmetric with respect to $x = 0$ such that the unit cell extends from $-L/2$ to $L/2$. For the basis of the unit cell we choose the following set of functions $\{|\alpha_\kappa\rangle\}$

$$|\alpha_\kappa\rangle = \frac{1}{\sqrt{L}} e^{i(\frac{2\pi}{L}\alpha+\kappa)x}, \tag{6.53}$$

where $\alpha \in \mathbb{Z}$ and $\kappa \in [-\pi/L, \pi/L]$ is the quasimomentum. It is easy to see that the set $\{|\alpha_\kappa\rangle\}$ forms an orthonormal basis for the unit cell since

$$\langle\alpha_\kappa|\beta_\kappa\rangle = \frac{1}{L}\int_{-L/2}^{L/2} e^{i\frac{2\pi}{L}(\beta-\alpha)x}dx = \delta_{\alpha\beta}. \tag{6.54}$$

Additionally, the basis fulfills the Bloch theorem given by Eq. (6.52) because the functions $|\alpha_\kappa\rangle$ can obviously be written as $|\alpha_\kappa\rangle = e^{i\kappa x}|\alpha\rangle$, where $|\alpha\rangle$ are plane-waves having the period

L, i.e.

$$|\alpha\rangle = \frac{1}{\sqrt{L}} e^{i\frac{2\pi}{L}\alpha x}. \tag{6.55}$$

Thus, if for fixed κ the one-period time-evolution operator $U_{\alpha\beta}(T,0)$ of the unit cell is represented in the basis $\{|\alpha_\kappa\rangle\}$, the Floquet modes obtained by diagonalizing $U_{\alpha\beta}(T,0)$ will obey the Bloch theorem (6.52) because the basis itself does. In the following the quasimomentum is indicated as a upper index in the time-evolution operator $U^\kappa_{\alpha\beta}(T,0)$. Consequently, the eigenvalue problem (6.25) for the Floquet modes and their corresponding quasienergies becomes

$$U^\kappa_{\alpha\beta}(T,0)\Phi_{\lambda,\kappa}(x,0) = e^{-i\epsilon_{\lambda,\kappa}T/\hbar}\Phi_{\lambda,\kappa}(x,0), \tag{6.56}$$

where the quasimomentum κ is a continuous parameter. Note that $U^\kappa_{\alpha\beta}(T,0)$ is the one-period time-evolution operator of the unit cell for a certain value of κ. $U_{\alpha\beta}(T,0)$ of the complete lattice can be imagined as a blockdiagonal matrix whose blocks are the $U^\kappa_{\alpha\beta}(T,0)$, i.e. the time-evolution operators of the unit cell represented in the basis $\{|\alpha_\kappa\rangle\}$ for a fixed κ. Before we proceed to the question how an arbitrary initial wavefunction can be propagated in the lattice the computation of $U^\kappa_{\alpha\beta}(T,0)$ is explained in the following section.

6.7 Unit cell time-evolution operator

In order to calculate the time-evolution operator over one-period $U^\kappa_{\alpha\beta}(T,0)$ we have to determine the Fourier components of the Hamiltonian $H(x,t)$ of the unit cell belonging to the lattice, i.e.

$$H^{(n)}(x) = \frac{1}{T}\int_0^T dt H(x,t)e^{-in\omega t}. \tag{6.57}$$

Inserting in (6.57) the Hamiltonian (Eq. (6.2)) yields

$$H^{(n)}(x) = \begin{cases} -\frac{\hbar^2}{2m}\frac{\partial^2}{\partial x^2} + V^{(n)}(x) & \text{if } n = 0 \\ V^{(n)}(x) & \text{else,} \end{cases} \tag{6.58}$$

where $V^{(n)}(x)$ is the n-th Fourier component of the potential of the unit cell given by

$$V^{(n)}(x) = \frac{1}{T}\int_0^T dt V(x,t)e^{-in\omega t}. \tag{6.59}$$

According to the previous section the potential of the unit cell $V(x,t)$ is given by

$$V(x,t) = \sum_{i=1}^{n_P} V_0 \exp\left(-\left(\frac{x - x_{0,i} - f_i(t)}{\delta}\right)^2\right), \tag{6.60}$$

where n_P is the phase period and $f_i(t) = C\cos(\omega(t+t_0)+\varphi_i)$ is the driving law (Fig. 6.1 and 6.2). In order to ensure that the barriers are always placed symmetrically with respect to the origin of the unit cell $x = 0$, the equilibrium position $x_{0,i}$ has to be chosen such that

$$x_{0,i} = (i - n_P)\frac{D}{2}, \tag{6.61}$$

where D is the equilibrium distance. For example, the unit cell belonging to the lattice of uniformly oscillating barriers, i.e. $n_P = 1$, $\varphi_i = 0$, contains one barrier placed at $x_{0,1} = 0$ (Fig. 6.2 (a)). For a lattice with a phase gradient of period three, i.e. $n_P = 3$, $\varphi_{i+n_P} = \varphi_i$, the equilibrium positions of the barriers forming the unit cell are $x_{0,1} = -D$, $x_{0,2} = 0$ and $x_{0,3} = D$ (Fig. 6.2 (b)). Let us now discuss how to calculate the Fourier series of the potential of the unit cell $V(x,t)$ for arbitrary phase periods n_P, initial phase t_0 and phase shifts φ_i. To this end we start by determining the Fourier components of a single laterally oscillating Gaussian potential and subsequently it is shown how this result can be generalized. Obviously, the potential of one Gaussian potential $V_{\mathrm{SB}}(x,t)$ with lateral driving $f(t) = C\cos(\omega(t+t_0)+\varphi_i)$ is given by

$$V_{\mathrm{SB}}(x,t) = V_0 \exp\left(-\left(\frac{x-f(t)}{\delta}\right)^2\right) \tag{6.62}$$

Its n-th Fourier component is

$$\begin{aligned} V_{\mathrm{SB}}^{(n)}(x) &= \frac{1}{T}\int_0^T dt V_{\mathrm{SB}}(x,t)e^{-in\omega t} \\ &= \frac{V_0}{T}\int_0^T dt \exp\left(-\left(\frac{x-C\cos(\omega(t+t_0)+\varphi_i)}{\delta}\right)^2\right)e^{-in\omega t} \end{aligned} \tag{6.63}$$

Let us now assume that $t_0 = \varphi_i = 0$ and consider $\varphi_i \neq 0$, $t_0 \neq 0$ afterwards, i.e.

$$\begin{aligned} V_{\mathrm{SB}}^{(n)}(x) &= \frac{V_0}{T}\int_0^T dt \exp\left(-\left(\frac{x-C\cos(\omega t)}{\delta}\right)^2\right)e^{-in\omega t} \\ &= \frac{V_0}{T}\int_0^T dt \exp\left(-\left(\frac{x-C\cos(\omega t)}{\delta}\right)^2\right)(\cos(n\omega t) - i\sin(n\omega t)) \\ &= \frac{V_0}{T}\int_0^T dt \exp\left(-\left(\frac{x-C\cos(\omega t)}{\delta}\right)^2\right)\cos(n\omega t) \end{aligned} \tag{6.64}$$

where we have used in the last line that due to the cosine-driving the exponential is symmetric in the variable t whereas sine is antisymmetric, i.e. the integrand is antisymmetric, too. Evidently, the integral over one period of a antisymmetric periodic function vanishes. Additionally, one can make the substitution $\tau = \omega t$ yielding finally

$$V_{\mathrm{SB}}^{(n)}(x) = \frac{V_0}{2\pi}\int_0^{2\pi} d\tau \exp\left(-\left(\frac{x-C\cos(\tau)}{\delta}\right)^2\right)\cos(n\tau). \tag{6.65}$$

Let us now generalize to the case $t_0 \neq 0$, $\varphi_i \neq 0$, i.e. we determine the n-th Fourier component of a single, laterally oscillating Gaussian with arbitrary initial phase and local phase shift. Obviously, the Fourier series of the single laterally oscillating Gaussian potential $V_{\mathrm{SB}}(x,t)$ is given by

$$V_{\mathrm{SB}}(x,t) = \sum_{n=-\infty}^{\infty} V_{\mathrm{SB}}^{(n)}(x)e^{in\omega t} \tag{6.66}$$

By means of the transformation

$$t \to t + t_0 + \frac{\varphi_i}{\omega} \tag{6.67}$$

we get to the case of nonzero t_0, φ_i and the Fourier series becomes

$$V_{\mathrm{SB}}(x, t + t_0 + \frac{\varphi_i}{\omega}) = \sum_{n=-\infty}^{\infty} V_{\mathrm{SB}}^{(n)}(x) e^{in(\omega(t+t_0)+\varphi_i)} \tag{6.68}$$

Accordingly, putting t_0 to a non-zero value and giving the barrier a phase shift φ_i leads to a complex phase shift of the Fourier component, i.e.

$$\tilde{V}_{\mathrm{SB}}^{(n)}(x) = V_{\mathrm{SB}}^{(n)}(x) e^{in(\omega t_0+\varphi_i)}. \tag{6.69}$$

By means of this result we can now construct the Fourier components for the unit cell potential. Due the fact that the Gaussian potentials are localized the Fourier series of a sum of potentials can be constructed by a superposition of the single barrier expressions. For the n-th Fourier component $V^{(n)}(x)$ of the unit cell potential for a lattice with phase period n_P this yields

$$V^{(n)}(x) = \sum_{i=1}^{n_P} V_{\mathrm{SB}}^{(n)}(x - x_{0,i}) e^{in(\omega t_0+\varphi_i)}, \tag{6.70}$$

where the sum runs over the number of barriers in the unit cell and $V_{\mathrm{SB}}^{(n)}(x - x_{0,i})$ is the n-th single barrier Fourier component given by Eq. (6.65).

Let us now represent $V^{(n)}(x)$ in the basis of the unit cell $\{|\alpha_\kappa\rangle\}$, i.e. $V_{\alpha\beta}^{(n)} = \langle\alpha_\kappa|V^{(n)}(x)|\beta_\kappa\rangle$, which yields

$$\begin{aligned} V_{\alpha\beta}^{(n)} &= \frac{1}{L}\int_{-L/2}^{L/2} dx V^{(n)}(x) e^{i\frac{2\pi}{L}(\beta-\alpha)x} \\ &= \frac{1}{L}\int_{-L/2}^{L/2} dx \sum_{i=1}^{n_P} V_{\mathrm{SB}}^{(n)}(x - x_{0,i}) e^{in(\omega t_0+\varphi_i)} e^{i\frac{2\pi}{L}(\beta-\alpha)x}, \end{aligned} \tag{6.71}$$

where the Fourier component given by Eq. (6.70) has been inserted in the second line. Since the Gaussian potentials forming the unit cell are localized, i.e. there is no significant overlap, the sum and integration can be interchanged, that is

$$V_{\alpha\beta}^{(n)} = \sum_{i=1}^{n_P} \frac{1}{L}\int_{-L/2}^{L/2} dx V_{\mathrm{SB}}^{(n)}(x - x_{0,i}) e^{in(\omega t_0+\varphi_i)} e^{i\frac{2\pi}{L}(\beta-\alpha)x} \tag{6.72}$$

By means of the transformation $\tilde{x} = x - x_{0,i}$ we get

$$V_{\alpha\beta}^{(n)} = \sum_{i=1}^{n_P} \frac{1}{L}\int_{-L/2}^{L/2} d\tilde{x} V_{\mathrm{SB}}^{(n)}(\tilde{x}) e^{in(\omega t_0+\varphi_i)} e^{i\frac{2\pi}{L}(\beta-\alpha)(\tilde{x}+x_{0,i})}. \tag{6.73}$$

The bounds of the integration do not change because the Gaussian potentials are zero outside

of the unit cell extending from $-L/2$ to $L/2$. Finally, we get

$$\begin{aligned} V_{\alpha\beta}^{(n)} &= \sum_{i=1}^{n_P} \frac{1}{L} \int_{-L/2}^{L/2} d\tilde{x} V_{\mathrm{SB}}^{(n)}(\tilde{x}) e^{i\frac{2\pi}{L}(\beta-\alpha)\tilde{x}} e^{i(n(\omega t_0+\varphi_i)+\frac{2\pi}{L}(\beta-\alpha)x_{0,i})} \\ &= \sum_{i=1}^{n_P} \tilde{V}_{\alpha\beta}^{(n)} e^{i(n(\omega t_0+\varphi_i)+\frac{2\pi}{L}(\beta-\alpha)x_{0,i})}, \end{aligned} \tag{6.74}$$

where $\tilde{V}_{\alpha\beta}^{(n)} = \langle \alpha_\kappa | V_{\mathrm{SB}}^{(n)}(x) | \beta_\kappa \rangle$ is the matrix representation of the n-th Fourier component corresponding to a single oscillating barrier $V_{\mathrm{SB}}^{(n)}(x)$ (Eq. (6.65)) in the unit cells' basis $\{|\alpha_\kappa\rangle\}$. Obviously, the matrix representation of the n-th Fourier component belonging to the complete potential of the unit cell $V_{\alpha\beta}^{(n)}$ can be determined in the following way. First, we represent the single barrier expression $V_{\mathrm{SB}}^{(n)}(x)$ given by Eq. (6.65) in the basis of the unit cell yielding $\tilde{V}_{\alpha\beta}^{(n)}$. Afterwards, $V_{\alpha\beta}^{(n)}$ is calculated by multiplying $\tilde{V}_{\alpha\beta}^{(n)}$ with a sum of complex phase factors $e^{i(n(\omega t_0+\varphi_i)+\frac{2\pi}{L}(\beta-\alpha)x_{0,i})}$ originating from the initial phase t_0, the local phase shifts φ_i and the nonzero equilibrium positions $x_{0,i}$ of the barriers constituting the unit cell.

With $V_{\alpha\beta}^{(n)}$ we can now give the matrix representation of the n-th Fourier component of the Hamiltonian $H(x,t)$ of the unit cell, i.e. $H_{\alpha\beta}^{(n)} = \langle \alpha_\kappa | H^{(n)}(x) | \beta_\kappa \rangle$. In the chosen basis $\{|\alpha_\kappa\rangle\}$ the operator of the kinetic energy is a diagonal matrix which yields

$$H_{\alpha\beta}^{(n)} = \begin{cases} \frac{\hbar^2\left(\frac{2\pi}{L}\alpha+\kappa\right)^2}{2m}\delta_{\alpha\beta} + V_{\alpha\beta}^{(n)} & \text{if } n=0 \\ V_{\alpha\beta}^{(n)} & \text{else,} \end{cases} \tag{6.75}$$

Now the time-evolution operator of the unit-cell $U_{\alpha\beta}^{\kappa}(T,0)$ for a fixed κ can be calculated according to method presented in Sec. 6.5.

Let us briefly comment on why we have chosen Gaussian potentials instead of the rectangular barriers. According to the discussion in the previous sections it is obvious that the numerical effort, i.e. computation time and memory requirements, depends crucially on the convergence of the Fourier series of the potential $V(x,t)$. Faster convergence implies less memory requirements for storing the matrices on a computer etc. Consequently, it is feasible to study how $V^{(n)}(x)$ depends on n. To this end we calculate the average of the n-th Fourier component of a single oscillating Gaussian potential $V_{\mathrm{SB}}^{(n)}(x)$ in the following way

$$c_n = \int_{-\infty}^{\infty} dx |V_{\mathrm{SB}}^{(n)}(x)| \tag{6.76}$$

In Fig. 6.3 the first four Fourier coefficients $V_{\mathrm{SB}}^{(n)}(x)$ of the single laterally oscillating Gaussian potential are shown for the following parameter choice $V_0 = 1$, , $C = 1$, $\delta = 1/2$. In Fig. 6.4 we show c_n as a function of n in semilogarithmic plot. As we see, c_n decreases exponentially with n. Since for $n \neq 0$ the Fourier coefficients of the Hamiltonian and the potential are identical, it follows that $|H^{(n)}(x)|$ decays exponentially, too. Conversely, for a laterally oscillating rectangular barrier, one gets only linear decay, i.e. $|H^{(n)}(x)| \sim \frac{1}{|n|}$ [95–97], which can be traced back to the discontinuous form of the rectangular potential. Through the

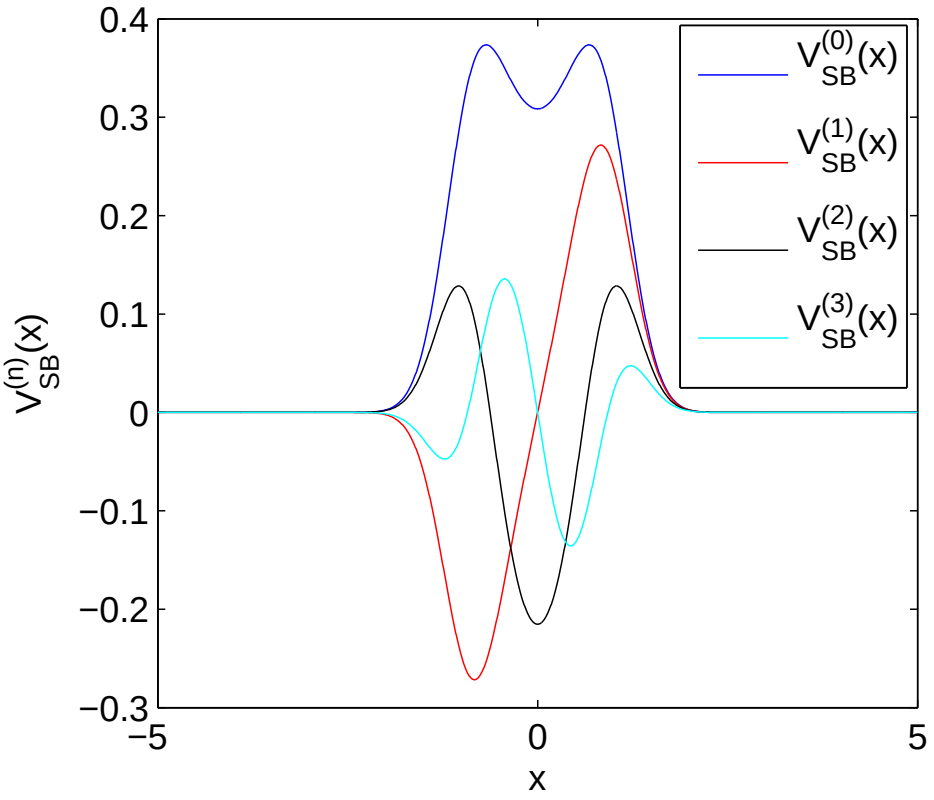

Figure 6.3: First four Fourier coefficients of the laterally oscillating Gaussian potential $V_{\mathrm{SB}}(x,t) = V_0 \exp\left(-\left(\frac{x-C\cos(\omega t)}{\delta}\right)^2\right)$ for $\delta = 1/2$, $C = 1$,$V_0 = 1$.

lateral movement this discontinuity becomes "transfered" to the time-domain leading to the exceedingly slow decrease. When calculating the time-evolution operator this implies that for a laterally oscillating rectangular barrier the sum over the Fourier components has to be performed over a broader range than for a laterally oscillating Gaussian barrier. Consequently, the Gaussian potential makes the numerical algorithm much more efficient in terms of memory requirements on a computer. Due to the fact that the effects observed for the classical regime do not depend on the shape of the potential, we have decided due to aforementioned reasons to consider Gaussian potentials.

6.8 Time-evolution of wavefunctions and observables

Before we proceed to the discussion concerning how an arbitrary initial state can be propagated in time let us briefly comment on the impact of the initial phase t_0 of the driving on the dynamics. From the previous discussion we have learned that t_0 enters in the calculation of the one-period time evolution operator, i.e. $U^{\kappa}_{\alpha\beta}(T,0)$ depends on t_0. Accordingly, the Floquet modes obtained by diagonalizing the matrix $U^{\kappa}_{\alpha\beta}(T,0)$ depend as well on t_0, so that we write in the following $\Phi_{\lambda,\kappa}(x,t,t_0)$.

From the discussion on Floquet theory we know that the Floquet modes $\Phi_{\lambda,\kappa}(x,t,t_0)$ of the

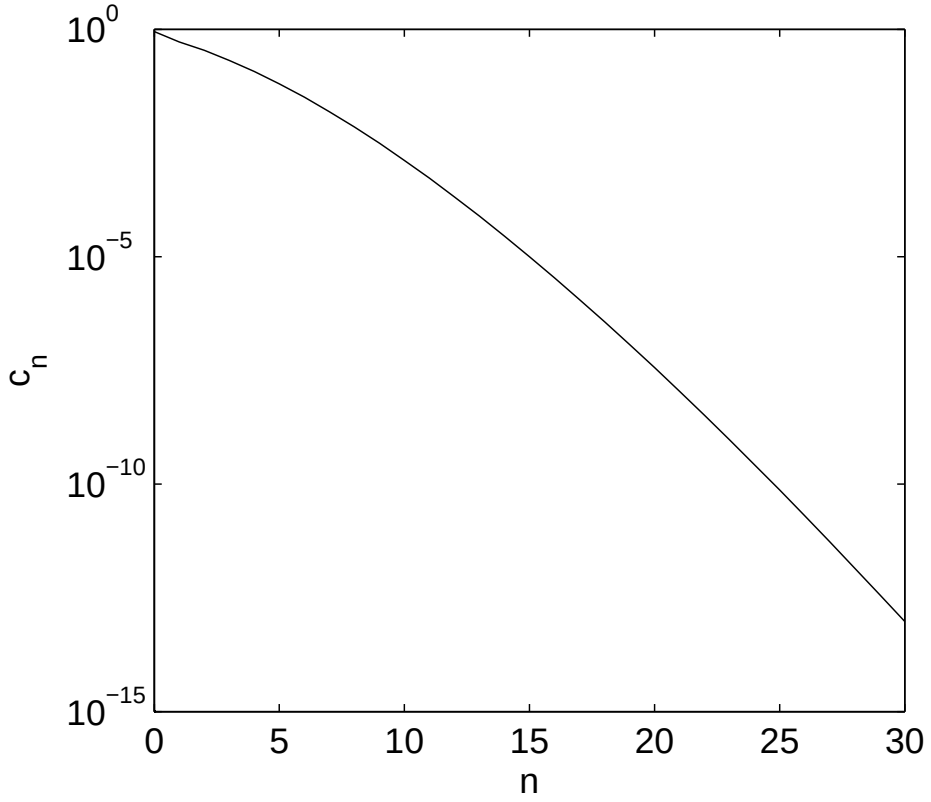

Figure 6.4: Average of the Fourier coefficients c_n of a harmonically oscillating Gaussian barrier with parameters $V_0 = 1, C = 1, \delta = 1/2$.

first Brillouin-zone form an orthonormal basis of the Hilbert space $\mathcal{R}$ for fixed time t. Due to the translation invariance $H(x + L, t) = H(x, t)$ of the Hamiltonian, one can think about $\mathcal{R}$ being sliced into subspaces characterized by the quasimomentum $\kappa \in [-\pi/L, \pi/L]$ [88]. Consequently, the evolution of an arbitrary initial state is obtained by writing its wavefunction $\Psi(x, t)$ for fixed quasimomentum κ and time t as a superposition of the Floquet modes and average subsequently over κ [51], that is

$$\Psi(x,t) = \frac{L}{2\pi} \int_{-\pi/L}^{\pi/L} d\kappa \sum_{\lambda} c_{\lambda,\kappa}(t_0) e^{-i\epsilon_{\lambda,\kappa} t/\hbar} \Phi_{\lambda,\kappa}(x, t, t_0), \tag{6.77}$$

where the expansion coefficients $c_{\lambda,\kappa}(t_0)$ are given by overlapping the initial wavefunction $\Psi(x, t = 0)$ with the Floquet modes $\Phi_{\lambda,\kappa}(x, t = 0, t_0)$, that is

$$c_{\lambda,\kappa}(t_0) = \int_{-\infty}^{\infty} \Phi^*_{\lambda,\kappa}(x, 0, t_0) \Psi(x, 0) dx. \tag{6.78}$$

As we see, the coefficient $c_{\lambda,\kappa}(t_0)$ depend on the initial phase of the driving. For stroboscopic points in time, which are multiples of the driving period T, Eq. (6.77) can be written due to

the periodicity of the Floquet modes $\Phi_{\lambda,\kappa}(x, mT, t_0) = \Phi_{\lambda,\kappa}(x, 0, t_0)$ as

$$\Psi(x, mT) = \frac{L}{2\pi} \int_{-\pi/L}^{\pi/L} d\kappa \sum_{\lambda} c_{\lambda,\kappa}(t_0) e^{-im\epsilon_{\lambda,\kappa}T/\hbar} \Phi_{\lambda,\kappa}(x, 0, t_0), \tag{6.79}$$

where the $\Phi_{\lambda,\kappa}(x, 0, t_0)$ and their corresponding $\epsilon_{\lambda,\kappa}$ are obtained numerically from Eq. (6.56). By means of expression (6.79) any initial wavefunction can be propagated stroboscopically so that we can study the long-term quantum dynamics.

In order to study the transport properties of the laterally driven lattice the expectation value of the position $\langle x(t) \rangle$ has to calculated which gives [51]

$$\begin{aligned} \langle x(t) \rangle &= \int_{-\infty}^{\infty} dx\, x |\Psi(x, t)|^2 \\ &= v(t_0)t + o(t), \end{aligned} \tag{6.80}$$

where the asymptotic transport velocity $v(t_0)$ can be be expressed very efficiently [51, 60] in the basis of the $\Phi_{\lambda,\kappa}(x, 0, t_0)$ via

$$v(t_0) = \frac{L}{2\pi} \int_{-\pi/L}^{\pi/L} d\kappa \sum_{\lambda} |c_{\lambda,\kappa}(t_0)|^2 v_{\lambda,\kappa}. \tag{6.81}$$

$v_{\lambda,\kappa}$ is the average velocity of a Floquet mode over one period of the driving, i.e.

$$v_{\lambda,\kappa} = \frac{1}{T} \int_0^T dt \langle \Phi_{\lambda,\kappa}(x, t, t_0) | \hat{v} | \Phi_{\lambda,\kappa}(x, t, t_0) \rangle, \tag{6.82}$$

with $\hat{v} = \hat{p}/m$. In general, the average current depends on the initial phase t_0 of the driving because the overlap coefficients $c_{\lambda,\kappa}(t_0)$ of the initial wavefunction with the Floquet modes do. Without averaging the velocity of the Floquet mode over one period we would calculate the velocity of the wavepacket at stroboscopic points in time, which can be nonzero although the average vanishes. By means of a generalization of the Hellmann-Feynman theorem to time-periodic systems $v_{\lambda,\kappa}$ can be related to the slope of the quasienergy bands [46, 51, 89] according to

$$v_{\lambda,\kappa} = \frac{1}{\hbar} \frac{d\epsilon_{\lambda,\kappa}}{d\kappa}, \tag{6.83}$$

i.e. the average transport velocity of the Floquet mode $\Phi_{\lambda,\kappa}(x, t, t_0)$ is given by the first derivative of the corresponding quasienergyband $\epsilon_{\lambda,\kappa}$ with respect to the quasimomentum κ.

6.9 Quasienergy spectrum

According to the previous discussion it is expedient to study the quasienergy bands $\epsilon_{\lambda,\kappa}$ of the driven lattices in order to understand whether transport occurs or not. To this end we solve Eq. (6.56) for discrete values of the quasimomentum $\kappa \in [-\pi/L, \pi/L]$. Let us first start with the quasienergy spectrum of the lattice of uniformly oscillating Gaussian barriers, i.e. setup (a) with $\varphi_i = 0$. In this case the potential $V(x, t)$ is invariant under the generalized parity- and time-reversal transformations given by Eq. (6.5) and (6.6). Fig.

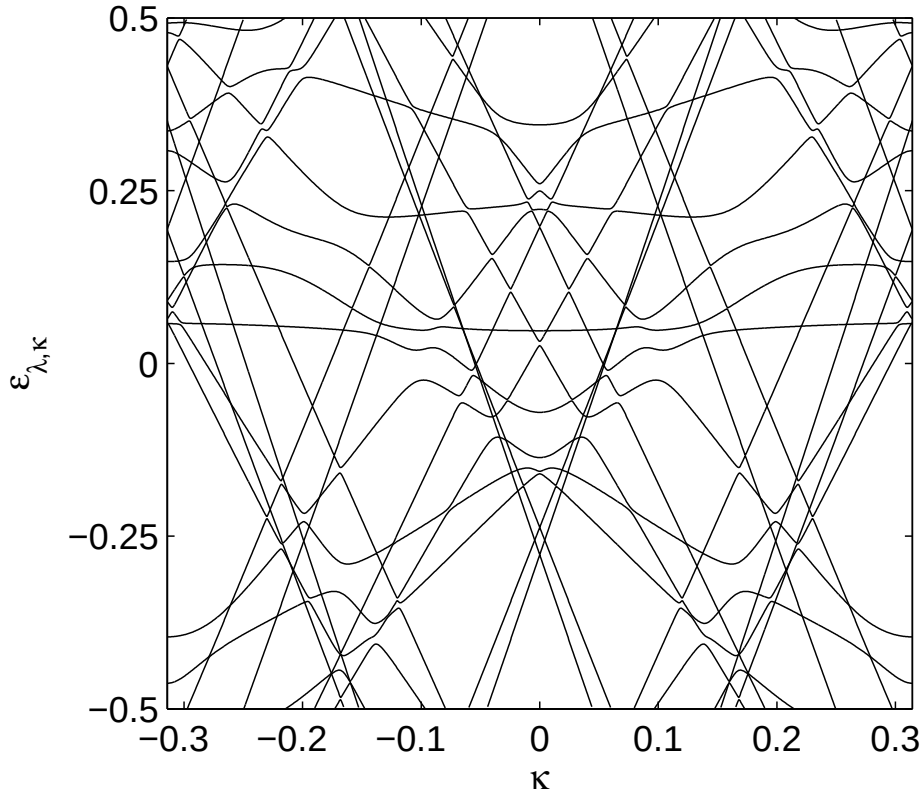

Figure 6.5: Quasienergyspectrum for a lattice of uniformly oscillating Gaussian barriers, i.e. $\varphi_i = 0$ for all i, with $V_0 = 1, \delta = 1/2, C = 1$.

6.5 shows the corresponding quasienergy bands. Due to the fact that both transformations reverse the sign of κ and therefore map the negative branch of the quasienergy band $\epsilon_{\lambda,-\kappa}$ onto the positive part $\epsilon_{\lambda,\kappa}$, the spectrum is mirror-symmetric with respect to $\kappa = 0$, that is $\epsilon_{\lambda,-\kappa} = \epsilon_{\lambda,\kappa}$ [88]. Due to this mirror-symmetry of the quasienergies, the average velocity of the Floquet modes obeys $v_{\lambda,-\kappa} = -v_{\lambda,\kappa}$. Moreover, in the presence of the parity or time-reversal symmetry of the potential the quasienergy bands have zero slope for $\kappa = 0$, i.e. the average velocity of the corresponding Floquet mode vanishes $v_{\lambda,\kappa=0} = 0$ [60]. Indeed, zooming in Fig. 6.5 reveals that at $\kappa = 0$ all bands are flat. Consequently, for the lattice of uniformly oscillating barriers the transport velocity is zero independent from the initial phase t_0 whenever the initial state has no overlap with Floquet modes possessing nonzero quasimomentum [60]. For example, the initial state $\Psi(x, 0) = 1/\sqrt{L}$, corresponding to a uniform distribution of particles over the whole lattice, belongs to the subspace with $\kappa = 0$. However, for more realistic initial states, e.g. when the particle are distributed only over a few unit cells of the lattice, the situation can be drastically different. In this case the initial wavefunction is not restricted in quasimomentum space to the line $\kappa = 0$ but possesses a certain distribution. Therefore, according to formula (6.81) the asymptotic transport is composed of the contributions from the various Floquet modes $\Phi_{\lambda,\kappa}(x, t)$ weighted with their overlap coefficients $c_{\lambda,\kappa}(t_0)$. Depending on the initial phase t_0 of the driving the overlap coefficients of the initial wavefunction $\Psi(x, 0)$ with the Floquet modes can be asymmetric with

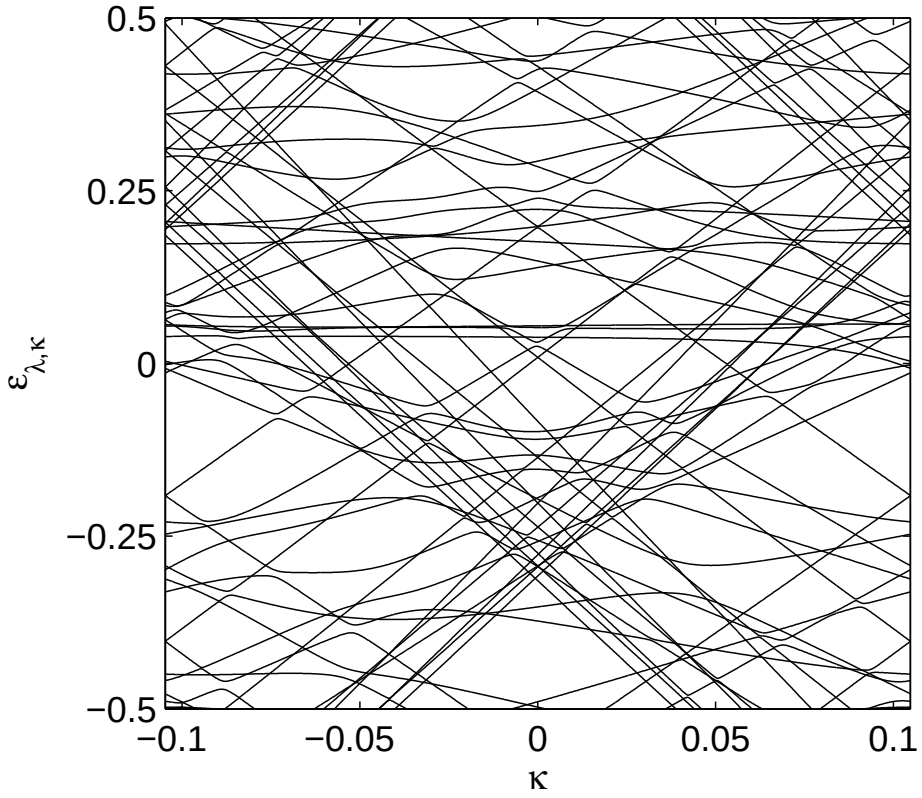

Figure 6.6: Quasienergyspectrum for a lattice of oscillating Gaussian barriers and a linear increasing periodic phase shift of period three, i.e. $\varphi_i = \{\ldots, 0, 2\pi/3, 4\pi/3, \ldots\}$, with $V_0 = 1, \delta = 1/2, C = 1$.

respect to $\kappa = 0$, that is $c_{\lambda,-\kappa}(t_0) \neq c_{\lambda,\kappa}(t_0)$, such that transport can become nonzero [88].

Let us now come to the discussion how breaking the spatiotemporal symmetries given by the generalized parity and time-reversal transformations leaves its hallmark in the appearance of the quasienergy spectrum. To this end we study the quantum dynamics of the lattice of laterally oscillating Gaussian potentials with linear phase gradient of period three, i.e. $\varphi_i = \{\ldots, 0, 2\pi/3, 4\pi/3, \ldots\}$. For this choice of the phase gradient both spatiotemporal symmetries are broken. Fig. 6.6 shows the corresponding quasienergy spectrum. Comparing Fig. 6.5 and 6.6 reveals immediately that the quasienergy bands possesses no longer the previously summarized characteristics. In fact, the spectrum looks for the lattice with the phase gradient much more "chaotic". Due to the asymmetry of the quasienergy band it is plausible to assume that the phase gradient leads in general to the occurrence of a directed transport even if the initial state is restricted to the subspace $\kappa = 0$ [60].

6.10 Husimi representation of Floquet modes

In this section we discuss how a breaking of the spatiotemporal symmetries manifests itself in the Husimi representation of Floquet modes. The Husimi representation is a method to visualize on a coarse-grained scale the distribution of a quantum state in the classical phase

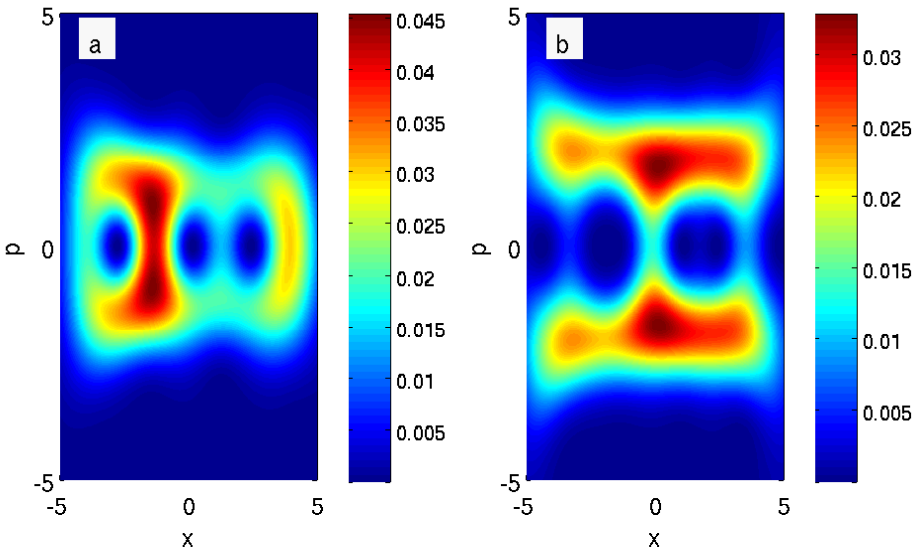

Figure 6.7: Husimi representation of two Floquet modes for zero quasimomentum for the lattice of uniformly oscillating Gaussian potentials $\varphi_i = 0$. The parameters of the potential are $\delta = 1/2$, $C = 1$ and $V_0 = 1$.

space [98, 99]. In general, it is defined by the overlap of a quantum state $|\Psi\rangle$ with a coherent state $|\Phi(x,p)\rangle$ centered at the phase space point (x,p), i.e.

$$\rho(x,p) = \frac{1}{2\pi}|\langle\Phi(x,p)|\Psi\rangle|^2. \tag{6.84}$$

$|\Phi(x,p)\rangle$ is the quantum state of a Gaussian wave packet centered at (x,p), that is

$$\langle\tilde{x}|\Phi(x,p)\rangle = (\pi\sigma^2)^{-1/4}\exp\left(-\frac{(x-\tilde{x})^2}{2\sigma^2} + ip\tilde{x}\right) \tag{6.85}$$

Fig. 6.7 shows $\rho(x,p)$ of two Floquet modes with zero quasimomentum and small average energy for the lattice of uniformly oscillating Gaussian potentials. Evidently, the Husimi representation $\rho(x,p)$ is symmetric with respect to $p = 0$ which reflects the existence of the spatiotemporal symmetries of the potential. In fact, the Husimi representations $\rho(x,p)$ of the other Floquet modes obey as well this mirror-symmetry. Consequently, the Floquet modes with $\kappa = 0$ are non-transporting in the lattice of uniformly oscillating Gaussian barriers. Still, the absence of a current cannot be deduced from this fact because for the transport properties of an arbitrary initial state the Floquet modes with nonzero quasimomentum contribute, too.

Fig. 6.8 shows two Floquet modes with zero quasimomentum in the lattice where the spatiotemporal symmetries of the potential are broken by means of the period three phase gradient $\varphi_i = \{\ldots, 0, 2\pi/3, 4\pi/3, \ldots\}$. Accordingly, the Floquet modes with $\kappa = 0$ get desymmetrized with respect to $p = 0$ such that they carry non-zero average velocity, i.e. $v_{\lambda,\kappa=0} \neq 0$. Contrary to the uniformly driven lattice we would in this case get a current even if the initial state is restricted to the subspace with zero average momentum, e.g. $\Psi(x,0) = 1/\sqrt{L}$. Moreover, although the transport properties for other initial states cannot be judged

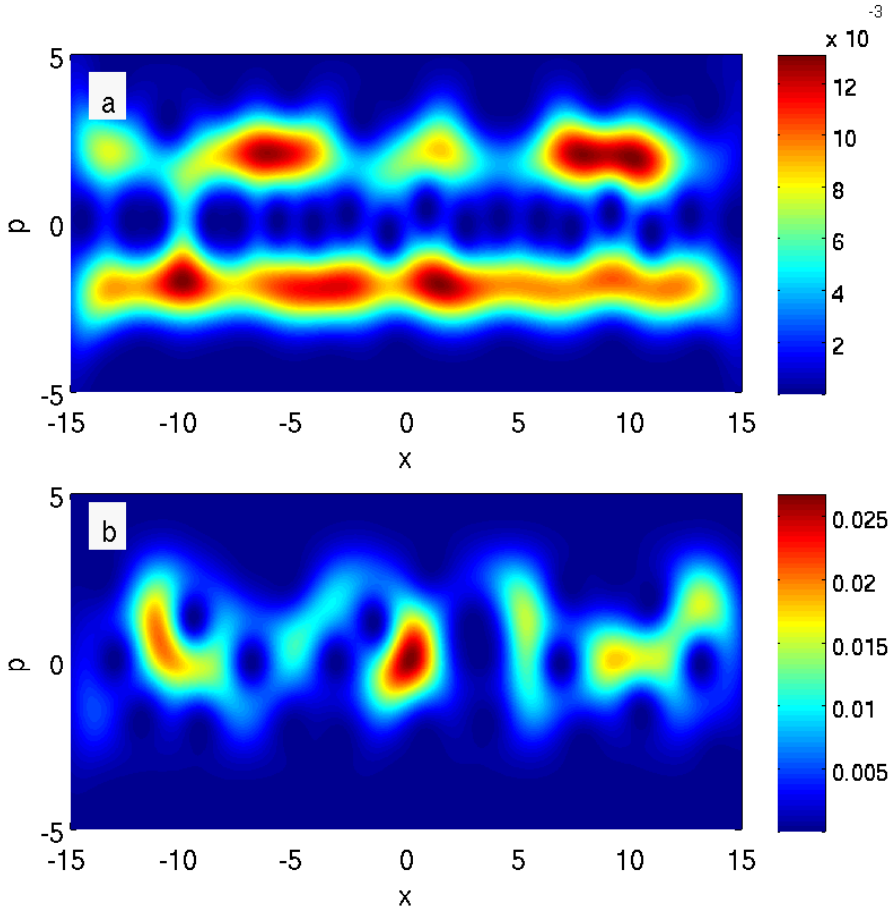

Figure 6.8: Husimi representation of two Floquet modes for zero quasimomentum for the lattice with phase period three $\varphi_i = \{\ldots, 0, 2\pi/3, 4\pi/3, \ldots\}$. The parameters of the potential are $\delta = 1/2$, $C = 1$ and $V_0 = 1$.

prior to the evaluation of Eq. (6.81), it is reasonable to assume that in these cases the current acquires a nonzero value, too.

6.11 Transport

In this section the transport properties of the driven lattices with different phase periods are studied. As initial state we choose a Gaussian wave packet, i.e.

$$\Psi(x, t = 0) = (\pi\sigma^2)^{-1/4} \exp\left(-\frac{x^2}{2\sigma^2}\right), \tag{6.86}$$

where σ is the initial width of the wave function. In the quasimomentum space the wavefunction is symmetric with respect to $\kappa = 0$, that is $\Psi(-\kappa, 0) = \Psi(\kappa, 0)$. By increasing the initial width of the wavefunction in real space σ, the wavefunction becomes narrower in quasimomentum space. Conversely, for a very narrow wave packet in real space its distribution in quasimomentum space is broad. From the previous discussions we know that the lattice of

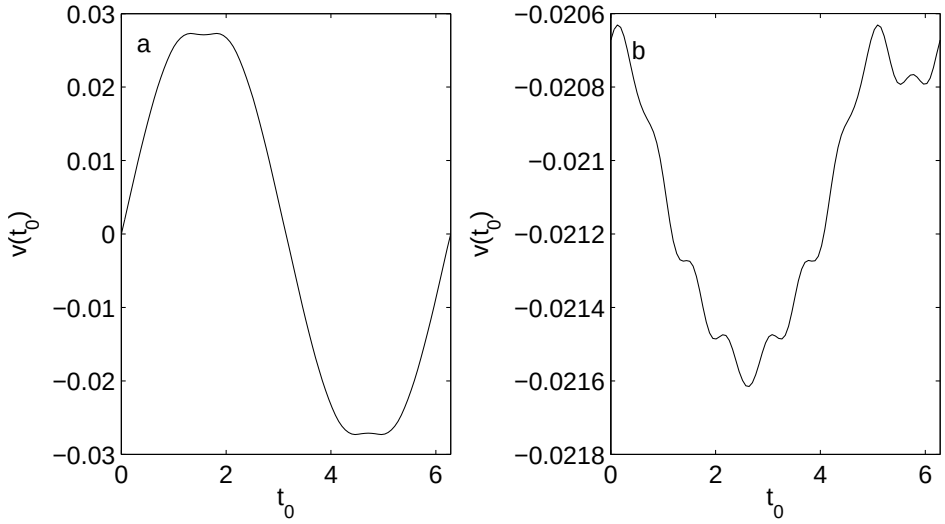

Figure 6.9: Transport velocity as a function of the initial phase for a lattice of uniformly oscillating Gaussian barriers $\varphi_i = 0$ (a) and a lattice with a phase gradient of period three $\varphi_i = \{\ldots, 0, 2\pi/3, 4\pi/3, \ldots\}$ (b). The parameters are $\delta = 1/2$, $C = 1$ and $V_0 = 1$

uniformly oscillating barriers will not show a current for an initial state which is very broad in real space because the Floquet modes with zero quasimomentum are non-transporting in this case. Contrary, a current will be observed in the lattice with the periodic phase gradient since these Floquet modes are desymmetrized. Yet, for a general Gaussian wavepacket possessing the width σ in real space we have to evaluate Eq. (6.81) in order to judge whether or not a current can be observed and in which direction the particles are transported. Figure 6.9 (a) shows for $\omega = 1$ (frequency of the driving) the transport as a function of the initial phase t_0 for a Gaussian wave packet with variance $\sigma = 6\pi$ for the lattice of uniformly oscillating Gaussian potentials, i.e. no phase gradient $\varphi_i = 0$. Although for each t_0 the Hamiltonian of the system possesses the generalized parity and time-reversal symmetry, the current does not vanish in general except at $t_0 = 0, \pi, 2\pi$. As previously mentioned, the appearance of the current is due to the fact that the overlap coefficients of the initial wavefunction with the Floquet modes $c_{\lambda,\kappa}(t_0)$ are not symmetric with respect to $\kappa = 0$ ($c_{\lambda,-\kappa}(t_0) \neq c_{\lambda,\kappa}(t_0)$). Obviously, this behavior is a big difference to the classical system, where independent of the initial phase the transport is zero, if one of the spatiotemporal symmetries of the potential is established. Still, $v(t_0)$ is point-symmetric with respect to $t_0 = \pi$, i.e. $v(t_0 + \pi) = -v(t_0 - \pi)$ so that the average $\langle v \rangle$ of the transport velocity over one period of t_0 is zero, i.e.

$$\langle v \rangle = \frac{1}{T} \int_0^T v(t_0) dt_0 = 0 \tag{6.87}$$

Contrary, we get for the same initial state in the lattice with phase gradient of period three $\varphi_i = \{\ldots, 0, 2\pi/3, 4\pi/3, \ldots\}$ a non-vanishing current independent of t_0 (Fig. 6.9 (b)). Accordingly, the average transport acquires as well a nonzero value $\langle v \rangle = -0.021$. It is important to note that in the quantum case the properties of the transport like the direction or the magnitude depend not only on the properties of the driven lattice but also crucially on the initial

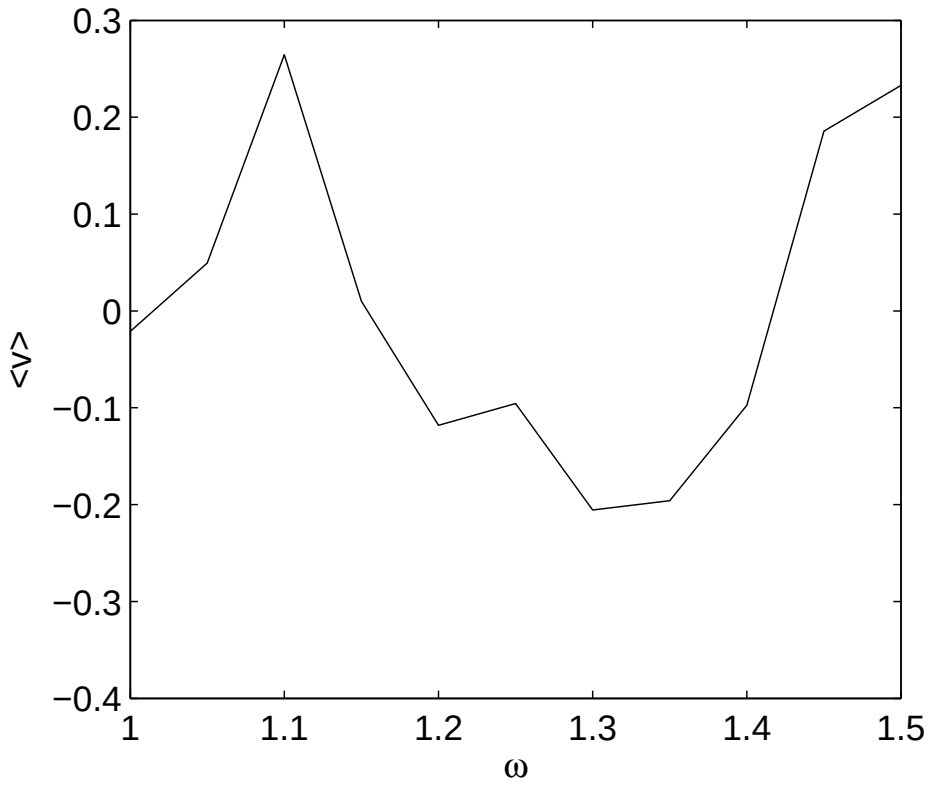

Figure 6.10: Transport velocity averaged over the initial phase t_0 in the lattice with phase period three $\varphi_i = \{\ldots, 0, 2\pi/3, 4\pi/3, \ldots\}$ as a function of the driving frequency. The parameters are $\sigma = 6\pi$, $\delta = 1/2$, $C = 1$ and $V_0 = 1$.

state. Consequently, the curves shown in Fig. 6.9 look possibly different for another width of the Gaussian wave packet σ. The transport can be tuned by e.g. varying the frequency of the driving while keeping the phase gradient and all other parameters like the initial width of the wavepacket σ fixed which can be seen from Fig. 6.10. In this plot the average current $\langle v \rangle$ is shown as a function of the frequency of the driving. Obviously, by tuning the frequency from 1 to 1.5 the direction and the magnitude of the average transport can be manipulated.

Chapter 7

Summary

In this thesis we have investigated the classical and the quantum dynamics of non-interacting particles loaded into spatiotemporally driven lattices. Due to the fact that the spatial and the temporal dependency of the corresponding time-dependent driving force do not decouple, i.e. the driving is local, novel interesting phenomena are evoked.

In the first part of the classical study we have seen that the particles which are loaded with small initial momentum in the driven lattice obey chaotic or regular dynamics, that is the classical phase space of the system is mixed [100]. By adjusting the parameters of the barriers and their corresponding driving laws specific parts of the phase space can be manipulated in a controllable manner while the remaining portion stays mainly unaffected. We have found that by means of a suitable choice of the local phase shifts for the barriers' driving laws the generalized parity and time-reversal symmetries of the Hamiltonian, identified in Ref. [44], can be broken leading to directed transport. The origin of this transport has been traced back to a desymmetrization of the chaotic sea in phase space with respect to $p = 0$ [45,46,51]. Properties of the transport like its direction or the magnitude can be tuned by adjusting the local phase shifts or parameters of the barriers (e.g. the potential height) whereas the most simplest way to revert the direction of the transport is by inverting the phase gradient [100]. Commonly, the phase space asymmetry is achieved by applying globally a biharmonic driving [33,37,44,47,48,51]. For this driving law a kinematic argument considering the single barrier dynamics is sufficient to explain the occurrence of a desymmetrization of the extended system's phase space, i.e. each barrier is transporting itself and the lattice inherits this property [100]. In this thesis it has been shown that a simple harmonic driving law together with a local breaking of certain symmetries of the unit cell implemented by local phase shifts is sufficient to generate a current of particles although each individual barrier is non-transporting. Consequently, the occurrence of the directed transport is in this case a collective phenomenon, i.e. the transport becomes a property of the lattice. Furthermore, we have found super-diffusion in configuration space for all studied driven lattices which is due to the mixed phase space structure [47, 51] leading to alternating dynamics between phases of diffusive motion and ballistic flights originating e.g. from stickiness to elliptic islands [47, 51, 100]. Moreover, we have seen that when each barrier is driven harmonically and equipped with an appropriately chosen phase shift it is possible to evoke localized chaotic dynamics at certain locations in the lattice, i.e. the corresponding trajectories are trapped between neighboring barriers [100]. This interesting effect has been exploited in [85] to demonstrate the selective trapping of particles in driven lattices which can be useful for e.g. quantum information processing.

As the next step in the classical study we have considered the impact on the non-equilibrium particle dynamics of breaking the generalized parity and time-reversal symmetries inhomogeneously by applying a spatially different time-periodic force [101]. Specifically, we have

considered a lattice possessing domains, each consisting of many barriers, and subject to different driving laws whereas neighboring domains feature oppositely directed local currents. At the interfaces between the differently driven blocks the particles can exhibit conversions of their dynamical character (ballistic / chaotic). By analyzing thoroughly the dynamics of single trajectories and the phase space properties of the domains we have identified the origin of these crossovers. The "local phase spaces" of adjacent blocks are concatenated at an interface which enables the particles to switch between the different phase space components in the blocks, e.g. by crossing the interface the particle can be injected from the chaotic sea into an elliptic island which is equivalent to a crossover from diffusive to ballistic dynamics [101]. Meanwhile, these phase space injection processes have been studied in finite systems which can transform an ensemble of diffusive particles into a pulsed, mono-energetic beam [84]. Furthermore, by overlapping appropriately the "local" phase spaces it has been found that the interfaces with incoming and outgoing flux are not equivalent with respect to the dynamical conversion properties occurring at their positions which leaves its hallmarks in the evolution of an ensemble of particles propagating in such a bimodally driven lattice [101]. It has been found that the trajectories typically obey alternately phases of ballistic and diffusive motion at the scale of one domain. For the temporal evolution of the spatial particle distribution $\rho(x)$ this behavior causes transient periodic modulations of $\rho(x)$ possessing local minima / maxima in a block which are smoothed out in the asymptotic time limit. By feeding the system with a constant beam of particles the periodic modulations of the spatial particle distribution $\rho(x)$ become asymptotically stable. If the interfaces are additionally moved through the lattice by a suitable time-dependent manipulation of the driving laws, the distribution $\rho(x)$ will follow approximately adiabatic this movement, i.e. the shape of $\rho(x)$ is preserved. Consequently, by means of this procedure the particle distribution is rendered into a propagating density wave.

In the quantum regime of the driven lattice the time-dependent Schrödinger equation has been solved by combining Floquet- and Bloch theory which are the mathematical frameworks for a Hamiltonian being periodic in time and space, respectively. We have obtained an eigenvalue equation for the Floquet modes $\Phi_{\lambda,\kappa}(x,t)$ and their corresponding quasienergies $\epsilon_{\lambda,\kappa}$ which contain the complete information in order to propagate an arbitrary initial wave function and to calculate the asymptotic transport velocity. For the lattice of uniformly oscillating barriers it has been confirmed that a current can be evoked depending on a global initial phase shift of the barriers although the Hamiltonian is invariant under the generalized parity and time-reversal transformation. Evidently, this behavior is a pure quantum effect because the transport vanishes in the classical system for an ensemble of particles in the chaotic sea when one of the spatiotemporally symmetries is established [44,51]. Finally, it has been shown that by changing the frequency of the driving the quantum transport in a phase modulated lattice with monochromatic driving can be tuned in direction and magnitude.

For further studies in the classical regime it would be expedient to consider the non-equilibrium dynamics when the oscillation of the barriers gets influenced by the interaction with the particles. In doing so, one could study whether memory effects play a role for the transport. In the quantum regime an interesting question is whether the classical dynamical conversion processes happening in the block-structured lattices leave their hallmarks also in the quantum dynamics.

Appendix A

Detection of periodic orbits in the Poincaré surface of section

In this appendix we present two methods for calculating the periodic orbits of the driven lattice. The first scheme is based on the symmetry properties of the corresponding trajectories in real space. Thus it is suitable for orbits where the particle undergoes only few collisions. The second method uses a variational principle and is based on the ideas in [76, 102]. It can be applied to orbits with many collisions.

A.1 Periodic orbits with few collisions

In the following we show how the position of dominant elliptic islands in the PSS can be calculated analytically using the example of the monochromatically, uniformly driven lattice with the parameters defined in Sec. 3.1, i.e. $V_0 = 0.16$, $l = 0.4$, $C = 1$, $m = 1$, $D = 4.4$ and $\omega = 1$. In Ref. [70] the authors have shown that due to the point-like interaction between the barrier and the particles it is possible to determine analytically the position in the Poincaré surface of section of the elliptic island corresponding to trapped dynamics in the scattering region of a single barrier by exploiting symmetry properties of the central periodic orbit (Fig. A.1 (a)). According to Ref. [70] the phase of the first collision is given by the root of the following function

$$f(\xi_1) = \left(\frac{2\cos(\xi_1) - \frac{l}{C}}{\pi - 2\xi_1} \right)^2 \cdot \left(\frac{2\sin(\xi_1)(\pi - 2\xi_1)}{2\cos(\xi_1) - \frac{l}{C}} - 1 \right) - \frac{V_0}{V'}, \tag{A.1}$$

with $V' = \frac{m}{2}\omega^2 C^2$. Once ξ_1 is known the other collision phases are given by

$$\begin{aligned} \xi_2 &= \pi - \xi_1, \\ \xi_3 &= \pi + \xi_1, \\ \xi_4 &= 2\pi - \xi_1. \end{aligned}$$

Fig. A.2 shows $f(\xi_1)$ (blue line) for the parameters of the monochromatically uniformly driven lattice. As we see, there are two roots and the physical significant one lies to the right of the function's maximum [70]. Applying the Newton-Raphson method to Eq. (A.1) yields $\xi_1 \approx 1.32$. Since the velocity of the particle before the collision is zero, its position at $t = 0$ is calculated straightforwardly by calculating the position of the barrier's left edge at phase ξ_1 (Fig. A.1 (a)), i.e.

$$x_{b,0}(\xi_1) = -\frac{l}{2} + C\cos(\xi_1) \approx 0.05. \tag{A.2}$$

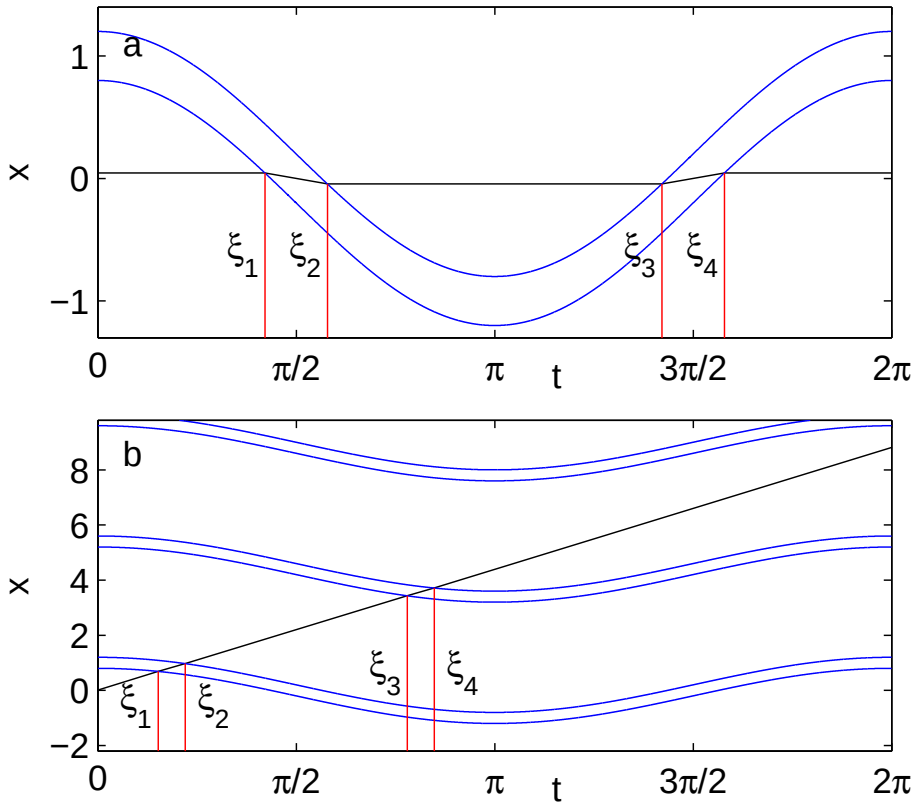

Figure A.1: Trajectories in real space in the monochromatically, uniformly driven lattice corresponding to the elliptic islands belonging to trapped dynamics (a) and winding numbers $w = 2$ (b).

Consequently, the central periodic orbit is at $x \approx 0.05$, $p = 0$ which coincides perfectly with the PSS (Fig. 3.1 (a)). In the following it is shown that the position of dominant ballistic, elliptic islands can be calculated similiarly using the example of the island with winding number $w = 2$.

As we see, the trajectory is symmetric with respect to $\frac{\pi}{2}$ (see Fig. A.1 (c)), i.e. $\xi_4 = \pi - \xi_1$ and $\xi_3 = \pi - \xi_2$. Consequently the particle's velocity in the first barrier equals the velocity in the second one, that is $v_1 = v_3$. According to Eq. (2.17) the particle's velocity after the first v_1 and the third collision v_3 is

$$v_1 = v_{b,0}(\xi_1) + \sqrt{\left(v_0 - v_{b,0}(\xi_1)\right)^2 - \frac{2V_0}{m}}, \tag{A.3}$$

$$v_3 = v_{b,0}(\xi_3) + \sqrt{\left(v_2 - v_{b,0}(\xi_3)\right)^2 - \frac{2V_0}{m}}, \tag{A.4}$$

where we have omitted the sign in both cases because the collisions at ξ_1 and ξ_3 occur when the barrier moves contrary to the particle. With $\xi_3 = \pi - \xi_1$ and $v_{b,0}(\xi) = -\omega C \sin(\xi)$ the

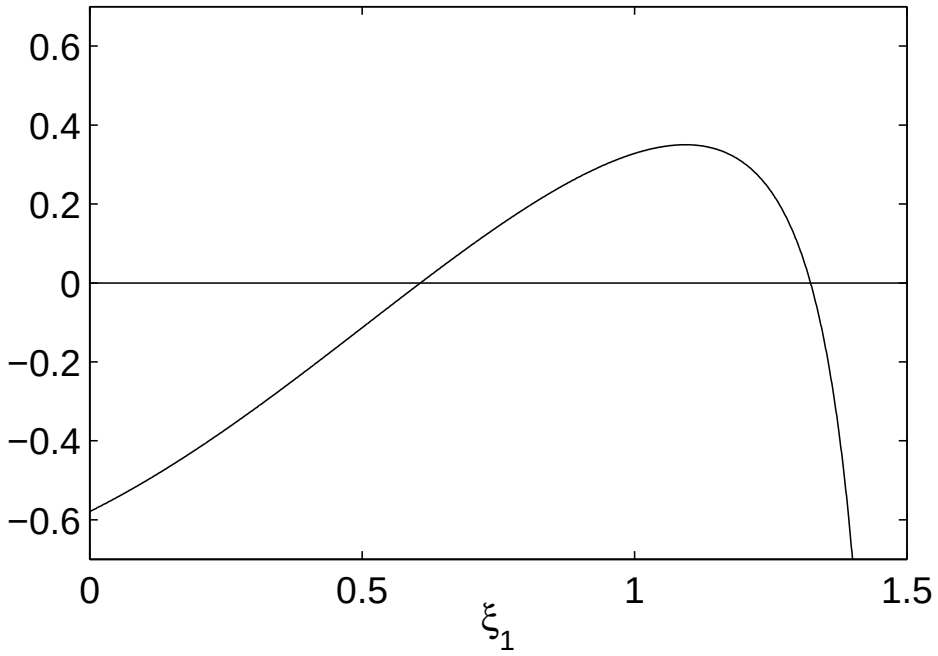

Figure A.2: The root of the function $f(\xi_1)$, which lies to the right of the maximum is the phase of the first collision ξ_1 of the central periodic orbit for the elliptic island corresponding to trapped dynamics (Fig. A.1 (a)).

condition $v_1 = v_3$ yields the following relation

$$\begin{aligned} f_1(\xi_1, \xi_2) = &\sin(\xi_1) - \sin(\xi_2) + \sqrt{(v_2 + \sin(\xi_2))^2 - \frac{V_0}{V'}} \\ &- \sqrt{(v_0 + \sin(\xi_1))^2 - \frac{V_0}{V'}} = 0 \end{aligned} \tag{A.5}$$

The initial velocity v_0 is determined as follows. The corresponding time span Δt_1 between the collision at ξ_1 and ξ_4 is

$$\Delta t_1 = \frac{\xi_4 - \xi_1}{\omega} = \frac{\pi - 2\xi_1}{\omega}. \tag{A.6}$$

The remaining distance is covered by the particle during Δt_2 which is given by

$$\Delta t_2 = \frac{2L - \Delta x}{v_0}, \tag{A.7}$$

where Δx is the distance between the first and fourth collision. Thus, Δx is derived from

$$\begin{aligned} \Delta x &= x_{b,1}(\xi_4) - x_{b,0}(\xi_1) \\ &= x_{0,1} + \frac{l}{2} + C\cos(\xi_4) - \left(x_{0,0} - \frac{l}{2} + C\cos(\xi_1) \right) \\ &= L + l - 2C\cos(\xi_1). \end{aligned} \tag{A.8}$$

Consequently, the initial velocity v_0 is found as before from the condition

$$\Delta t_1 + \Delta t_2 = T. \tag{A.9}$$

Plugging Δt_1 and Δt_2 into this equation and solving it for v_0 yields

$$v_0 = \omega C \frac{\frac{L-l}{C} + 2\cos(\xi_1)}{\pi + 2\xi_1}. \tag{A.10}$$

In order to determine the particle's velocity v_2 between the second and third collision we proceed as follows. Δt_1 is the sum of the time intervals $[0, \xi_2]$ and $[\xi_3, 2\pi]$, that is

$$\Delta t_1 = \frac{2\pi - \xi_3 + \xi_2}{\omega} = \frac{\pi + 2\xi_2}{\omega}. \tag{A.11}$$

Δt_2 is the time between the second and third collision, i.e.

$$\Delta t_2 = \frac{\Delta x}{v_2}, \tag{A.12}$$

where Δx is simply

$$\begin{aligned} \Delta x &= x_{b,1}(\xi_3) - x_{b,0}(\xi_2) \\ &= x_{0,1} - \frac{l}{2} + C\cos(\xi_3) - \left(x_{0,0} + \frac{l}{2} + C\cos(\xi_2) \right) \\ &= L - l - 2C\cos(\xi_2). \end{aligned} \tag{A.13}$$

The sum of Δt_1 and Δt_2 is one period of the driving $T = 2\pi/\omega$ which yields finally the velocity after the second collision

$$v_2 = \omega C \frac{\frac{L-l}{C} - 2\cos(\xi_2)}{\pi - 2\xi_2}. \tag{A.14}$$

Inserting the expression for v_0 (Eq. (A.10)) and for v_2 (Eq. (A.14)) in Eq. (A.1) results in

$$\begin{aligned} f_1(\xi_1, \xi_2) = &\sin(\xi_1) - \sin(\xi_2) + \sqrt{\left(\frac{\frac{L-l}{C} - 2\cos(\xi_2)}{\pi - 2\xi_2} + \sin(\xi_2) \right)^2 - \frac{V_0}{V'}} \\ &- \sqrt{\left(\frac{\frac{L-l}{C} + 2\cos(\xi_1)}{\pi + 2\xi_1} + \sin(\xi_1) \right)^2 - \frac{V_0}{V'}} = 0 \end{aligned} \tag{A.15}$$

Another equation for ξ_1 and ξ_2 can be formulated as follows. The spatial distance $\Delta x = x_{b,0}(\xi_2) - x_{b,0}(\xi_1)$ between the collisions at ξ_1 and ξ_2 has to covered by the particle during

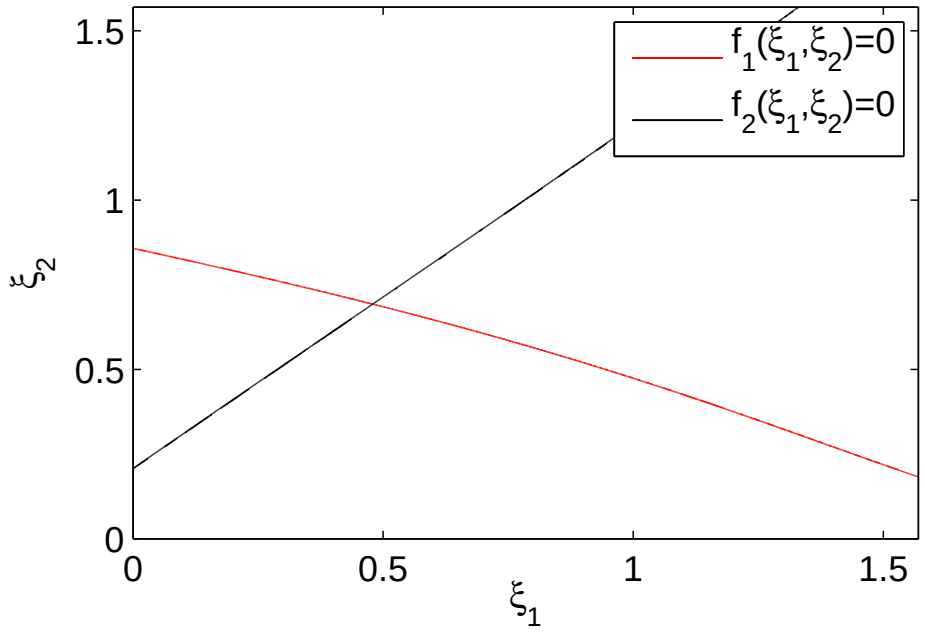

Figure A.3: Contourlines of the functions $f_1(\xi_1,\xi_2)=0$ and $f_1(\xi_1,\xi_2)=0$ giving the phase of the first and the second collision of the central periodic orbit belonging to the $w=2$ elliptic island (Fig. A.1(b)).

the time $\Delta t=(\xi_2-\xi_1)/\omega$, that is

$$x_{b,0}(\xi_2)-x_{b,0}(\xi_1)=v_1\frac{\xi_2-\xi_1}{\omega} \tag{A.16}$$

$$\Leftrightarrow l+C(\cos(\xi_2)-\cos(\xi_1))=\left(-\omega C\sin(\xi_1)+\sqrt{(v_0+\omega C\sin(\xi_1))^2-\frac{2V_0}{m}}\right)\frac{\xi_2-\xi_1}{\omega}, \tag{A.17}$$

which can written as before in the form

$$\begin{aligned} f_2(\xi_1,\xi_2)=&\cos(\xi_1)-\cos(\xi_2)\\ &+(\xi_2-\xi_1)\left(\sqrt{\left(\frac{\frac{L-l}{C}+2\cos(\xi_1)}{\pi+2\xi_1}+\sin(\xi_1)\right)^2-\frac{V_0}{V'}}-\sin(\xi_1)\right)-\frac{l}{C}=0 \end{aligned} \tag{A.18}$$

In Fig. A.3 we show the contourlines of the functions $f_{1,2}(\xi_1,\xi_2)=0$ in the ξ_1,ξ_2-plane. The intersection of the two curves is the sought-after solution of the equations (A.15), (A.18) and can be traced straightforwardly which yields $\xi_1\approx 0.48$ and $\xi_2\approx 0.69$. Plugging ξ_1 into Eq. (A.10) yields $v_0\approx 1.41$ and thus we have the momentum of the central periodic orbit $p=mv_0\approx 1.41$. Furthermore, since the particle moves ballistically between the collision, its position at $t=0$ is determined by

$$x(0)=x_{b,0}(\xi_1)-v_0\Delta t=-\frac{l}{2}+C\cos(\xi_1)-v_0\frac{\xi_1}{\omega}, \tag{A.19}$$

giving $x(0) \approx 0.01$. Accordingly, the central periodic orbit of the $w = 2$ elliptic island is at $x \approx 0.01$, $p \approx 1.41$ which coincides perfectly with the PSS (Fig. 3.1 (a)).

In general, we can proceed similarly for setups with larger phase periods and for every resonance. A system of equations will therefore result

$$\{f_i(\xi_1, \xi_2, \cdots, \xi_k) = 0, \;\; i = 1 \ldots k\}. \tag{A.20}$$

We remark that it is difficult to generalize this scheme to periodic orbits with many collisions, since the approach to set up the system of equations and the roots corresponding to physical solutions depend on the specific symmetry properties of the phases upon collisions of the central periodic orbit belonging to the resonance.

A.2 Periodic orbits with many collisions

For periodic orbits with many collisions, which we need in order to determine the flux through a cantorus (Appendix B), the scheme presented in the previous section is obviously not feasible anymore. In this case it makes more sense to make use of a variational method [76,102], which will be presented in the following. Between successive collisions with the barriers' edges, the particles move ballistically in a constant potential. Hence the Lagrangian of the system is simply

$$L(x, \dot{x}, t) = \begin{cases} \frac{mv^2}{2} & \text{particle between barriers} \\ \frac{mv^2}{2} - V_0 & \text{particle in a barrier.} \end{cases} \tag{A.21}$$

The action of a periodic orbit in the PSS with winding number $w = r/s$ is given by

$$W_{r/s} = \sum_{i=0}^{s-1} \int_{t_i}^{t_{i+1}} L(x, \dot{x}, t) dt, \tag{A.22}$$

where $t_i = iT$ is the moment, when the i-th PSS is taken. Due to the point-like interaction the action Eq. (A.22) can be added piecewise. In general, the action (A.22) can be rewritten as

$$W_{r/s} = \sum_{k=0}^{N} W_k(t_k, t_{k+1}). \tag{A.23}$$

N is the total number of collisions occurring between t_0 and $t_{N+1} = t_0 + sT$. In the following we assume that the particle's position $x(t_0)$ does not coincide with one of the barrier's edges when the first PSS is taken. Now we restrict ourselves to periodic orbits with winding number $w = r/s$. The integer r specifies how many spatial unit cells of length L a trajectory travels in the lattice, at which the velocity never changes sign. Each unit cell consists of n barriers, where n is the phase period. With each barrier the particle collides exactly two times because a transmission occurs at every collision. Accordingly, the number of collisions N, the phase period n and r are related through $N = 2nr$. Inserting the Lagrangian of the system (A.21)

in equation (A.23) gives

$$W_k(t_k, t_{k+1}) = \begin{cases} \frac{m(x(t_{k+1})-x(t_k))^2}{2(t_{k+1}-t_k)} & \text{particle between barriers} \\ \frac{m(x(t_{k+1})-x(t_k))^2}{2(t_{k+1}-t_k)} - V_0\,(t_{k+1}-t_k) & \text{particle in barrier.} \end{cases} \tag{A.24}$$

$x(t_k)$ equals for $k = 1, \ldots, N$ with the position of one of the barriers' edges at a collision, which depends on the driving law $f_i(t)$ at the i-th site. For particles in a barrier the spatial distance between the successive collisions is $x(t_{k+1}) - x(t_k) = l + f_i(t_{k+1}) - f_i(t_k)$ and accordingly $x(t_{k+1}) - x(t_k) = D - l + f_{i+1}(t_{k+1}) - f_i(t_k)$ between the barriers. Setting $m = 1$ the action $W_k(t_k, t_{k+1}$ for $k = 1, \ldots, N-1$ becomes

$$W_k(t_k, t_{k+1}) = \begin{cases} \frac{(D-l+f_{i+1}(t_{k+1})-f_i(t_k))^2}{2(t_{k+1}-t_k)} & \text{particle between barriers} \\ \frac{(l+f_i(t_{k+1})-f_i(t_k))^2}{2(t_{k+1}-t_k)} - V_0 \cdot (t_{k+1}-t_k) & \text{particle in barrier.} \end{cases} \tag{A.25}$$

For $k = 0$ we get with $t_0 = 0$, $x(t_0) = x_0$ and $m = 1$

$$\begin{aligned} W_0(t_0, t_1) &= \frac{(x(t_1) - x(t_0))^2}{2(t_1 - t_0)} \\ &= \frac{\left(-\frac{l}{2} + f_1(t_1) - x_0\right)^2}{2t_1}, \end{aligned} \tag{A.26}$$

i.e. this part of the action depends on the particle's starting position x_0 and the time of the first collision t_1, that is in the following we write $W_0(x_0, t_1)$. For $k = N$ we find

$$\begin{aligned} W_N(t_N, t_{N+1}) &= \frac{(x(t_{N+1}) - x(t_N))^2}{2(t_{N+1}) - t_N)} \\ &= \frac{\left(x_0 + D - \frac{l}{2} - f_N(t_N)\right)^2}{2(sT - t_N)}, \end{aligned} \tag{A.27}$$

where we have used that $t_{N+1} = t_0 + sT = sT$ and $x(t_{N+1}) = x_0 + rL = x_0 + rnD$, $x(t_N) = (rn-1)D + \frac{l}{2} + f_N(t_N)$, i.e. $W_N(t_N, x_0)$. We search for trajectories for which the action is extremal, i.e. we vary the collision times $t_1, \ldots, t_N$ and the initial position of the trajectory x_0. The action gradient vector is $\nabla W = (\partial W/\partial x_0, \partial W/\partial t_1, \ldots, \partial W/\partial t_N)^T$, where the partial derivatives of the action with respect to t_i for $k = 2, \ldots, N-1$ are given by

$$\frac{\partial W}{\partial t_i} = \frac{\partial W_{i-1}(t_{i-1}, t_i)}{\partial t_i} + \frac{\partial W_i(t_i, t_{i+1})}{\partial t_i}. \tag{A.28}$$

Correspondingly, for the initial position x_0 and t_1, t_N we have

$$\frac{\partial W}{\partial x_0} = \frac{\partial W_0(t_0, t_1)}{\partial x_0} + \frac{\partial W_N(t_N, t_{N+1})}{\partial x_0} \tag{A.29}$$

$$\frac{\partial W}{\partial t_1} = \frac{\partial W_0(t_0, t_1)}{\partial t_1} + \frac{\partial W_1(t_1, t_2)}{\partial t_1} \tag{A.30}$$

$$\frac{\partial W}{\partial t_N} = \frac{\partial W_{N-1}(t_{N-1}, t_N)}{\partial t_N} + \frac{\partial W_N(t_N, x_0)}{\partial t_N}. \tag{A.31}$$

For finding roots of ∇W a multidimensional Newton scheme has been applied. Therefore, the derivative matrix ("Hessian") of the action gradient is needed. It is a cyclic, tridiagonal matrix of the second derivatives of W_i, whose rank increases with the period s of the orbit [102]. To get an initial starting point we start from the integrable limit ($V_0 = 0$) and trace the periodic orbits as the perturbation, i.e. V_0, is increased. Finally, the stability of the obtained periodic orbit can be determined via the eigenvalues of the Hessian. In the case of the unstable orbit it has only positive eigenvalues, whereas for the stable periodic orbit there is a single negative eigenvalue [102]. For orbits with not too high periods ($s < 300$) the results of this scheme have been compared additionally to other globally convergent methods [103,104] and we have found agreement.

Appendix B

Flux through cantori and transit times

In this appendix we discuss the transit times of orbits in the PSS. First of all, we give an example of trajectories in the chaotic sea, which are confined to a subpart of phase space for a very long time. Then a procedure how to approximate the average escape time from this region is described briefly. Finally, this method is applied exemplarily in the case of the uniformly oscillating lattice. In Fig. B.1 a magnification of the PSS of a single trajectory is shown. It has been launched in the chaotic layer close to the FISC and once it has crossed the $p = 0$-axis in the PSS, the simulation has been stopped. Obviously, there are sudden changes in the density of points in the PSS. This is a hallmark of the so-called cantori, which are remnants of dissolved tori with irrational winding number. These objects can be regarded as tori with gaps, so that the Hamiltonian flow is able to pass through [76]. The diamonds

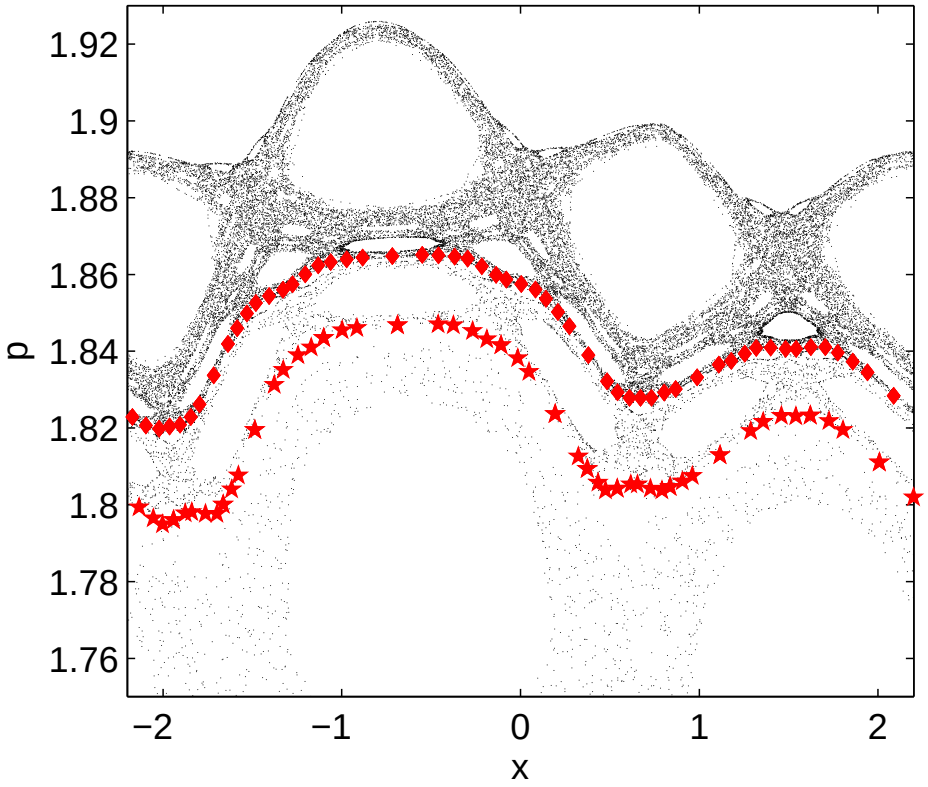

Figure B.1: Poincaré surface of section of a single chaotic trajectory, which has been started in the upper region and stopped once it has crossed the $p = 0$-axis. The diamonds and stars are periodic orbits corresponding to truncations of the continued fraction expansion of $w_1 = \frac{2\gamma+1}{\gamma}$ and $w_2 = \frac{29\gamma-1}{11\gamma}$, respectively.

and stars in Fig. B.1 are periodic orbits, which belong to truncations of the continued fraction expansions of cantori with the noble winding numbers $w_1 = \frac{2\gamma+1}{\gamma} = [2, 1^\infty]$ and $w_2 = \frac{29\gamma-1}{11\gamma} = [2, 1, 1, 2, 1^\infty]$, where $\gamma = \frac{1+\sqrt{5}}{2}$ is the golden mean. The associated rational winding numbers for the two periodic orbits are

$$\begin{aligned} w_\bullet &= [2, 1^9] = \frac{144}{55} \\ w_\star &= [2, 1, 1, 2, 1^5] = \frac{129}{50}. \end{aligned} \tag{B.1}$$

As long as the trajectories are confined in the PSS to the region above the cantorus, their velocity never changes sign. Moreover, the magnitude of the velocity varies only over a narrow interval. Thus, they perform ballistic-like motion during this time span. This has severe impact on the dynamics of an ensemble of particles, i.e. it leads to super diffusion in configuration space as we have seen in Sec. 4.1.2. In order to obtain the average length of the ballistic flights, we have to determine the flux Φ_w through a cantorus with irrational winding number w. Mather [105] has shown that the sequence of differences in action of periodic orbits belonging to truncations of the continued fraction expansion of w converges to Φ_w

$$\Phi_w = \lim_{\frac{r}{s} \to w} \Big(W_{r/s} - W^*_{r/s} \Big), \tag{B.2}$$

where $W_{r/s}$, $W^*_{r/s}$ is the action of the "minimizing" and the "minimax" orbit respectively [76], i.e. periodic orbits with winding number $w = r/s$, belonging to the minimum (saddle point) of the action. The minimizing orbit is generically unstable and hyperbolic, whereas the minimax orbit is either an elliptic or hyperbolic-with-reflection periodic orbit. The method for determining the periodic orbits with winding number $w = r/s$ and their corresponding action sis described in Appendix A.2. In the following $\Phi_{r/s} = W_{r/s} - W^*_{r/s}$ is called the flux through a chain of periodic orbits with winding number $w = r/s$. Fig. B.2 shows the flux Φ_{r_j/s_j} through convergents of w_1 and w_2 as a function of the level j of the truncated continued fraction expansions. In the beginning the flux scales according to the power-law $\Phi_{r_j/s_j} \sim C\xi^{-j}$ with $\xi \approx 4.339$ [106] (black curve in Fig. B.2). Still the sequence converges rapidly with increasing j as Fig. B.2 shows. Asymptotically, we find for the fluxes through the cantori $\Phi_{w_1} = 3.62 \cdot 10^{-7}$ and $\Phi_{w_2} = 1.09 \cdot 10^{-5}$. An approximation to the transit time for particles to get from the region above the cantorus with winding number w_i to the phase space below it is given by

$$t_{w_i} = \frac{A_{w_i}}{\Phi_{w_i}}, \tag{B.3}$$

where A is the area in the PSS above w_i. By dividing the PSS into small squares, we have estimated these areas to be $A_{w_1} = 0.12$ and $A_{w_2} = 0.18$, which yields for the total transit time $t_{\text{transit}} = t_{w_1} + t_{w_2} = 3.48 \cdot 10^5$ to get in the PSS from the region above the cantorus w_1 to the region below the cantorus w_2. Consequently, on average the particles get confined 348.000 periods of the driving in this region of the phase space and thus perform during this time ballistic flights. We note that the above transit time is meant to provide a rough estimate for the transport through the cantori. The comparison with numerical data obtained by simulating an ensemble placed in a chaotic region close to the FISC shows that

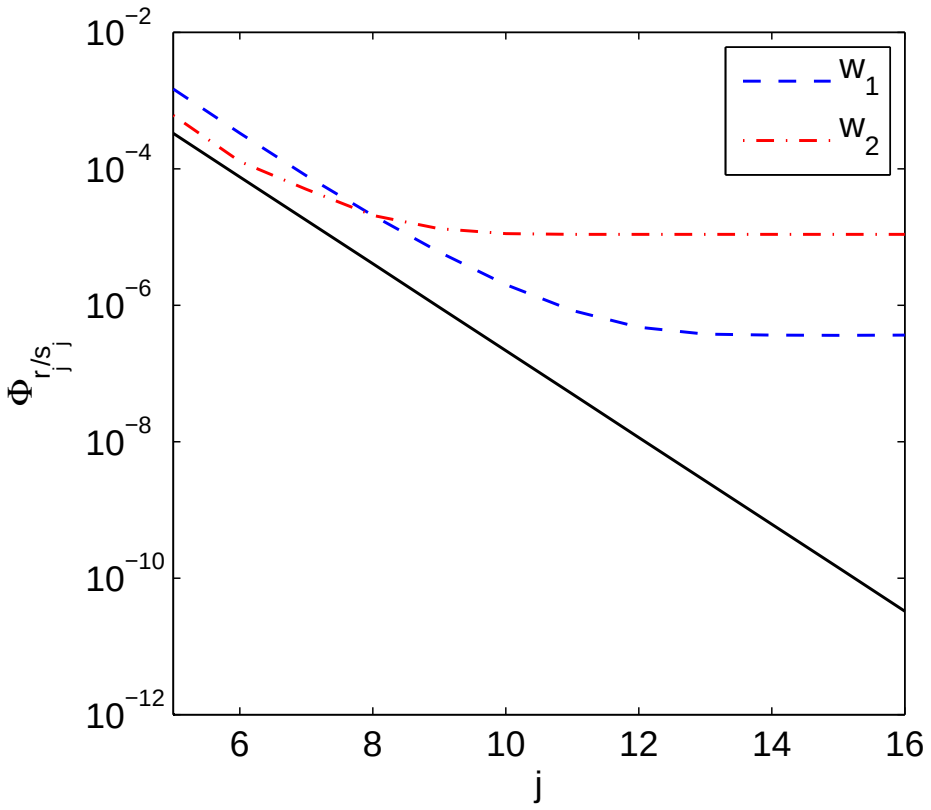

Figure B.2: Flux through the chains of periodic orbits, belonging to convergents of w_1 and w_2, as a function of the level j. The black curve is $\Phi_{r_j/s_j} \sim C\xi^{-j}$ with $\xi \approx 4.339$.

the transit time is in general even longer. Beside the effect of being trapped to the region above the cantorus, the trajectories accessorily can get sticky to the hierarchy of elliptic islands surrounded by subislands being above the cantorus. The latter process extends the ballistic flights significantly.

Bibliography

[1] W. A. Lin and L. E. Ballentine, Quantum tunneling and chaos in a driven anharmonic oscillator, Physical Review Letters **65**, 2927 (1990).

[2] F. Grossmann, T. Dittrich, P. Jung, and P. Hänggi, Coherent destruction of tunneling, Physical Review Letters **67**, 516 (1991).

[3] D. Farrelly and J. A. Milligan, Two-frequency control and suppression of tunneling in the driven double well, Physical Review E **47**, R2225 (1993).

[4] M. A. Lieberman and A. J. Lichtenberg, Stochastic and Adiabatic Behavior of Particles Accelerated by Periodic Forces, Physical Review A **5**, 1852 (1972).

[5] A. J. Lichtenberg and M. A. Lieberman, *Regular and Chaotic Dynamics*, Springer, 1992.

[6] F. Lenz, F. K. Diakonos, and P. Schmelcher, Tunable Fermi Acceleration in the Driven Elliptical Billiard, Physical Review Letters **100**, 014103 (2008).

[7] M. Gavrila, *Atoms in Intense Laser Fields*, Academic Press, 1992.

[8] N. B. Delone and V. P. Krainov, *Multiphoton Processes in Atoms*, Springer, 1995.

[9] T. Brabec and F. Krausz, Intense few-cycle laser fields: Frontiers of nonlinear optics, Reviews of Modern Physics **72**, 545 (2000).

[10] R. Feynman, R. Leighton, and M. Sands, *The Feynman Lectures on Physics*, Addison-Wesley, 1963.

[11] J. Maddox, Making models of muscle contraction, Nature **365**, 203 (1993).

[12] R. D. Astumian and M. Bier, Fluctuation driven ratchets: Molecular motors, Physical Review Letters **72**, 1766 (1994).

[13] F. Jülicher, A. Ajdari, and J. Prost, Modeling molecular motors, Reviews of Modern Physics **69**, 1269 (1997).

[14] M. O. Magnasco, Forced thermal ratchets, Physical Review Letters **71**, 1477 (1993).

[15] R. Bartussek, P. Hänggi, and J. G. Kissner, Periodically Rocked Thermal Ratchets, Europhysics Letters **28**, 459 (1994).

[16] C. R. Doering, W. Horsthemke, and J. Riordan, Nonequilibrium fluctuation-induced transport, Physical Review Letters **72**, 2984 (1994).

[17] R. Bartussek, P. Reimann, and P. Hänggi, Precise Numerics versus Theory for Correlation Ratchets, Physical Review Letters **76**, 1166 (1996).

[18] P. Jung, J. G. Kissner, and P. Hänggi, Regular and Chaotic Transport in Asymmetric Periodic Potentials: Inertia Ratchets, Physical Review Letters **76**, 3436 (1996).

[19] P. Reimann, Brownian motors: noisy transport far from equilibrium, Physics Reports **361**, 57 (2002).

[20] R. D. Astumian and P. Hänggi, Brownian Motors, Physics Today **55**, 33 (2002).

[21] H. Linke, Ratchets and Brownian motors: Basics, experiments and applications, Applied Physics A **75**, 167 (2002).

[22] P. Hänggi and F. Marchesoni, Artificial Brownian motors: Controlling transport on the nanoscale, Reviews of Modern Physics **81**, 387 (2009).

[23] J. M. R. Parrondo, G. P. Harmer, and D. Abbott, New Paradoxical Games Based on Brownian Ratchets, Physical Review Letters **85**, 5226 (2000).

[24] P. G. T. Gregory P. Harmer, Derek Abbott and J. M. R. Parrondo, Brownian ratchets and Parrondo's games, Chaos **11**, 705 (2001).

[25] H. Linke, T. E. Humphrey, A. Löfgren, A. O. Sushkov, R. Newbury, R. P. Taylor, and P. Omling, Experimental Tunneling Ratchets, Science **286**, 2314 (1999).

[26] K. N. Alekseev, M. V. Erementchouk, and F. V. Kusmartsev, Direct-current generation due to wave mixing in semiconductors, Europhysics Letters **47**, 595 (1999).

[27] V. S. Khrapai, S. Ludwig, J. P. Kotthaus, H. P. Tranitz, and W. Wegscheider, Double-Dot Quantum Ratchet Driven by an Independently Biased Quantum Point Contact, Physical Review Letters **97**, 176803 (2006).

[28] A. Sterck, S. Weiss, and D. Koelle, SQUID ratchets: basics and experiments, Applied Physics A **75**, 253 (2002).

[29] F. Falo, P. Martínez, J. Mazo, T. Orlando, K. Segall, and E. Trías, Fluxon ratchet potentials in superconducting circuits, Applied Physics A **75**, 263 (2002).

[30] J. B. Majer, J. Peguiron, M. Grifoni, M. Tusveld, and J. E. Mooij, Quantum Ratchet Effect for Vortices, Physical Review Letters **90**, 056802 (2003).

[31] S. Smirnov, D. Bercioux, M. Grifoni, and K. Richter, Quantum Dissipative Rashba Spin Ratchets, Physical Review Letters **100**, 230601 (2008).

[32] M. Schiavoni, L. Sanchez-Palencia, F. Renzoni, and G. Grynberg, Phase Control of Directed Diffusion in a Symmetric Optical Lattice, Physical Review Letters **90**, 094101 (2003).

[33] R. Gommers, S. Bergamini, and F. Renzoni, Dissipation-Induced Symmetry Breaking in a Driven Optical Lattice, Physical Review Letters **95**, 073003 (2005).

[34] R. Gommers, S. Denisov, and F. Renzoni, Quasiperiodically Driven Ratchets for Cold Atoms, Physical Review Letters **96**, 240604 (2006).

[35] R. Gommers, M. Brown, and F. Renzoni, Symmetry and transport in a cold atom ratchet with multifrequency driving, Physical Review A **75**, 053406 (2007).

[36] R. Gommers, V. Lebedev, M. Brown, and F. Renzoni, Gating Ratchet for Cold Atoms, Physical Review Letters **100**, 040603 (2008).

[37] T. Salger, S. Kling, T. Hecking, C. Geckeler, L. Morales-Molina, and M. Weitz, Directed Transport of Atoms in a Hamiltonian Quantum Ratchet, Science **326**, 1241 (2009).

[38] A. V. Arzola, K. Volke-Sepúlveda, and J. L. Mateos, Experimental Control of Transport and Current Reversals in a Deterministic Optical Rocking Ratchet, Physical Review Letters **106**, 168104 (2011).

[39] A. Wickenbrock, P. C. Holz, N. A. A. Wahab, P. Phoonthong, D. Cubero, and F. Renzoni, Vibrational Mechanics in an Optical Lattice: Controlling Transport via Potential Renormalization, Physical Review Letters **108**, 020603 (2012).

[40] V. Lebedev and F. Renzoni, Two-dimensional rocking ratchet for cold atoms, Physical Review A **80**, 023422 (2009).

[41] J. L. Mateos, Chaotic Transport and Current Reversal in Deterministic Ratchets, Physical Review Letters **84**, 258 (2000).

[42] M. Borromeo, G. Costantini, and F. Marchesoni, Deterministic ratchets: Route to diffusive transport, Physical Review E **65**, 041110 (2002).

[43] J. L. Mateos, Current reversals in chaotic ratchets: the battle of the attractors, Physica A **325**, 92 (2003).

[44] S. Flach, O. Yevtushenko, and Y. Zolotaryuk, Directed Current due to Broken Time-Space Symmetry, Physical Review Letters **84**, 2358 (2000).

[45] T. Dittrich, R. Ketzmerick, M.-F. Otto, and H. Schanz, Classical and quantum transport in deterministic Hamiltonian ratchets, Annalen der Physik **9**, 755 (2000).

[46] H. Schanz, M.-F. Otto, R. Ketzmerick, and T. Dittrich, Classical and Quantum Hamiltonian Ratchets, Physical Review Letters **87**, 070601 (2001).

[47] S. Denisov and S. Flach, Dynamical mechanisms of dc current generation in driven Hamiltonian systems, Physical Review E **64**, 056236 (2001).

[48] S. Denisov, J. Klafter, M. Urbakh, and S. Flach, DC currents in Hamiltonian systems by Lévy flights, Physica D **170**, 131 (2002).

[49] S. Denisov, S. Flach, A. A. Ovchinnikov, O. Yevtushenko, and Y. Zolotaryuk, Broken space-time symmetries and mechanisms of rectification of ac fields by nonlinear (non)adiabatic response, Physical Review E **66**, 041104 (2002).

[50] J. Gong and P. Brumer, Directed anomalous diffusion without a biased field: A ratchet accelerator, Physical Review E **70**, 016202 (2004).

[51] H. Schanz, T. Dittrich, and R. Ketzmerick, Directed chaotic transport in Hamiltonian ratchets, Physical Review E **71**, 026228 (2005).

[52] L. Cavallasca, R. Artuso, and G. Casati, Directed deterministic classical transport: Symmetry breaking and beyond, Physical Review E **75**, 066213 (2007).

[53] L. Wang, G. Benenti, G. Casati, and B. Li, Ratchet Effect and the Transporting Islands in the Chaotic Sea, Physical Review Letters **99**, 244101 (2007).

[54] S. Denisov, S. Flach, and P. Hänggi, Stationary Hamiltonian transport with dc bias, Europhysics Letters **74**, 588 (2006).

[55] I. Goychuk and P. Hänggi, Minimal Quantum Brownian Rectifiers, Journal of Physical Chemistry B **105**, 6642 (2001).

[56] G. G. Carlo, G. Benenti, G. Casati, and D. L. Shepelyansky, Quantum Ratchets in Dissipative Chaotic Systems, Physical Review Letters **94**, 164101 (2005).

[57] S. Denisov, S. Kohler, and P. Hänggi, Underdamped quantum ratchets, Europhysics Letters **85**, 40003 (2009).

[58] G. G. Carlo, G. Benenti, G. Casati, S. Wimberger, O. Morsch, R. Mannella, and E. Arimondo, Chaotic ratchet dynamics with cold atoms in a pair of pulsed optical lattices, Physical Review A **74**, 033617 (2006).

[59] D. Poletti, G. G. Carlo, and B. Li, Current behavior of a quantum Hamiltonian ratchet in resonance, Physical Review E **75**, 011102 (2007).

[60] S. Denisov, L. Morales-Molina, S. Flach, and P. Hänggi, Periodically driven quantum ratchets: Symmetries and resonances, Physical Review A **75**, 063424 (2007).

[61] S. Denisov, L. Morales-Molina, and S. Flach, Quantum resonances and rectification in ac-driven ratchets, Europhysics Letters **79**, 10007 (2007).

[62] L. Morales-Molina, S. Flach, and J. B. Gong, Quantum ratchet control - Harvesting on Landau-Zener transitions, Europhysics Letters **83**, 40005 (2008).

[63] T. S. Monteiro, P. A. Dando, N. A. C. Hutchings, and M. R. Isherwood, Proposal for a Chaotic Ratchet Using Cold Atoms in Optical Lattices, Physical Review Letters **89**, 194102 (2002).

[64] N. A. C. Hutchings, M. R. Isherwood, T. Jonckheere, and T. S. Monteiro, Chaotic Hamiltonian ratchets for pulsed periodic double-well potentials: Classical correlations and the ratchet current, Physical Review E **70**, 036205 (2004).

[65] J. Gong and P. Brumer, Generic Quantum Ratchet Accelerator with Full Classical Chaos, Physical Review Letters **97**, 240602 (2006).

[66] A. V. Ponomarev, S. Denisov, and P. Hänggi, ac-Driven Atomic Quantum Motor, Physical Review Letters **102**, 230601 (2009).

[67] D. Tannor, *Introduction to Quantum Mechanics: A Time-Dependent Perspective*, University Science Books, 2006.

[68] M. Grifoni and P. Hänggi, Driven quantum tunneling, Physics Reports **304**, 229 (1998).

[69] S.-I. Chu and D. A. Telnov, Beyond the Floquet theorem: generalized Floquet formalisms and quasienergy methods for atomic and molecular multiphoton processes in intense laser fields, Physics Reports **390**, 1 (2004).

[70] F. R. N. Koch, F. Lenz, C. Petri, F. K. Diakonos, and P. Schmelcher, Dynamical trapping and chaotic scattering of the harmonically driven barrier, Physical Review E **78**, 056204 (2008).

[71] F. Koch, Nonlinear dynamics in the harmonically driven barrier, Diplomathesis, University of Heidelberg, 2007.

[72] W. Press, S. Teukolsky, W. Vetterling, and B. Flannery, *Numerical Recipes in C*, Cambridge University Press, 1992.

[73] C. F. F. Karney, Long-time correlations in the stochastic regime, Physica D **8**, 360 (1983).

[74] B. Chirikov and D. Shepelyansky, Correlation properties of dynamical chaos in Hamiltonian systems, Physica D **13**, 395 (1984).

[75] M. Tabor, *Chaos and Integrability in Nonlinear Dynamics: An Introduction*, Wiley-Interscience, 1989.

[76] J. D. Meiss, Symplectic maps, variational principles, and transport, Reviews of Modern Physics **64**, 795 (1992).

[77] E. G. Altmann, A. E. Motter, and H. Kantz, Stickiness in Hamiltonian systems: From sharply divided to hierarchical phase space, Physical Review E **73**, 026207 (2006).

[78] L. A. Bunimovich, Relative volume of Kolmogorov-Arnold-Moser tori and uniform distribution, stickiness and nonstickiness in Hamiltonian systems, Nonlinearity **21**, T13 (2008).

[79] L. A. Bunimovich, Mushrooms and other billiards with divided phase space, Chaos **11**, 802 (2001).

[80] M. Newman, Power laws, Pareto distributions and Zipf's law, Contemporary Physics **46**, 323 (2005).

[81] E. W. Montroll and G. H. Weiss, Random Walks on Lattices. II, Journal of Mathematical Physics **6**, 167 (1965).

[82] G. Zumofen, J. Klafter, and A. Blumen, Lévy walks and propagators in intermittent chaotic systems, Physical Review E **47**, 2183 (1993).

[83] J. Klafter and G. Zumofen, Lévy statistics in a Hamiltonian system, Physical Review E **49**, 4873 (1994).

[84] T. Wulf, Interface dynamics of spatio-temporally driven layers, Diplomathesis, University of Hamburg, 2011.

[85] B. Liebchen, C. Petri, F. Lenz, and P. Schmelcher, Patterned deposition of particles in spatio-temporally driven lattices, Europhysics Letters **94**, 40001 (2011).

[86] P. K. Papachristou, F. K. Diakonos, E. Mavrommatis, and V. Constantoudis, Nonperiodic delay mechanism and fractallike behavior in classical time-dependent scattering, Physical Review E **64**, 016205 (2001).

[87] E. Ott, *Chaos in Dynamical Systems*, Cambridge Univeristy Press, 1992.

[88] F. Zhan, S. Denisov, A. V. Ponomarev, and P. Hänggi, Quantum ratchet transport with minimal dispersion rate, Physical Review A **84**, 043617 (2011).

[89] H. Sambe, Steady States and Quasienergies of a Quantum-Mechanical System in an Oscillating Field, Physical Review A **7**, 2203 (1973).

[90] J. H. Shirley, Solution of the Schrödinger Equation with a Hamiltonian Periodic in Time, Physical Review **138**, B979 (1965).

[91] K. F. Milfeld and R. E. Wyatt, Study, extension, and application of Floquet theory for quantum molecular systems in an oscillating field, Physical Review A **27**, 72 (1983).

[92] T. Dittrich, P. Hänggi, G.-L. Ingold, B. Kramer, G. Schön, and W. Zwerger, *Quantum Transport and Dissipation*, Wiley-VCH, 1998.

[93] S.-K. Son, S. Han, and S.-I. Chu, Floquet formulation for the investigation of multiphoton quantum interference in a superconducting qubit driven by a strong ac field, Physical Review A **79**, 032301 (2009).

[94] M. Henseler, *Klassische und Quantendynamik periodisch getriebener, chaotischer Streusysteme*, PhD thesis, Technical University of Dresden, 1999.

[95] I. Vorobeichik, R. Lefebvre, and N. Moiseyev, Field-induced barrier transparency, Europhysics Letters **41**, 111 (1998).

[96] I. Vorobeichik and N. Moiseyev, State-to-state transition probabilities for time-dependent Hamiltonians using complex absorbing potentials, Journal of Physics B: Atomic, Molecular and Optical Physics **31**(4), 645 (1998).

[97] M. Henseler, T. Dittrich, and K. Richter, Classical and quantum periodically driven scattering in one dimension, Physical Review E **64**, 046218 (2001).

[98] K. Husimi, Some Formal Properties of the Density Matrix, Proceedings of the Physico-Mathematical Society of Japan **22**, 264 (1940).

[99] K. Takahashi, Distribution Functions in Classical and Quantum Mechanics, Progress of Theoretical Physics Supplement **98**, 109 (1989).

[100] C. Petri, F. Lenz, F. K. Diakonos, and P. Schmelcher, Directed transport and localization in phase-modulated driven lattices, Physical Review E **81**, 046219 (2010).

[101] C. Petri, F. Lenz, B. Liebchen, F. Diakonos, and P. Schmelcher, Formation of density waves via interface conversion of ballistic and diffusive motion, Europhysics Letters **95**, 30005 (2011).

[102] S. R. Hudson, Calculation of cantori for Hamiltonian flows, Physical Review E **74**, 056203 (2006).

[103] P. Schmelcher and F. K. Diakonos, Detecting Unstable Periodic Orbits of Chaotic Dynamical Systems, Physical Review Letters **78**, 4733 (1997).

[104] P. Schmelcher and F. K. Diakonos, General approach to the localization of unstable periodic orbits in chaotic dynamical systems, Physical Review E **57**, 2739 (1998).

[105] J. Mather, A criterion for the non-existence of invariant circles, Publications Mathématiques de L'IHÉS **63**, 153 (1986).

[106] R. Mackay, J. Meiss, and I. Percival, Transport in Hamiltonian systems, Physica D **13**, 55 (1984).

Danksagung

Ich möchte mich zuerst bei Prof. Peter Schmelcher für die Betreuung der Doktorarbeit und die Unterstützung während meiner Promotion bedanken.

Großer Dank gebührt Prof. Fotis Diakonos, der mit einigen Ideen und Hilfestellungen zu dieser Arbeit beigetragen hat. Die Aufenthalte in Griechenland haben mir immer sehr viel Freude bereitet.

Bei meinem Bürokollegen Benno Liebchen möchte ich mich für die vielen guten Anregungen und das Korrekturlesen der Dissertation bedanken.

Ein Dank geht auch an Christian Morfonis, Ioannis Brouzos, Thomas Wulf und Panagiotis Giannakeas, die ebenfalls dabei geholfen letzte Verbesserungen vorzunehmen.

Besonders bedanken möchte ich mich bei meiner Familie und meinen Freunden. Ohne ihre Unterstützung wäre diese Dissertation nicht möglich gewesen.